Stony Brook University

Engineering Enhanced Piezoelectric Response in Ferroelectric Superlattices

A Dissertation Presented

by

John Sinsheimer

to

The Graduate School

in Partial Fulfillment of the Requirements

for the Degree of

Doctor of Philosophy

in

Physics

Stony Brook University

December 2012

Stony Brook University

The Graduate School

John Sinsheimer

We, the dissertation committee for the above candidate for the Doctor of Philosophy degree, hereby recommend acceptance of this dissertation.

Matthew Dawber – Dissertation Advisor
Assistant Professor, Department of Physics and Astronomy

Thomas Weinacht – Chairperson of Defense
Professor, Department of Physics and Astronomy

Maria Victoria Fernandez-Serra
Assistant Professor, Department of Physics and Astronomy

Premala Chandra
Professor, Department of Physics and Astronomy
Rutgers University

Myung-Geun Han
Assistant Physicist, Condensed Matter Physics and Materials Science
Brookhaven National Laboratory

This dissertation is accepted by the Graduate School.

Charles Taber
Interim Dean of the Graduate School

Abstract of the Dissertation

Engineering Enhanced Piezoelectric Response in Ferroelectric Superlattices

by

John Sinsheimer

Doctor of Philosophy

in

Physics

Stony Brook University

2012

The piezoelectric effect is a useful property of certain crystals where the application of pressure on a crystal produces a voltage, and conversely in the inverse piezoelectric effect, the size of the crystal changes with the application of voltage. Piezoelectricity is widely used in devices such as ultrasound machines and various sensors and actuators. This thesis presents the development of two artificially layered material systems with enhanced piezoresponse and techniques developed to accurately characterize functional properties.

Large piezoelectric responses, such as those seen in $PbZr_xTi_{1-x}O_3$ in the vicinity of the compositional morphotropic phase boundary, can occur when the direction of the polarization in a ferroelectric material can rotate. Here we combine $PbTiO_3$, a ferroelectric with out-of-plane polarization when grown on $SrTiO_3$, and $CaTiO_3$, a ferroelectric with in-plane polarization when grown on $SrTiO_3$, into high quality superlattices in various material ratios to attempt to engineer polarization rotation and enhanced piezoelectric response.

X-ray diffraction performed using a lab diffractometer and using NSLS X21 and X22C beamlines was used to measure the structure of superlattices, confirming compositional phase changes with rotations of polarization directions. Electrical measurements showed an enhancement of the dielectric constant and piezoforce microscopy showed a twofold enhancement of the piezoresponse of $PbTiO_3$ at a particular material ratio in the superlattice.

In contrast to the polarization rotation driven behavior seen in $PbTiO_3/CaTiO_3$, when $PbTiO_3$ and $BaTiO_3$, a ferroelectric also with out-of-plane polarization, are combined in a superlattice, enhanced piezoelectric response is driven by other, interfacial, effects. To realize this system, the challenging growth of strained $BaTiO_3$ on $SrTiO_3$ is required. It was found that successful growth was highly dependent on electrical boundary conditions, an effect we have studied by the use of in situ synchrotron x-ray diffraction during growth at X21.

Contents

List of Figures

List of Tables

Acknowledgements

I would like to thank my adviser, Matthew Dawber, for providing the opportunity to carry out this research, and for his excellent guidance and suggestions on all the various projects. I would like to acknowledge all my current and former group members who helped make this work possible, including Sara Callori, Benedikt Ziegler, Ben Bein, Lukas Kürten, Yucef Benkara, Juliana Coraor, Jon Daley, Humed Yusuf, Kevin Chen, and Grace Pan.

Thanks to Sara and Matt for helping to put the lab together and making everything actually work. Thanks to Benedikt for growing our first films and superlattices. I'd also like to acknowledge Randy Headrick and Priya Chinta and other group members from UVM who helped make our NSLS X21 beamline experiments successful, and thank you to Peter Stephens for helping us use and learn the X22C beamline. Thanks to Bent Nielsen and Xu Du and his group for their work and equipment that makes our electrical measurements possible. Thank you to Dong Su for HR-STEM measurements on our samples, to MG Han for teaching me about TEM sample preparation and measurements, and thank you to all of our other collaborators.

Thank you to my thesis committee for their comments and suggestions that improved the quality of this thesis. Thank you again to Sara, Ben, and Matt for your suggestions and comments that improved this thesis. I would like to thank Nicolas Stucki for the use of his sputtering figure and for his thesis, which provided an excellent resource about ferroelectrics and characterization techniques.

I would like to give additional thanks to my friends Chris, Kunal, Burton, Andrew, and others and thank you to Tracie, Ben, Amy, Mom, and Dad, and all other family members for your support. Thank you to Candace for your love and support throughout the last 3.4 years.

Chapter 1

Introduction

Ferroelectrics are insulating materials with interesting and useful functional properties that have found applications in sensors, actuators, and even computer memories. Ferroelectrics are defined as materials that have a spontaneous electric polarization that can be switched between two stable polarization states with the application of an electric field. If the electric polarization is plotted against the applied field, one obtains a hysteresis loop, a defining feature of a ferroelectric, with an example shown in Figure 1.1, Materials that are ferroelectric are also piezoelectric, meaning the strain state of the crystal is coupled to the polarization, and ferroelectrics are pyroelectric, meaning the temperature of the crystal is coupled to a spontaneous polarization. The additional requirement for a ferroelectric compared to a pyroelectric is that the spontaneous polarization must be able to be switched by an electric field. The name ferroelectric is derived from ferromagnet, which are analogous materials that can exhibit spontaneous magnetic polarization that is switchable with an applied magnetic field, with the most well known example of which is iron. Ferroelectricity was first discovered in Rochelle salt in 1921 [78], but the microscopic origins were not well understood at the time. A significant step forward in understanding was enabled by the discovery of $BaTiO_3$ in 1945 [80], which has the simpler perovskite lattice structure, and indeed, all of the materials considered in this thesis are perovskite oxides. Today, ferroelectrics are a very active field of research. A few of the most active sub-fields at present are artificially layered structures with novel properties [21, 47, 52, 70, 72], the development of materials with large piezoelectric coefficients [7, 31, 51, 57, 63], and the study of interfaces between ferroelectrics and other materials [13, 42, 87].

Ferroelectricity can arise either from asymmetric ionic displacements in the crystal structure or asymmetries in electronic charge in the unit cell, which when summed over the entire crystal, results in an electric dipole moment or electric polarization. Most ferroelectrics actually combine both of these

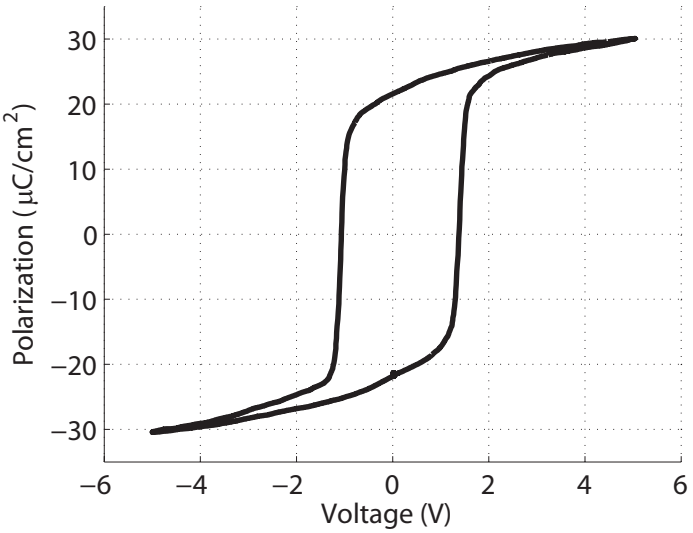

Figure 1.1: A defining feature of a ferroelectric is the electric polarization hysteresis loop, shown here for a sample of $PbTi_{1-x}Zr_xO_3$. The material has a spontaneous polarization at zero applied field, and the polarization state may be switched by applying a field in the opposite direction to the spontaneous polarization.

kinds of polarization to some extent. The polarization over the entire crystal is typically not uniform, but instead, small regions of uniform polarization form with different orientations to one another. These regions of uniform polarization are known as domains, and the boundaries between domains are known as domain walls. Different domain configurations form in response to electromechanical boundary conditions of the sample or other effects. The study of domain structure and behavior and their effect on various material properties is another active field of research [11, 50, 66, 69].

The structural and functional properties of ferroelectric materials can be tuned by an applied strain from a substrate. Additionally, modern advances in growth techniques allow for epitaxial growth of materials to a precision of single unit cell layers, enabling the creation of artificial structures of two or more materials as in superlattices. A superlattice consists of a repeated pattern of two or more layered materials of certain thicknesses, which can be as thin as single unit cell layers. Many properties of the system can be tuned by changing the relative number of unit cell layers of each material in the superlattice. The interaction between layers or interfacial effects can result in new behaviors not seen in either of the constituent materials in bulk, with a few examples being enhanced piezoresponse, enhanced dielectric constant, or

rotated polarization orientations [6, 20, 31, 54].

This thesis examines two methods of enhancing piezoresponse in ferroelectric superlattices. First, a discussion of materials used and background information is presented in Chapter 2. The process of superlattice growth in this work, through sputter deposition, is discussed in Chapter 3. Once a superlattice is grown, its structural and electrical properties are characterized using a variety of techniques as explained in Chapters 4 and 5, respectively. Using the described growth techniques, superlattices composed of $PbTiO_3$ and $CaTiO_3$ were produced and exhibit a rotation in polarization orientation from sample to sample, giving rise to an enhanced piezoresponse, as discussed in Chapter 6. Additionally, we examined superlattices composed of $PbTiO_3$ and $BaTiO_3$, which also show enhanced piezoresponse, but due to other, interfacial effects, as described in Chapter 7. The coherent growth of $PbTiO_3/BaTiO_3$ superlattices strongly depends on the highly strained $BaTiO_3$ layers. To better understand the mechanisms for coherent growth, the growth of $BaTiO_3$ was studied at the X21 beamline at the National Synchrotron Light Source, and this work is presented in Chapter 8.

Chapter 2

Background and Materials

The materials discussed in this work, are all perovskite oxides, which are a class of materials having the general chemical formula ABO_3 with pseudo-cubic structure. The unit cell of a cubic perovskite oxide is shown in Figure 2.1, having the A ions on the corners, the B ion in the center, and the oxygen ions on center of the faces. The a, b, and c lattice parameters are measures of the length, width, and height of the unit cell. Depending on the ions and temperature, the unit cell may distort in a variety of different ways, with a few examples shown in the bottom of Figure 2.1. The valence of the A cation typically ranges from +1 to +3, while the valence of the B cation typically ranges from +3 to +6. The A and B sites may have mixed ions, as in solid solutions such as $PbTi_{1-x}Zr_xO_3$, commonly referred to as PZT. Perovskites have a wide range of possible behaviors, having been shown to be ferroelectric, ferromagnetic, anti-ferroelectric, paraelectric, insulating, conducting, or even superconducting, depending on the ions in the crystal.

Perovskites that are ferroelectric generally have a high symmetry cubic phase in the $Pm\bar{3}m$ space group at high temperature and are paraelectric in this phase. As temperature is lowered from the high symmetry temperature, these ferroelectrics undergo one or more structural phase transitions leading to lower symmetries and to ferroelectricity. The relationship between physical properties of the crystal and symmetry is given by Neumann's principle [34, 55], which states that the symmetry associated with a physical property in the crystal should be higher or equal to the symmetry of the crystal point group. Of the 32 crystal point groups, 20 allow for piezoelectricity for which there is no center of symmetry. This number reduces to 10 for materials that are also pyroelectric, which requires unique polar axis, and which also allows for spontaneous polarization in the absence of an external field. Thus by symmetry arguments, ferroelectric materials are also pyroelectric and piezoelectric.

Perovskite ferroelectrics may be classified into A-type or B-type driven

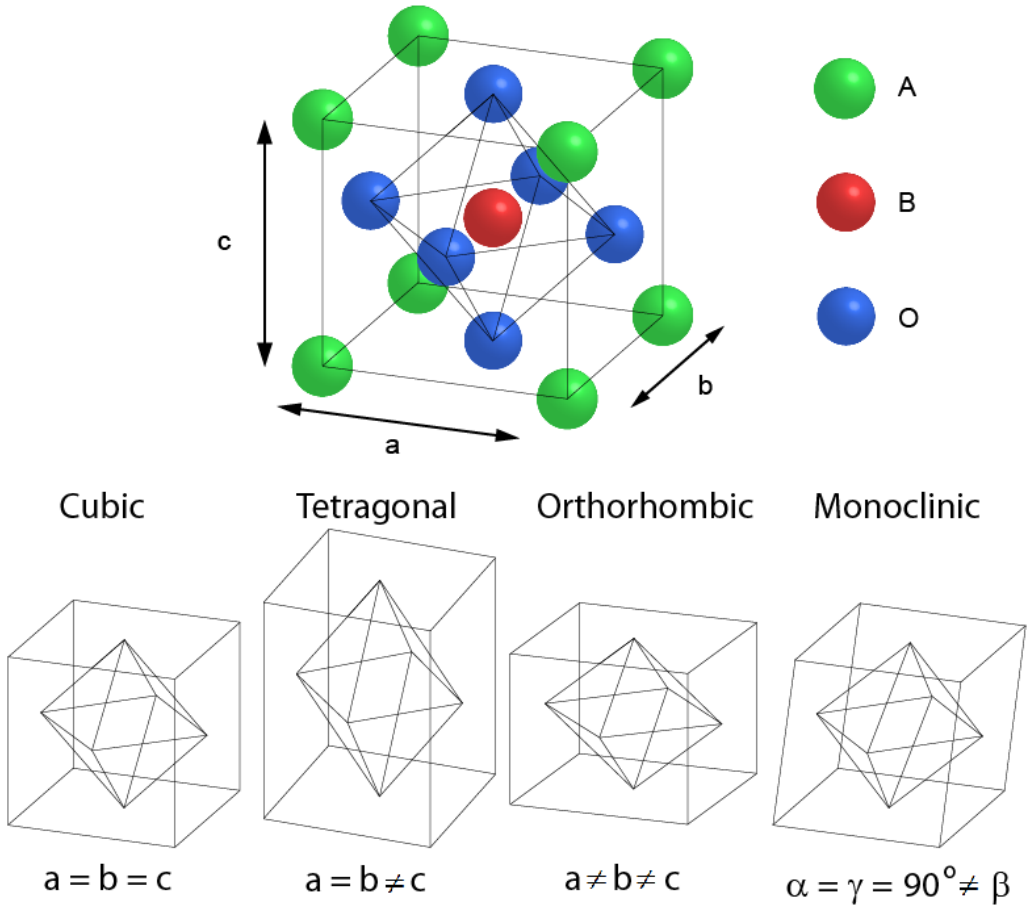

Figure 2.1: (Top) The unit cell of a cubic ABO_3 perovskite is represented with A ions on the corners, a B ion in center of the unit cell, and oxygen ions on the faces, forming an octahedron around the B ion. (Bottom) The unit cell may distort in a variety of different ways, with a few examples shown here for tetragonal, rhombohedral, and monoclinic.

ferroelectrics depending on the relative sizes of the A and B ions in the unit cell. The ferroelectrics used in this work are $PbTiO_3$, $BaTiO_3$, and $CaTiO_3$, which all have the B-site occupied by a Ti atom. The general behavior of the ions in a perovskite ferroelectric can be described by the tolerance factor, defined by $t = (R_A + R_O)/\sqrt{2}(R_B + R_O)$, where R_A, R_B, and R_O are the atomic radii of the A, B and O ions in the crystal, respectively. A tolerance factor of t≈1 corresponds to a cubic perovskite structure. For the $ATiO_3$ materials discussed in this work, the different A ionic radii compared to the Ti ionic radii will lead to either t>1 or t<1. Materials with t>1 are known as B-site driven and tend to have the Ti ion move off center, as in $BaTiO_3$ at low temperatures, which has rhombohedral structure. Materials with t<1 are known as A-site driven and tend not to be ferroelectric. Good examples are $SrTiO_3$ and $CaTiO_3$ that have values of t slightly less than one, and exhibit tilting of the oxygen octahedra [33, 60]. $PbTiO_3$ has the A sites occupied by Pb^{2+} ions that have hybridization between the Pb 6s states and O 2p states leading to a large strain, that stabilizes the tetragonal phase. This also leads to an indirect change between the hybridization of the Ti and O ions, which becomes necessary for ferroelectricity [15]. In this case, the stable positions of oxygen and titanium ions shift either up or down along the longer axis relative to the Pb ions, resulting in one of the two stable polarization states.

2.1 $SrTiO_3$

The perovskite films and superlattices in this work are all grown on substrates of $SrTiO_3$, which is a cubic perovskite at room temperature, having lattice parameters a=b=c=3.905 Å. $SrTiO_3$ is paraelectric and at room temperature is easily polarizable under an applied field, having a dielectric constant of about 300 [73]. $SrTiO_3$ is insulating, but may be made conducting by doping with niobium. Unlike some other perovskite oxides, $SrTiO_3$ does not have a structural phase transition into a ferroelectric phase as temperature is decreased. As temperature is decreased from room temperature, $SrTiO_3$ does undergo a phase transition at about 110 K to tetragonal with $I4/mcm$ space group. In this phase, the oxygen octahedrons rotate around the c axis, with antiferrodistortive ordering from one unit cell to the next [29]. It is likely that $SrTiO_3$ has no phase transition to ferroelectricity due to quantum fluctuations [9].

2.2 $SrRuO_3$

$SrRuO_3$ is a metallic perovskite having a resistivity of about 140 $\mu\Omega$·cm at room temperature [3] and is used as a bottom electrode, being grown on top of the $SrTiO_3$ substrate before a film or superlattice is grown. The resistivity of $SrRuO_3$ is about 10 times lower resistivity than that of Nb-doped $SrTiO_3$ and it can be grown with a very smooth, atomically flat surface. Additionally, growth of $SrRuO_3$ in this work is done here in-situ, immediately prior to the deposition of other materials, preventing possible surface contaminants that could attract to the metal. Bulk $SrRuO_3$ has an orthorhombic crystal structure at room temperature with lattice parameters a=5.53 Å, b=5.57 Å, and c=7.85 Å, with a lattice distortion of 89.6° [41]. The pseudocubic lattice parameter is a_{pc}=3.93 Å, which has an in-plane lattice mismatch with $SrTiO_3$ of 0.6%. When grown on $SrTiO_3$, $SrRuO_3$ still exhibits an orthorhombic structure at room temperature, but the phase transition from tetragonal to orthorhombic is lower, than compared to bulk, occurring at about 350 °C. [49]. At higher temperatures of about 600-700 °C, $SrRuO_3$ has a cubic to tetragonal phase transition when grown on $SrTiO_3$. At lower temperatures, below 155 K, $SrRuO_3$ is ferromagnetic [19].

2.3 $PbTiO_3$

Both superlattices discussed in this work contain $PbTiO_3$, which is tetragonal and ferroelectric in bulk at room temperature, having lattice parameters of a=b=3.904 Å and c=4.152 Å. The ferroelectric distortion results in a shift of the oxygen and titanium ions in the same direction along the c axis, with a larger magnitude of displacement of the oxygen ions, with respect to the lead ions. The crystal symmetry transitions from a paraelectric cubic $Pm\bar{3}m$ phase with lattice parameters a=b=c=3.969 Å to tetragonal and ferroelectric $P4mm$ phase at about 490 °C. $PbTiO_3$ has a large ferroelectric polarization, as high as 75 $\mu C/cm^2$ [10]. $PbTiO_3$ can be grown on $SrTiO_3$ under compressive strain of -1.64%. When $PbTiO_3$ is epitaxially constrained in-plane to the lattice parameter of a $SrTiO_3$ substrate, the crystal is tetragonal and has polarization directed along the [001] direction.

2.4 $BaTiO_3$

$BaTiO_3$ is a ferroelectric perovskite at room temperature having tetragonal structure with lattice parameters of a=b=3.99 Å and c=4.04 Å. $BaTiO_3$

undergoes several structural phase transitions from cubic, $m3m$, at high temperature to lower temperatures. The cubic high temperature phase has lattice parameters of a=b=c=4.01 Å and the tetragonal phase transition occurs around 120 °C. At lower temperatures around -3 °C, the structure transitions to orthorhombic, mm space group, and then to trigonal at -93 °C with $3m$ space group, which are also ferroelectric phases. During these phase transitions, the polar axis of the ferroelectric phases changes from [001], to [011], to [111], respectively [43]. The structural phase transition temperatures of these multiple phases are strongly dependent on the strain [15]. The spontaneous polarization of single crystal $BaTiO_3$ has been measured to be 26 $\mu C/cm^2$ [38], which is significantly less than $PbTiO_3$. When grown on $SrTiO_3$, $BaTiO_3$ is under a large compressive strain and tends to undergo relaxation processes, forming defects instead of remaining coherent with the in-plane lattice parameters of the substrate.

2.5 $CaTiO_3$

$CaTiO_3$, like $SrTiO_3$, is an A-site driven perovskite and is not ferroelectric at room temperature in bulk [18]. Single crystal $CaTiO_3$ at room temperature has orthorhombic structure with lattice parameters of a=5.442 Å, b=5.380 Å, and c=7.640 Å, and having a pseudocubic parameter of a_{pc}=3.826 Å [64]. Interestingly, $CaTiO_3$ does not exhibit a structural phase transition over a large temperature range, staying orthorhombic up to temperatures of 1100 °C [14, 45]. When grown on $SrTiO_3$, $CaTiO_3$ is under a fairly large tensile strain of 2%. Thin films of $CaTiO_3$ grown on $SrTiO_3$ have shown only paraelectric behavior in the out-of-plane direction [68]. However, first principles calculations suggest that the ground state of $CaTiO_3$ under sufficient tensile strain ($> 1.5\%$) is orthorhombic with space group O and with ferroelectric polarization directed along [110] directions with respect to $SrTiO_3$ substrate [18].

2.6 Piezoelectricity

Due to crystal symmetries, ferroelectrics are also piezoelectric, and ferroelectrics tend to have desirable piezoelectric properties since polarization is coupled to the strain in polarizable materials. Piezoelectricity is defined in terms of the direct piezoelectric effect, where an applied stress leads to charges on the surface, equivalently in the converse piezoelectric effect, an applied electric field leads to a strain of the crystal. In this thesis, measurements are performed by the application of an electric field, so we will specifically

focus on the converse piezoelectric effect and measuring strain.

The strain of a material is defined as relative size distortion in response to an external effect. As a simple example, if a one dimensional object of length l changes in length by x due to some external effect, the strain is calculated as $S = x/l$ and is unitless. If the strain is induced by an electric field E, then the piezoelectric coefficient d, is defined by $d = S/E$, with units of m/V. In real, three-dimensional materials, a distortion of a crystal in one direction can result in distortions in other directions, so strain is given by a rank 2 tensor, or a 3x3 matrix of strain coefficients, S_{ij}, where i,j=x, y, or z. However, it can be shown that the strain tensor is symmetric, so the number of unique components in this matrix is only 6 instead of 9 [48], with components S_{xx}, S_{yy}, S_{zz}, S_{yz}, S_{zx}, S_{xy}. The strain tensor is typically written in terms of Voigt notation, where the subscript ij is replaced by a single letter such as m, with values ranging from m=1-6. The numbers m=1-6 this case correspond to m=1=xx, m=2=yy, m=3=zz etc. in the same order presented above for the strain coefficients [44].

Since the electric field can also be applied in three dimensions, the piezoelectric coefficient, d_{kij}, is expressed as a rank 3 tensor and defined from the equation [62]

$$S_{ij} = d_{kij} E_k \tag{2.1}$$

The piezoelectric coefficient tensor d_{ijk} contains 3^3=27 components, but due to symmetries of the stress and strain tensor, the number of unique components is only at most 18 for the case of triclinic crystal structure, and the unique number of components is further reduced for higher crystal symmetries. For tetragonal crystals of $4mm$ symmetry, the piezoelectric coefficient only has 3 unique components [62]. Using Voigt notation, the d_{ijk} tensor can be expressed as d_{km}, where m ranges from 1-6 as explained before for the stress tensor, thus the piezoelectric coefficient d_{km} can be written as a 3x6 matrix of components.

In this work, we measure an effective piezoelectric coefficient d^*_{33} in Voigt notation, or d^*_{333} in tensor notation. A field is applied in the out-of-plane direction, or nearly out-of-plane direction, and the measured strain response is measured along the out-of-plane direction. Equation 2.1 is applicable only along the polar axis of the crystal. If the applied field is not perfectly in the out of plane direction, as in the case when measuring with a conductive AFM tip (see Chapter 5), or when the polarization direction is not purely in the out-of-plane direction, then the measured piezoresponse is typically determined by multiple components of the piezoelectric coefficient tensor. The effective piezoelectric tensor in this case must be considered as a coordinate transformation from the real piezoelectric tensor defined by the polar axis in

the crystal [62]

$$d^*_{ijk} = A_{il}A_{jm}A_{kn}d_{lmn} \tag{2.2}$$

where each A is a part of a coordinate transformation matrix, relating the two coordinate systems, resulting in typically complicated expressions. For example, in the case of a tetragonal crystal with space group $4mm$, if a field is applied at an angle θ off of the polar axis of the crystal, the effective piezoelectric coefficient d^*_{33} is given by [55]

$$d^*_{33} = \cos\theta[\sin^2\theta(d_{15} + d_{31}) + \cos^2\theta d_{33}]$$

Depending on the angle θ and the relative magnitudes of the different piezoelectric tensor components, $(d_{15} + d_{31})$ compared to d_{33}, it will not be clear whether a measured piezoresponse is mostly due to large values of $(d_{15} + d_{31})$ or large values of d_{33}. With this in mind, measurements of the piezoresponse in this thesis that are referred to as the d_{33} are really measurements of an effective d^*_{33}. However, it is still very useful to compare measured effective d^*_{33} values from sample to sample in order to better understand the underlying properties that give rise to different piezoelectric responses.

Chapter 3

Thin Film Growth

The perovskite oxides discussed in this work are all grown using a technique known as off-axis RF magnetron sputtering. Sputtering is a form of physical vapor deposition in which a target material is vaporized and then deposited onto a substrate. Sputter deposition has the advantage of lower costs and ease of use compared with other physical vapor deposition techniques such as pulsed laser deposition (PLD), or molecular beam epitaxy (MBE), and off-axis sputtering is able to provide growth precision of single unit cell layers [60]. In our deposition system, the material to be grown begins as a 1.3" compressed ceramic disk, called the target, containing a compressed powder of the material in the correct stoichiometric ratios. In this work, targets were purchased initially from Praxair, and later Kurt J. Lesker. The target is placed on the end of the sputter gun with some thermal paste to ensure thermal conductivity and held in place with a magnetic backing. The end of the sputter gun sits in a vacuum chamber near the heated substrate. To initiate sputtering, an RF field with a frequency of 13.56 MHz is produced by the sputter gun, stripping away electrons from the argon gas. The argon ions are mostly unaffected by the RF field, due to a combination of the high frequency of the field and large mass of the ion. The sputter gun acts as the cathode while the rest of the chamber, which is grounded, acts as the anode. The shape of the RF field then causes an asymmetry in the concentration of electrons, with more electrons concentrated near the cathode and less concentration around the anode. This induces a self-bias, giving rise to a DC field seen by the argon ions, causing the argon ions to accelerate towards the target. Additionally, the permanent magnets on the sputter gun constrain the shape of the plasma. The accelerated ions collide with the target material with enough energy that material is ejected from the surface into a vapor. Some of the vapor reaches the heated substrate, combining with oxygen gas present to grow the perovskite oxide. This process is illustrated in Figure 3.1. The off-axis geometry, where

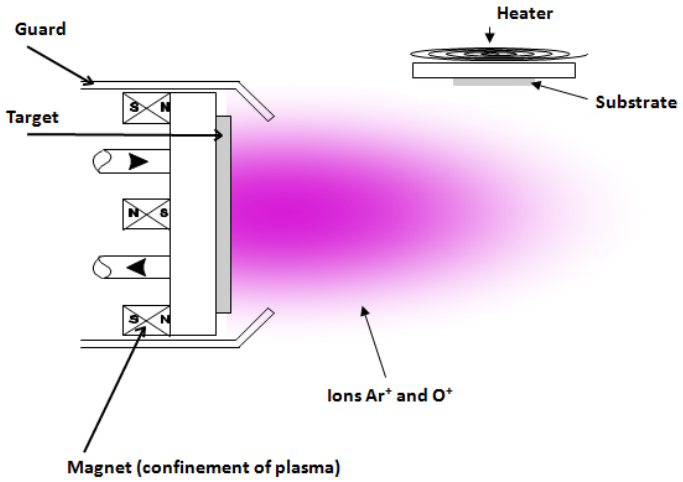

Figure 3.1: An illustration of the off-axis RF magnetron sputter deposition process. Used with permission from Nicolas Stucki.

the substrate is positioned 90 degrees off of the sputter gun axis, results in slower growth, but better surface quality. In the on-axis geometry, highly energetic ions from the target can cause sputtering at the substrate surface, resulting in poor growth.

Prior to a deposition, a substrate is first cleaned, then pasted onto a heater, and finally placed into the deposition chamber. Substrates are cleaned by placing them into a beaker of acetone, which is placed into an ultrasonic cleaner for 5 minutes. This process is repeated with a beaker of ethanol, and then the substrate is dried with nitrogen gas. The substrate is then pasted with silver paste onto the center of a resistive heater and baked in an oven at 200 °C for one hour to expedite drying of the silver paste. The silver paste will ensure good thermal conductivity between the heater and substrate during growth. After the heater cools from the oven, it is placed inside the deposition chamber, which is then pumped down until the vacuum pressure is less than 6E-7 Torr (8E-7 mbar). Pumping the chamber down to low vacuum pressure removes contaminants such as water and nitrogen.

The deposition chamber is a custom design allowing for six sputter guns and is shown in Figure 3.2 and having other parts required to perform sputter deposition. Growth is performed at low pressures, typically around 0.18 Torr, by flowing in oxygen and argon gas into the chamber in a specific ratio. The chamber pressure is measured with an MKS Baratron type 627B absolute pressure transducer. This pressure gauge has a number of features to ensure consistent pressure readings. For example, the gauge is heated internally to 45

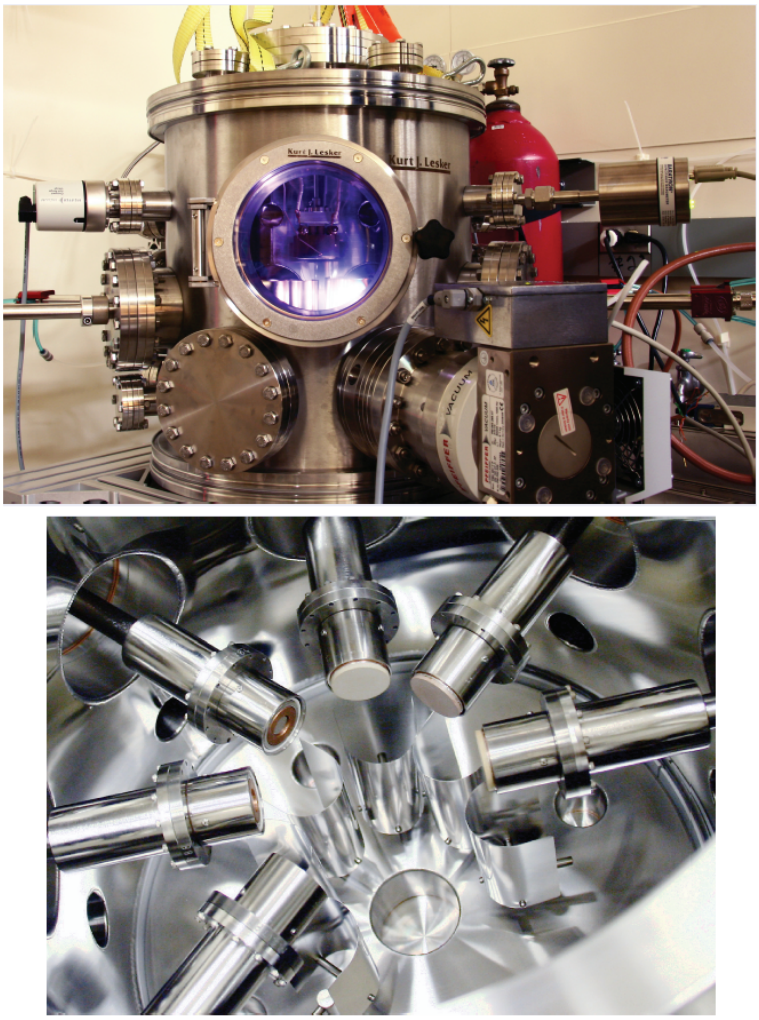

Figure 3.2: (Top) A side view of our vacuum chamber showing a purple plasma inside. (Bottom) An overhead view inside of our vacuum chamber with six sputter guns and shutters spaced around the center of the chamber.

°C, so measurements are not affected by changes in environmental temperatures as other gauges typically are. The overall chamber pressure is regulated by a butterfly valve and the pressure sensor in conjunction with a turbomolecular pump and roughing pump behind the butterfly valve. The butterfly valve changes the size of the opening that the pumps act upon while monitoring the chamber pressure, providing accurate control of the overall chamber pressure. Gas flow is regulated by mass flow controllers, which accurately control gas flow rates in units of standard cubic centimeters per minute (SCCM). The resistive heater on which the substrate is pasted fits into a mount in the off-axis geometry when the chamber is at atmospheric pressure. A thermocouple made of Alumel and Chromel is inserted into a hole in the base of the heater in order to determine the temperature of the heater. Insulated copper wires connect to the electrodes on the heater to provide the DC power that heats the heater. The sputter guns are powered by a combination of several devices that provide the RF power, selects a sputter gun, and matches the impedance of the sputter gun. Sputter guns and targets are shielded from one another by movable shutters, which are controlled by compressed air valves and computer controlled electronics.

The deposition process is performed by a Labview program that controls and monitors all the previously described devices. The program first sets the flow rates of oxygen and argon and sets the chamber pressure through the butterfly valve, according to the specified growth conditions for a given material as shown in Table 3.1. A PID controller controls a DC power supply voltage to the heater while monitoring the thermocouple, causing the heater to ramp up to the growth temperature and stabilize. After 5 minutes of stable oxygen flow, argon flow, temperature, and pressure values, the shutter for the specific sputter gun is opened and the gun is powered on for a user specified amount of time. Figure 3.3 shows the heater inside the chamber just before and after the sputter gun is turned on. In the program interface, the user selects the desired number of unit cells to grow, and the program calculates the deposition time based on the user defined growth rate, which is previously determined and monitored by other growth measurements. For superlattices that alternate material growth, the sputter gun is turned off and shutter is closed for 2 minutes before the next sputter gun and shutter is activated. After all the material layers have been grown, the heater is cooled under the same pressure and flow conditions until the temperature is less than 80 °C, since perovskite oxides tend to form oxygen vacancies or other undesirable features at high temperatures and low oxygen partial pressures. The growth parameters for materials in a superlattice are typically not the best growth parameters for a thin film of a single material. In particular, $BaTiO_3$ is grown

	$SrRuO_3$	$PbTiO_3$	$CaTiO_3$	$BaTiO_3$
Temperature (°C)	620	550	550	550
Pressure (Torr)	0.1	0.18	0.18	0.18
Flow O_2 (SCCM)	6	7	7	7
Flow Ar (SCCM)	32	16	16	16
Gun Power (W)	30	35	45	30
Approx. Growth Rate (mins/unit cell)	1.5	2.6	6.3	1.5

Table 3.1: A table of growth conditions for materials in superlattices in our home chamber. Note that thin films of each of these materials may have different ideal growth temperatures than is used in superlattice.

at a lower temperature in a superlattice with $PbTiO_3$ compared to a thin film of pure $BaTiO_3$, since Pb is very volatile and hence grows very poorly at higher temperatures. It is generally observed that keeping the sample at the same temperature throughout the growth process results in higher quality superlattices.

3.1 Substrates

The thin films and superlattices in this work are all grown on substrates of (001) oriented $SrTiO_3$ or Nb-doped $SrTiO_3$, purchased from CrysTec. $SrTiO_3$ is grown as a large, cylindrically shaped single crystal and then cut into smaller 5x5 mm square substrates with thickness of about 1 mm. These cuts are typically not at 0 degrees with respect to the unit cells in the crystal, but off by a small angle, known as the miscut angle, resulting in a step and terrace structure of the surface, with steps being the height of one unit cell. Substrates are then treated with buffered HF and annealed to ensure TiO_2 termination on one surface, while the other side is unpolished. The crystallinity and surface quality of the purchased substrates is then measured in our lab by performing x-ray diffraction and atomic force microscopy (AFM) (See Chapter 4). Very good quality substrates will show a rocking curve with single narrow full width at half maximum (FWHM) of 0.02° or less, and no diffraction peaks outside of the main diffraction peaks. Extra peaks measured in the rocking curve signify crystal at a different lattice parameter, twinning, or other structural defects. Substrates with lower quality are used for growth calibration while higher quality substrates are used for samples that will be most thoroughly characterized. The surface topography from AFM measurements should show single unit cell layer step and terrace structure with well defined step edges. This

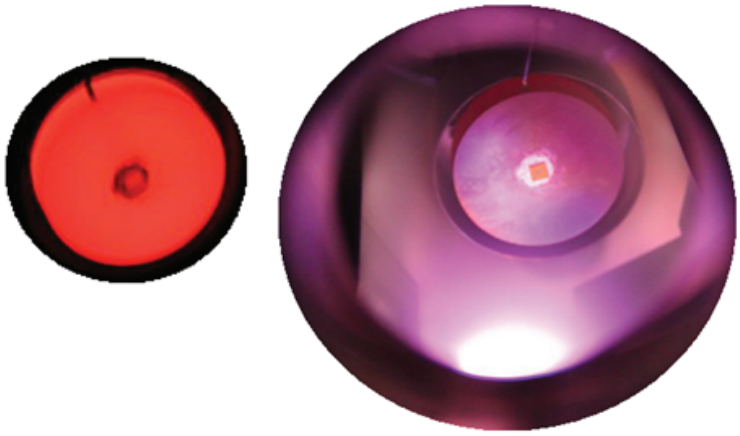

Figure 3.3: (Left) A heater at a temperature of 600 °C with pasted substrate in center, inside of the chamber. (Right) The sputter gun is now turned on, creating a purple light from the Ar ions.

step and terrace structure results from the cutting process of the substrates not exactly along a crystal plane, defining a miscut angle. The purchased substrates sometimes show over-etching, leading to pits in the surface, so it is important to verify the absence of these features for quality crystal growth. $SrTiO_3$ substrates may be doped with niobium through ion implantation, resulting in a conducting substrate which may be used as a bottom electrode for electrical measurements. However, the doping process degrades the crystal quality, which then affects the quality of grown films and superlattices.

3.2 Growth Calibration

To achieve control over single unit cell layer growth, the rate of growth, or 1/rate in terms of minutes per unit cell layer, must be accurately known. A new target placed onto the end of a sputter gun is first presputtered for typically 24 hours or longer. This helps to clean the target and establishes equilibrium conditions in which a material is sputtered at a slow, constant rate, with 1/rate values typically between 1.5 and 6.5 minutes per unit cell layer, depending mainly on the type of material and sputter gun power. To determine the growth rate of a new target that has been presputtered, a substrate is prepared and placed into the chamber and growth is then performed for a set amount of time, such as 100 minutes. Then the total number of unit cells grown is measured with x-ray diffraction and reflectivity, allowing for a calculation of minutes per unit cell layer. As targets are sputtered over time,

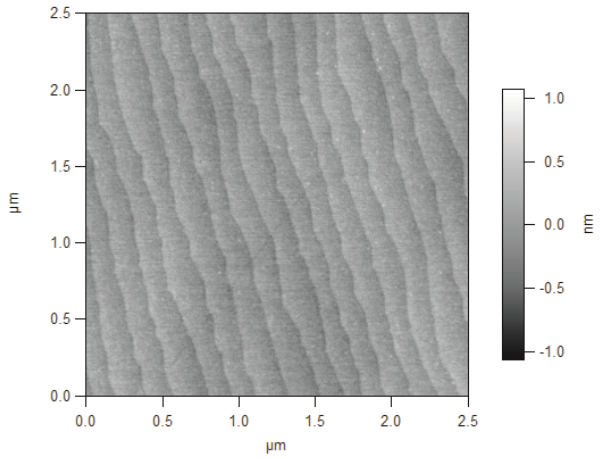

Figure 3.4: Atomic force microscopy surface topography of a $SrTiO_3$ showing unit cell height steps.

the growth rate tends to slow slightly, resulting in longer times required to deposit a unit cell layer, so it is important to continually measure the growth of each sample grown and consider adjustments to the growth rates as needed. For consecutive samples grown in our lab, the growth rate changes only for older targets, and in this case, changes less than 0.5 % from sample to sample.

In the case of superlattices, it is generally not possible to measure the thickness of each material layer, but only a superlattice wavelength, the thickness of the repeated structure. Therefore, before any superlattices are grown, the growth rate of each material in the superlattice must be known accurately. The volume fraction of one material in a given superlattice will typically not exactly match the nominal growth, having a slight shortage or excess of one or both materials. To determine the volume fraction of each material in a superlattice, it is necessary to consider the growth of several different superlattices grown consecutively and compare the measured actual bilayer thickness, in terms of unit cell layers, with either the growth time of one material or with the expected number of unit cell layers based on both growth times used. X-ray diffraction can be used to calculate the average number of unit cells in a superlattice bilayer even as the average c lattice parameter of the superlattice is changing from sample to sample. Equation 4.4 is used to calculate the thickness of the bilayer in a superlattice, and if it is divided by Equation 4.7, used to calculate the average c lattice parameter of the unit cells in the superlattice, then one obtains the measured number of unit cell layers in the bilayer of the superlattice.

One method used to adjust growth rates of superlattices is to use least

squares linear regression on the relationship between the expected number of unit cell layers grown and the growth time of one of the materials. As an example, consider a series of grown PTO/CTO superlattices consisting of a 3/3, a 9/3 and a 5/3. This particular growth rate determination method is applicable when one of the materials growth time is held at a fixed length of time per bilayer, as in the $CaTiO_3$ in this example, which is grown at 7.2 minutes per unit cell layer, implying a growth time of (7.2×3) minutes per bilayer. The $PbTiO_3$ growth time per bilayer varies significantly between superlattices in this example, and all samples are grown using 2.72 minutes per unit cell layer. So the growth times per bilayer are (2.72×3), (2.72×9), and (2.72×5), for the 3/3, 9/3, and 5/3, respectively. Assuming that growth is linear, the number of unit cell layers of $PbTiO_3$ will be related to the growth time in a linear fashion. This can be illustrated by plotting the bilayer thickness, in terms of the number of unit cell layers, against the time spent growing $PbTiO_3$ in each respective bilayer, in minutes. The result is shown in Figure 3.5 and fitted with linear regression, obtaining the equation shown on the chart. The slope of the line corresponds to the growth rate in terms of unit cell layers per minute, so the reciprocal yields 2.78 minutes per unit cell layer as the measured reciprocal growth rate of $PbTiO_3$. The y-intercept implies that the $CaTiO_3$ layers account for 3.071 unit cell layers, so the measured reciprocal growth rate for $CaTiO_3$ is $(7.2 \times 3)/3.071 = 7.03$ minutes per unit cell layer for $CaTiO_3$. With these growth rates, it becomes possible to calculate a volume fraction of each material in the superlattice that may be more accurate than the nominal growth. For example, the measured number of unit cell layers in the bilayer of the 3/3 superlattice was 6.06, from the average of the measurements of the (001) and (002) diffraction scans. Therefore the volume fraction of $CaTiO_3$ in the superlattice is calculated as $3.071/6.06 = 0.507$, which differs from the nominal volume fraction of 0.5 by a small amount.

Since the previous method relies on one material being sputtered for a fixed amount of time in the superlattice, another method of least squares may be used when consecutive superlattices are grown with either different material growth rates or if the superlattices in series have different layer thicknesses of both materials. This is accomplished by comparing the measured number of unit cell layers grown in a bilayer with the expected number of unit cells grown in a bilayer, with the latter based on the growth rates. As an example with a PTO/CTO superlattice, suppose the actual sputtering time used to grow a bilayer in a PTO/CTO superlattice is given by t_{PTO} and t_{CTO} with units of minutes, and the reciprocal growth rates to be determined are given by R_{PTO} and R_{CTO} with units of minutes per unit cell layer. Then the expected number

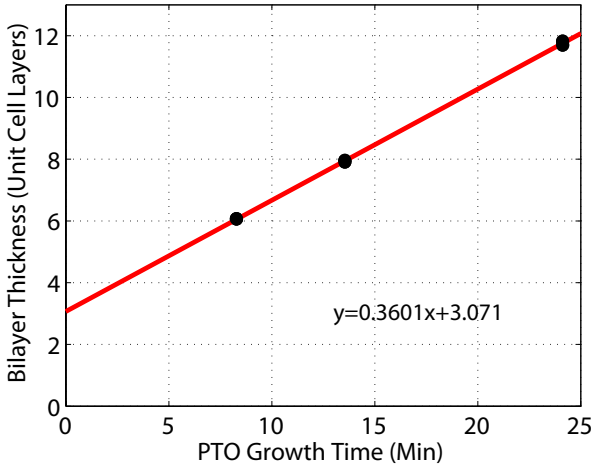

Figure 3.5: A plot used to calculate growth rates and volume fractions of each material in a set of three PTO/CTO superlattices. The error bars are about the size of the marker in this graph.

of unit cell layers in a bilayer is given by

$$n_{bilayer,expected} = \frac{t_{PTO}}{R_{PTO}} + \frac{t_{CTO}}{R_{CTO}} \tag{3.1}$$

The measured number of unit cell layers in the superlattice is determined by

$$n_{bilayer,measured} = \Lambda/\overline{c} \tag{3.2}$$

where Λ is the measured superlattice wavelength, and $\overline{c}$ is the average c lattice parameter of the unit cell layers in the superlattice. These are given by Equations 4.4 and 4.7, using a=3.905 Å for coherent growth on $SrTiO_3$ substrates. Then using methods similar to those in [8], we can define χ^2 as

$$\chi^2 = \sum \left(\frac{n_{bilayer,measured} - n_{bilayer,expected}}{\sigma} \right)^2 \tag{3.3}$$

where the sum is taken over several consecutively grown superlattices, and where σ corresponds to the uncertainties in the measured values of each n. The value of σ will depend almost entirely on the measurement uncertainty in the diffraction angles, since the sputtering time is very accurately controlled by the computer clock. So σ can be calculated directly from the error propagation equation by using the equations for $\Lambda/\overline{c}$ expanded in terms of the θ

angles, and using careful estimations of the measurement uncertainty in each measured angle in this equation. As a simplification, σ may be estimated as a fixed percentage error of $n_{bilayer,measured}$. This approximation would weigh all residuals equally in terms of the percentage error instead of the absolute differences, which would be larger for thicker bilayers and smaller for thinner bilayers. However this approximation would have to be used more carefully, or less weight would still have to be added manually for some superlattices, as sometimes superlattice diffraction peaks are not very well defined because of convolution effects. In either case, regression is performed using a computer to minimize χ^2 using the rates R_{PTO} and R_{CTO} as adjustable parameters, determining best fit growth rate values for a set of superlattices.

Both of these methods for determining growth rates over time have to be used carefully. If the consecutive superlattices grown do not vary significantly from one another or the measurement error is not properly weighted, then the regression may result in unrealistic values for growth rates. In general, if a set of values have error bars of similar size to the difference between the values, the regression will not obtain reliable results. Thus, it is very important to know the growth rates of each material accurately before superlattices are grown since, it is more difficult to establish growth rates in a series of superlattices. Although new ceramic targets used for sputtering will not immediately begin showing changes in growth rates, the growth rate will eventually begin to increase, and so it is important to track the growth and make adjustments carefully. Using these techniques, the growth of superlattices in this work generally varies from the expected growth by less than 1.5%.

3.3 $SrRuO_3$ Growth

Before growing the majority of PTO/CTO samples in this work, a short study was undertaken to improve the electrical properties and surface quality of $SrRuO_3$ by adjusting the growth temperature, and comparing growth on Nb-doped $SrTiO_3$ substrates to growth on $SrTiO_3$ substrates. Nb-doped $SrTiO_3$ has frequently been used as a bottom electrode in other works, since the niobium doping greatly increases the conductivity of $SrTiO_3$, which is normally an insulator. However, the doping process is known to reduce the surface quality of the substrates, which can in turn cause poor film growth. In this short study, samples were grown on Nb-doped $SrTiO_3$ and $SrTiO_3$ to a thickness of 100 unit cell layers, or about 40 nm, at temperatures of 600 °C, 620 °C, and 640 °C. Previously, bottom $SrRuO_3$ electrodes had been grown to 50 unit cell layers thickness, so another comparison is made by doubling the thickness to 100 unit cell layers. Surface topography was measured using an atomic force

Sample	Growth Temp (^{o}C)	Thickness (nm)	Resistance (Ω)	RMS Roughness (pm)
J0125101	600	20	100 ±5	200 ±30
J0804101*	600	40	78 ±3	330 ±30
J0810101	600	40	50 ±3	315 ±30
J0811101*	620	40	47 ±3	315 ±30
J0813101*	640	40	55 ±4	250 ±30
*Growth on Nb-$SrTiO_3$ substrate				

Table 3.2: Measured resistances between silver top electrodes for a series of $SrRuO_3$ films grown on $SrTiO_3$ and Nb-$SrTiO_3$ substrates.

microscope, and the approximate RMS surface roughness was calculated. In addition, the electrical properties were measured by first depositing 125 μm diameter silver electrodes on top of the films, then measuring the resistance between adjacent electrodes. These films and their measured properties are summarized in the Table 3.2 and some surface topography images are shown in Figure 3.6. The step and terrace structure of the film follows the step and terrace structure of the substrate.

The different samples show a number of changes in film properties depending on the growth temperature, type of substrate, and film thickness. AFM topography shows films of 100 unit cell layer thickness all have double unit cell layer steps of about 8 Å, known as step bunching, instead of the single unit cell layer steps of the substrate. This is not ideal for film growth, as it may affect the properties of films grown on top of $SrRuO_3$. This step bunching growth depends on the overall film thickness, rather than the growth temperature, based on the results shown in the table. Comparing the resistances of the films, we see decreased resistance when the thickness is doubled to 100 unit cell layers, and counterintuitively, the resistance is less for a film grown on $SrTiO_3$ as compared to Nb-doped $SrTiO_3$. This is likely the result of better film quality due to the better surface quality of the $SrTiO_3$ substrates compared to the Nb-$SrTiO_3$ substrate. The growth on Nb-$SrTiO_3$ at different temperatures shows a drop in resistance at 620 °C, but little or no change at 640 °C.

Finally the surface roughness was compared both qualitatively and quantitatively. The AFM topography images shown in Figure 3.6 show interesting surface changes in surface quality as a function of growth temperature. At 600 °C, shown in the top left image, the step edges have poor definition and there are many islands of one unit cell thickness. At 620 °C, shown in the bottom left image, the step edges become better defined, and then nearly straight at

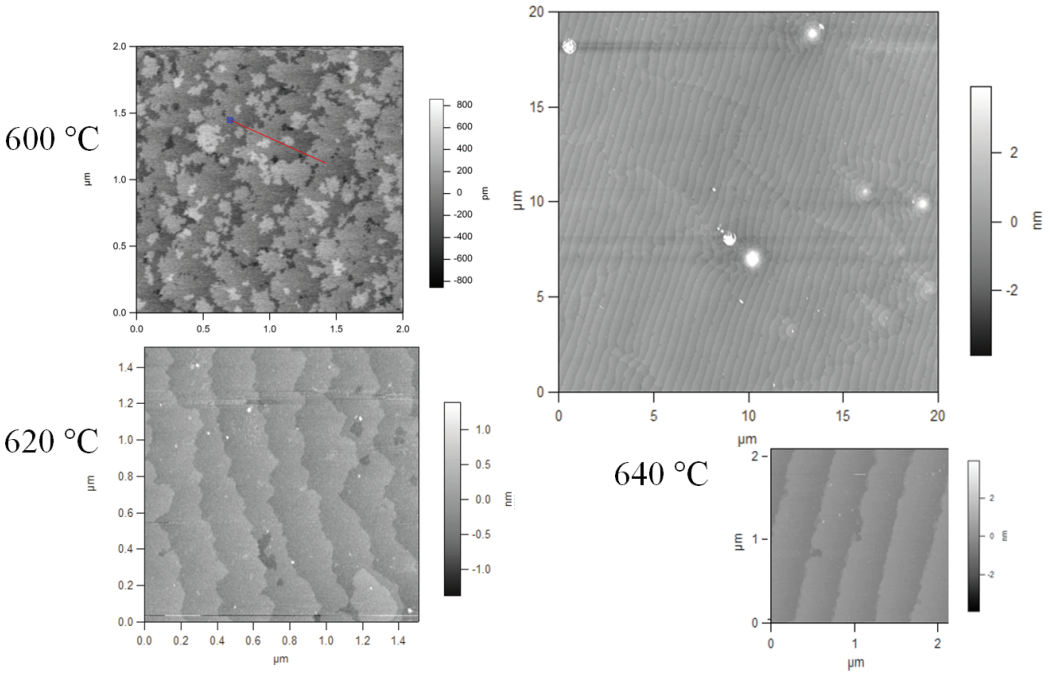

Figure 3.6: $SrRuO_3$ surface topography dependence on temperature. Top left is a $SrRuO_3$ film grown on $SrTiO_3$, while other images show growth on Nb-$SrTiO_3$, all with labeled growth temperatures.

640 °C, shown in the bottom right. However at 640 °C growth temperature, a larger area scan, shown in the top right image, we observe defects that resemble large pillars growing out of the surfaces, which would negatively affect films of other materials grown on top of this film. These features are not observed in larger area scans at the 620 °C growth temperature. The calculated RMS roughness of different films is difficult to assess, since the calculations depends on noise in the image, the particular area where roughness is measured, or if the surface is not perfectly clean, so the uncertainty is estimated at 30 pm in the table. We only see significant differences in surface roughness for the film grown at 640 °C and the 50 unit cell layer film. Since the 100 unit cell layer films exhibits the double unit cell layer steps, this results in a larger value of RMS roughness compared to the 50 unit cell layer film. The surface roughness of the 640 °C film also does not include the observed defects in this calculation, but it is interesting that outside of these defects, the lowest roughness is observed out of any of the 100 unit cell layer films. Based on these measurements and observations, the new growth temperature of 620 °C was used to grow $SrRuO_3$ bottom electrodes for samples grown after this study, owing to the superior electrical properties over films grown at 600 °C and better defined step edges. Later measurements also show this behavior for 100 unit cell layer films carries over to 50 unit cell layer films, and 50 unit cell layer films grown at 620 °C still exhibit single unit cell layer step growth.

Chapter 4

Structural Characterization

A variety of techniques can be used to characterize the structure of grown films and superlattices. X-ray diffraction and x-ray reflectivity are used to characterize the structural properties of films including the lattice parameters, crystal quality, and film thickness. Atomic force microscopy is used to measure the surface topography including roughness and whether the film follows the well defined step edges of the substrate. The film cross sections can be directly imaged using transmission electron microscopy, performed by our collaborator Dong Su at the Center for Functional Nanomaterials at Brookhaven National Laboratory.

4.1 X-Ray Diffraction

X-rays are scattered by electrons around ions in the crystal lattice. When these ions are periodically spaced, x-rays will scattered coherently at certain angles, giving rise to a diffraction pattern. X-ray diffraction follows Bragg's law, shown in Equation 4.1, and can be used to determine the distance, d, between planes of atoms in the crystal lattice.

$$n\lambda = 2d\sin(\theta) \tag{4.1}$$

In this equation, θ is defined as the angle of incidence of x-rays relative to planes of atoms, λ is the wavelength of x-rays, and n is the order, an integer number corresponding to the number of wavelengths involved in diffraction between atomic planes. In many diffractometers, the x-ray source and direction is fixed, so the Bragg condition is obtained by changing the sample angle, defined as ω in this work, and by changing the angle of the detector, defined as 2θ. For purely out-of-plane diffraction, corresponding to diffraction from $(00n)$ planes, ω is equal to θ.

X-ray diffraction in this work is performed using a Bruker D8 Discover diffractometer located in our lab or using the X21 or X22C beamlines at the National Synchrotron Light Source at Brookhaven National Laboratory. The Bruker D8 Discover produces x-rays by accelerating electrons into copper atoms, knocking out inner shell electrons. The resulting energy transitions give rise to x-rays with well defined energies. Various internal optics focus and select the copper Kα_1 emission line, which has a known wavelength of 1.5406 Å, and internal optics further direct x-rays towards the sample holder. After diffraction from the sample, x-rays are screened by either a combination of two slits, or a triple bounce Ge220 channel cut analyzer crystal. The triple bounce analyzer greatly increases the resolution of diffracted x-rays, since diffracted x-rays leaving the sample must undergo three diffractions in a Ge (220) oriented crystal before reaching the detector. Thus x-rays that are not incoming to the detector at a specific angle do not undergo diffraction from the analyzer crystal into the detector. Additionally, if x-rays with wavelengths slightly different from 1.5406 Å reach the sample and diffract towards the detector, these will also be screened by the analyzer crystal.

Prior to performing diffraction scans, the sample must be aligned by adjusting many of the angles shown in Figure 4.1 that are available in our diffractometer. When a sample is placed onto the sample holder in a diffractometer, it will often not be flat at zero degrees in ω relative to the x-ray beam and will not be in the center of the x-ray beam. The alignment procedure described in Appendix A.1 is used center the sample, finding the offsets from the nominal values in Z, ω, and 2θ angles that are used to perform future scans. After alignment is completed, a wider 2θ-ω scan can be performed to measure diffraction peaks from films or superlattices.

4.1.1 Rocking Curves

In addition to being used as an alignment scan, a rocking curve is performed to assess the crystallinity of substrates or grown films. Samples are typically positioned into the (001) diffraction condition of the substrate or Bragg diffraction peak of the film and then the 2θ angle is fixed into this position. A scan is performed by measuring diffraction intensity as a function of ω. An ideal single crystal will only yield a single diffraction peak with a narrow width. Defects such as facets, dislocations, or other structural anomalies will result in extra peaks or a broadened central peak. The crystallinity of a substrate or film can be quantified by calculating the full width at half maximum (FWHM) of a rocking curve peak. Ideally, a film grown epitaxially on a substrate should match the crystalline quality of the substrate, so rocking curves of films and superlattices are one way to assess the quality of the growth. In Figure 4.2, a

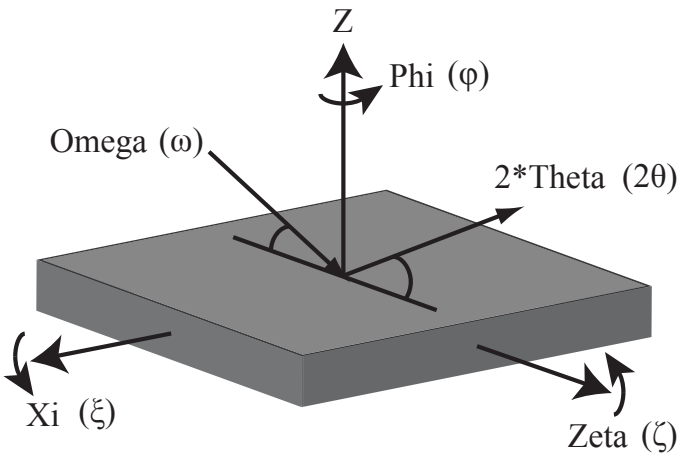

Figure 4.1: Adjustable angles used for sample alignment and x-ray diffraction scans.

rocking curve of a superlattice is scaled up and superimposed onto the rocking curve of the substrate. The matching of the FWHM of the superlattice with the substrate shows good quality epitaxial growth. The FWHM may depend on the resolution of the diffractometer and the optics used. The triple bounce Ge220 analyzer used to generate this diffraction peak has a much higher resolution than simple slits in front of the detector and is capable of measuring a 0.0032° FWHM on a Si111 crystal.

4.2 2θ-ω Scans

Scans of 2θ-ω maintain the Bragg diffraction condition by varying the 2θ angle at twice the rate as the ω angle. The 2θ-ω scan can be used to determine the average c lattice parameter and total thickness of a thin film, or can be used to determine the average c lattice parameter of a superlattice and the superlattice wavelength Λ, the thickness of the repeated structure in the superlattice. In some cases, 2θ-ω scans can be used to calculate the average c lattice parameter of each material in the superlattice.

Diffraction from a thin film of a single material results in an intense peak centered at a 2θ angle corresponding to the average c lattice parameter of the film according to Bragg's law 4.1. A number of fringes with decreasing intensities will arise around this peak, called Laue oscillations, due to the finite thickness of the film. A fitting program or simulation program is typically used to calculate the average c and film thickness, using these values as adjustable parameters. The spacings of the Laue oscillations are inversely proportional

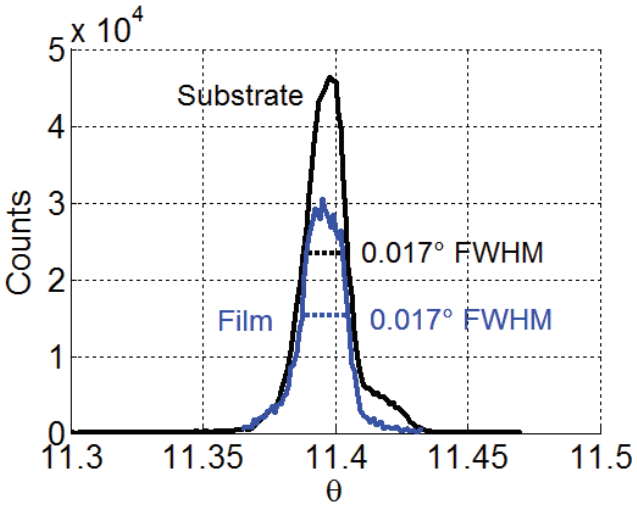

Figure 4.2: A scaled up rocking curve of a superlattice film overlaid unto a rocking curve of substrate of $SrTiO_3$ shows matching FWHM values.

to the film thickness, so as film thickness increases, the spacings between oscillations decrease. An example of measured diffraction scan of thin film of $SrRuO_3$ near the (001) $SrTiO_3$ with a simulated intensities is shown in Figure 4.3. The simulation calculates the diffracted x-ray intensities over a range of 2θ angles. In this figure, the best matching between simulated diffraction and the film diffraction is found using a c lattice parameter of 3.989 Å and total film thickness of 115 unit cell layers.

A typical superlattice diffraction scan is shown in Figure 4.4 for a 12/3 PTO/CTO superlattice around the (001) diffraction peak of the $SrTiO_3$ substrate. The most intense peak is from diffraction of the $SrTiO_3$ substrate, while the periodicity of the bilayers results in many diffraction peaks, with the most intense superlattice peak usually corresponding to the average c lattice parameter over the entire superlattice. In this figure, the most intense superlattice peak is labeled by 0, while the other superlattice peaks are labeled ± 1, ± 2, etc. The different superlattice peaks correspond to different orders n in Bragg's Law for the superlattice diffraction, but the order n is not immediately known here, so the labeling here is with respect to the most intense peak. Any two superlattice peaks in this graph can also be used to calculate the thickness of the repeated bilayer in the superlattice.

The new superlattice periodicity consisting of repetitions of two or more materials gives rise to the superlattice peaks seen in Figure 4.4. This periodicity enables diffraction equivalent to that of a unit cell with a c lattice parameter equal to the repeated thickness of the superlattice, which is called

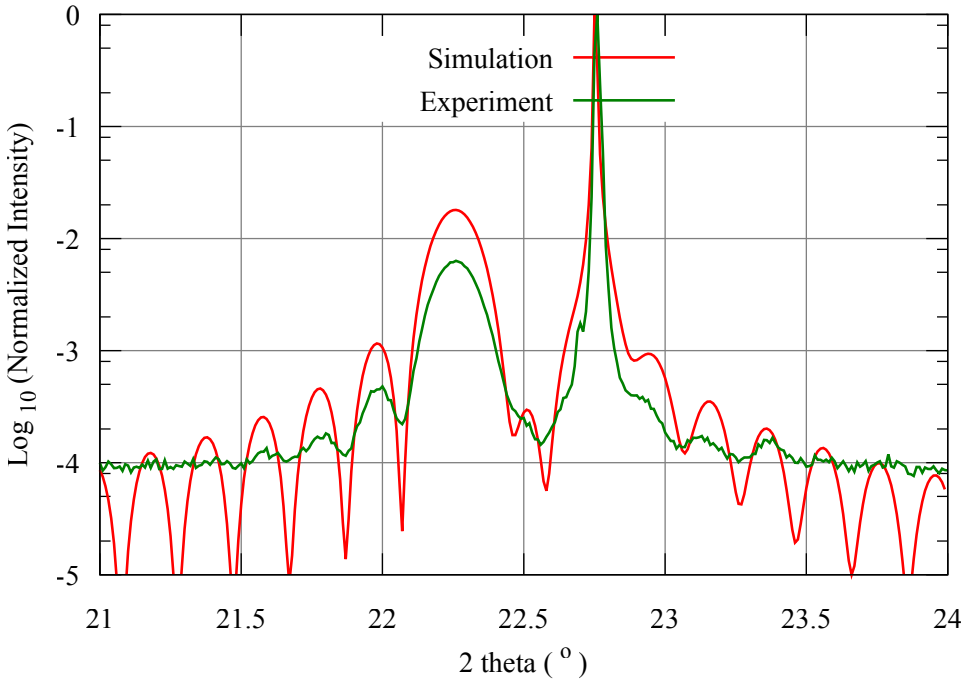

Figure 4.3: An x-ray diffraction scan of a $SrRuO_3$ film near the (001) $SrTiO_3$ peak is compared with a simulation of diffracted intensities. Adjusting the c lattice parameter and number of unit cell layers in the films changes the shape of the diffraction until the two are in agreement.

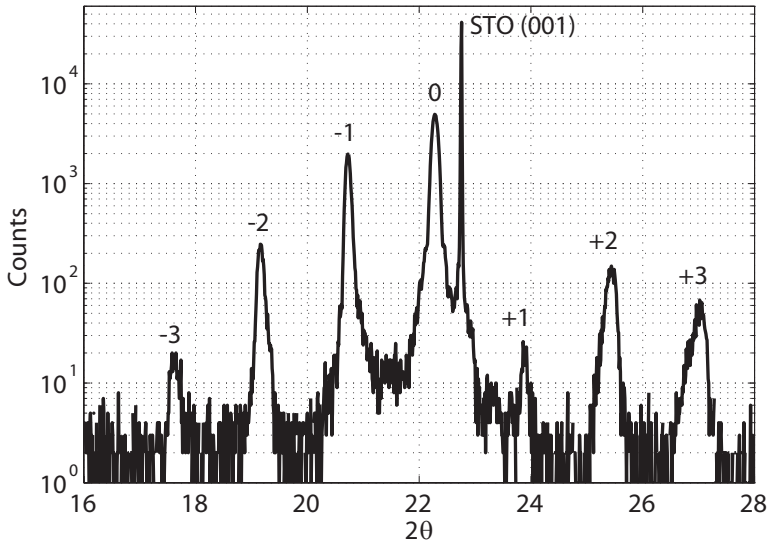

Figure 4.4: X-ray diffraction of a 12/3 PTO/CTO superlattice grown on $SrRuO_3$ on $SrTiO_3$ around the (001) $SrTiO_3$ diffraction peak. The main superlattice peak is labeled with a 0, while satellites are labeled ± 1, ± 2, and ± 3.

the superlattice wavelength, and denoted as Λ with units of Angstroms. For example, consider a bilayer of a PTO/CTO superlattice consisting of N unit cell layers of $PbTiO_3$ and M unit cell layers of $CaTiO_3$. Then the thickness of the bilayer is given by

$$\Lambda = (N)(c_{PTO}) + (M)(c_{CTO}) \tag{4.2}$$

where c_{PTO} and c_{CTO} are the c lattice parameters of $PbTiO_3$ and $CaTiO_3$ in the superlattice, respectively. However, a diffraction measurement usually cannot directly determine any of the values on the right side of this equation. Another expression for Λ arises from Bragg's law, since this new periodicity acts similarly to a unit cell with a c lattice parameter equal to Λ

$$n\lambda = 2\Lambda \sin(\theta_n) \tag{4.3}$$

where n is the order as before and θ_n the angle of the corresponding diffraction peak. Since Λ is typically much larger than the c of a unit cell of a given material in the superlattice, the diffraction peaks are much closer together in 2θ than substrate or film diffraction peaks of different orders. The problem

with Equation 4.3 is that when one measures a diffraction graph similar to Figure 4.4, it is not at all obvious what the order n is of a given superlattice peak, and furthermore, not all the orders are even measurable in a typical 2θ-ω scan.

A solution is to determine the value of Λ by ignoring the order of a given peak and instead using the 2θ angles of two adjacent superlattice peaks. Consider two adjacent superlattice diffraction peaks of order n and $(n-1)$. Then we have two equations from Equation 4.3

$$n\lambda = 2\Lambda \sin(\theta_n) \quad \text{and} \quad (n-1)\lambda = 2\Lambda \sin(\theta_{n-1})$$

and substituting the left equation above into the right equation above yields

$$2\Lambda \sin(\theta_n) - \lambda = 2\Lambda \sin(\theta_{n-1})$$

$$2\Lambda(\sin(\theta_n) - \sin(\theta_{n-1})) = \lambda$$

Solving for Λ yields

$$\Lambda = \frac{\lambda}{2(\sin(\theta_n) - \sin(\theta_{n-1}))} \tag{4.4}$$

So any two adjacent superlattice peaks can be used to determine a value of Λ.

The average c lattice parameter of the unit cells composing the superlattice is given by

$$\overline{c} = \frac{\Lambda}{(N+M)} \tag{4.5}$$

if the superlattice is composed of N unit cell layers of one material and M unit cell layers of another material, but this is complicated by the fact that superlattice growth does not typically result in integer values of N and M and these values are not known exactly since growth is imperfect. To avoid this issue, the average c over the superlattice can be calculated without knowing the values of N and M. Consider the previous equation 4.5 and now equation 4.3, but with the angle of some superlattice peak labeled as θ_{SL}

$$n_{SL}\lambda = 2\Lambda \sin(\theta_{SL})$$

and combine these to eliminate Λ, yielding

$$n_{SL}\lambda = 2\overline{c}(N+M)\sin(\theta_{SL})$$

or

$$\overline{c} = \frac{n_{SL}}{N+M}\frac{\lambda}{2\sin(\theta_{SL})}$$

If the order of the superlattice peak chosen divides the superlattice wavelength into parts equal to the number of unit cells, the $n_{SL}/(N+M)$ term is equal to 1. So if the correct superlattice peak is chosen, this simplifies to

$$\overline{c} = \frac{\lambda}{2\sin(\theta_{SL})} \tag{4.6}$$

As an example, consider the 12/3 superlattice of Figure 4.4. If the 15th order superlattice peak, which in this case is the most intense superlattice peak, is chosen for θ_{SL}, then the term $n_{SL}/(N+M) = 15/(12+3) = 1$, and so we obtain Equation 4.6. For each order of the substrate, there will be exactly one superlattice peak corresponding to $\overline{c}$ in this fashion, leading to Equation 4.6, and it is usually, but not necessarily, the most intense superlattice peak as we will see later.

If the superlattice is coherent with the substrate, meaning the film and the substrate have the same in-plane lattice parameters, then an average tetragonality $\overline{c}/a$ can be easily calculated from a 2θ-ω scan. The coherence of a film with the substrate can be determined by a (113) reciprocal space map or by other measurements of in-plane lattice parameters. The average c of the superlattice is calculated using the $\theta_{SL} = 2\theta_{SL}/2$ angle, while the c lattice parameter of the cubic substrate, equal to the a and b lattice parameters, are calculated using the θ angle of the substrate. Then for coherent films, the equation for $\overline{c}/a$ is given by

$$\frac{\overline{c}}{a} = \frac{\sin\theta_{Substrate}}{\sin\theta_{SL}} \tag{4.7}$$

$\overline{c}/a$ will be denoted as c/a for convenience, understanding it is an average tetragonality over all the unit cells composing a superlattice.

The reason why only some orders of superlattice diffractions are measurable is because the out-of-plane x-ray diffraction of superlattices is the convolution of the diffraction from each block of material and diffraction from the additional periodicity of the bilayers. Consider again the diffraction around the (001) substrate peak of a 12/3 PTO/CTO superlattice where the 12 layers of $PbTiO_3$ and 3 layers of $CaTiO_3$ are repeated 17 times, as shown in Figure 4.4. Each block of 12 $PbTiO_3$ unit cell layers results in an x-ray diffraction peak and Laue oscillations qualitatively similar to that of a $PbTiO_3$ thin film of 12 unit cell layers, but now with increased intensity due to the repetitions in the superlattice. The 2θ angle of this $PbTiO_3$ diffraction peak is determined by the average c lattice parameter of the $PbTiO_3$ in the superlattice. The 3 unit cell layers of $CaTiO_3$ also cause diffraction like the $PbTiO_3$ layers, but with

a maximum intensity at a 2θ angle determined by the average c lattice parameter of the $CaTiO_3$ in the superlattice, and this diffraction also convolutes with the $PbTiO_3$ diffraction peaks. Finally the many superlattice peaks with wavelength Λ convolute with the $PbTiO_3$ and $CaTiO_3$ peaks, and are most intense where the convolutions of the $PbTiO_3$ and $CaTiO_3$ peaks are most intense. The relative intensities of the $PbTiO_3$ and $CaTiO_3$ diffraction peaks drop off rapidly away from the maximum, and in turn greatly attenuate the superlattice peaks further from the central peaks.

For superlattices with small Λ it is generally not possible to resolve the diffraction from blocks of the same material, and so a c lattice parameter of each material in the superlattice cannot be directly calculated with accuracy. In general, large superlattice wavelengths Λ or very intense x-rays from a synchrotron radiation are required to resolve the broad diffraction peaks from each material block in the superlattice. For superlattices with small Λ, the diffraction from each block results in a very broad main peak, resembling a background on which the superlattice peaks lie. Additionally, at low angles or larger x-ray wavelengths, the angular separation between the diffraction peaks of the two materials is so small that the two diffraction peaks from each material to merge into a single, convoluted peak. The angular separation between diffraction peaks of the different materials can by increased by performing diffraction at larger angles, near the (004), or higher order diffraction peaks, for example, but then diffracted intensity is significantly less. If the superlattice wavelength Λ is larger, the intensity of diffraction peaks from each continuous material layer becomes larger relative to the superlattice peaks, and additionally the diffraction peaks from the blocks of the same material become much narrower. In this case it then becomes possible to measure the c lattice parameter of each material with careful calculations. Some illustrations of this behavior and examples are given in Appendix A.2. This behavior additionally explains why, for superlattices in this work, the main superlattice peak is almost always the most intense superlattice peak, which is due to the small superlattice wavelengths, Λ, and low angle diffraction scans performed.

Actual superlattice growth typically results in superlattices where the average number of unit cell layers is not exactly an integer. This can happen if the interfaces between the materials have a small shortage or excess of ions for each of the materials in the superlattice. Then the average thickness of a block of material in the superlattice is found to have a fractional value. For example, the 12/3 PTO/CTO superlattice of Figure 4.4 has 2θ peaks of the substrate, SL_0, SL_{-1} at values of 22.756°, 22.283°, and 20.729°, respectively. Using Equations 4.4 and 4.6 yields Λ=57.82 Å and $\overline{c}$=3.986 Å, which imply that the average number of unit cells in the superlattice bilayer is 14.51, less

than the expected 15 unit cell layers. It is not readily apparent from an x-ray diffraction scan which of the materials in the superlattice was not grown long enough, or perhaps both materials were not grown long enough. But, by comparing growth of several superlattices in series, a measured growth rate of each material can be calculated, which when combined with the known growth times of each material, results in a calculated fractional number of unit cell layers for each material. In this case, using the growths of superlattices grown in series with the 12/3 superlattice, the average number of unit cell layers of $PbTiO_3$ was calculated to be 11.69, while the number of unit cell layers of $CaTiO_3$ was calculated to be 2.82, which means that each continuous block of material in the superlattice had a shortage of material, relative to the desired integer number of unit cell layers 12 and 3, respectively.

The non-integer number of unit cell layers in turn causes some issues with using Bragg's Law as stated and either the previous definitions need to be modified or additional constraints need to be added to the diffraction equations, in particular if one wishes to calculate the order n. If we want to calculate the order n of the most intense superlattice peak, which will be referred to as n_{SL0}, using Equation 4.3, we find n_{SL0}=14.51, or again, the number of unit cells on average that composes the bilayer, even though the order n here is not an integer as in Bragg's Law. The order n of the SL_{-1} peak calculated in the same way yields n_{SL-1}=13.51, or exactly one less than the 14.51th order. Clearly not every possible n in this equation yields a superlattice diffraction peak, but the different orders still differ by integer values. So the Bragg diffraction equation would not be valid for any integer n, but for some n provided it is different from other orders by integer values. However, the interpretation of the order n here has no bearing on the primary equations used to characterize superlattices, since equations for $\bar{c}$ (4.6), c/a (4.7), and Λ (4.4) do not contain the order n. Equations deriving (4.6) had the order n and the number of unit cells $(N+M)$ of each material, but this term still equals 1 and drops out in the case of fractional orders and fractional unit cell layers, so the final equation is unchanged. Another interpretation of the non-integer orders in relation to Bragg's Law is discussed in Appendix A.3.

4.3 X-ray Diffraction Simulation

Bragg's Law for superlattices is not exact, but has a small amount of error due to the convolution of superlattice diffraction peaks with the underlying finite size effects peaks of the material layers, slightly shifting the diffraction peaks in 2θ. If the superlattice peak is positioned on the left or right side of an underlying peak, the diffracted intensity from the superlattice periodicity

will be skewed, shifting down the slope of the underlying peak. This effect is more pronounced if a superlattice peak is positioned over a $SrRuO_3$ bottom electrode size effect peak, which typically has a much larger intensity than the underlying superlattice material layer peaks. These shifts in 2θ are almost always smaller than the differences in 2θ from resulting from different sample composition, so Bragg's law is still a good approximation. However, simulations can provide more accurate measurements of c lattice parameters and superlattice wavelengths.

The diffracted x-ray intensities at an angle 2θ from a thin film or superlattice can be directly calculated from structure factors, which if correctly calculated, take into account the various convolution effects. The scattered x-ray intensity from a crystal depends on the periodic arrangement of electrons around the ions, which is described by the structure factor, and the scattered x-ray intensity depends on the angle and wavelength of the incoming x-ray [44]. The incident and scattered x-rays can be written in terms of the scattering vector, or momentum transfer vector, $\boldsymbol{q} = \boldsymbol{k}_f - \boldsymbol{k}_i$, where $\boldsymbol{k}_i$ is the incoming x-ray wave vector and $\boldsymbol{k}_f$ is the outgoing scattered wave vector. The measurement angle 2θ is can be calculated from $\boldsymbol{q}$ by

$$|\boldsymbol{q}| = q = \frac{4\pi \sin\theta}{\lambda} \tag{4.8}$$

The scattered x-ray intensity is related to the structure factor $S(\boldsymbol{q})$ of a unit cell, which is defined as

$$S(\boldsymbol{q}) = \sum_{\boldsymbol{r}_j} f_j(\boldsymbol{q}) e^{i\boldsymbol{q}\cdot\boldsymbol{r}_j} \tag{4.9}$$

where the sum is taken over the positions of the ions $\boldsymbol{r}_j$ in the unit cell, and $f_j(\boldsymbol{q})$ is the atomic form factor, which is a measure of the scattered x-ray intensity depending on the electron density about a given ion. Expressions for the atomic form factors for various ions can be found in the International Tables of Crystallography [56]. The positions of the ions in the lattice, $\boldsymbol{r}_j$, can be taken as those for a tetragonal perovskite crystal structure, and the lattice parameters of the unit cells are then the parameters which are adjusted to find the best correspondence between experiment and simulation. The scattered x-ray intensity as a function of $\boldsymbol{q}$ is then proportional to

$$\text{Intensity}(\boldsymbol{q}) \, \alpha \, |S(\boldsymbol{q})|^2$$

which is then related back to a measurement angle at θ or 2θ using Equation 4.8.

These equations were implemented within an online with simulation pro-

gram (written by Matthew Dawber) and used in this work in order to accurately find the lattice parameters from a given diffraction scan, and produce comparisons between measured x-ray diffraction with calculated x-ray diffraction as in Figure 4.3 and others in the appendix. For each angle 2θ, the relative diffraction intensity was calculated from a either a superlattice, thin film, or both for when superlattices are grown on $SrRuO_3$ electrodes. The various equations are calculated from user defined values of c lattice parameters, type of materials, and number of unit cell layers. The previous equations can be simplified for the case of thin films, and the diffraction intensity of the substrate can be calculated through the use of an extinction parameter [75]. The simulations of superlattices with non-integer numbers of unit cell layers is calculated from the total structure factor of the entire superlattice in the out-of-plane direction. For a given simulation, the user defines the c lattice parameter of each material, and the number of unit cell layers of each material in the repeated superlattice, which may be a fractional number of unit cell layers. The superlattice "unit cell" (in fact, the entire sample) is then constructed by the program by essentially building up the composition of a given layer by taking into account the amount of material that has been deposited so far, and how much of each material is available during the deposition of that layer. Simulations performed in this way show a very good matching with experimental results, and can be used to accurately calculate the average c lattice parameter of the superlattice and estimate the number of unit cell layers of each material in the superlattice, even when non-integer numbers of unit cells are deposited for each material.

4.4 X-ray Reflectivity

Another method to determine the thickness of a film is to perform low angle x-ray reflectivity measurements. The finite thickness of the film gives rise to intensity oscillations as seen in a 2θ-ω scan performed at low 2θ angles. The intensity oscillations have spacings that are related to the thickness of the film. If one assumes a dynamical formulation of x-ray reflection as in [59], and assumes a small angle of incidence of x-rays to the surface, the relationship between the thickness, t, and oscillations is given by the following approximation

$$\alpha_{im}^2 - \alpha_c^2 = m^2 \left(\frac{\lambda}{2t}\right)^2 \tag{4.10}$$

where α_{im} is the angle of incidence giving rise to an oscillation peak in units of radians, α_c is the critical angle, m is an integer, and λ is the wavelength.

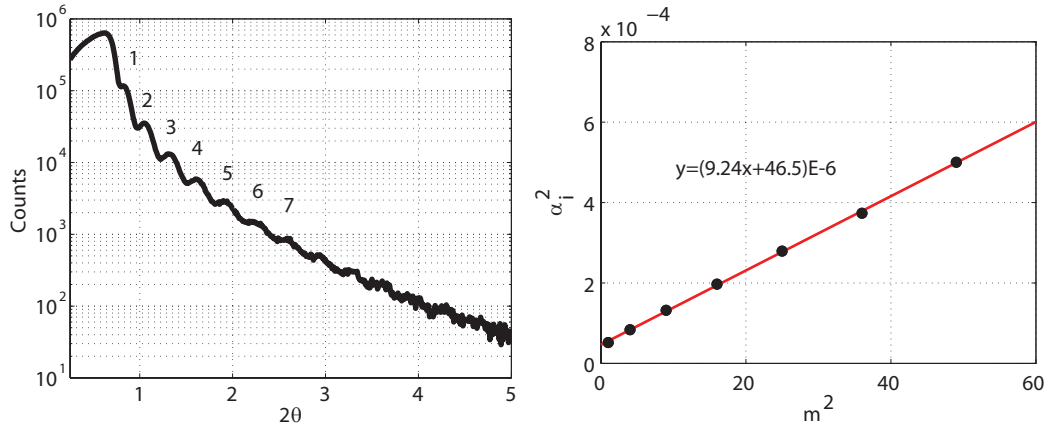

Figure 4.5: (Left) X-ray reflectivity of a $SrRuO_3$ film and (Right) linear regression of α_{im}^2 vs m^2 used in the film thickness calculation.

To calculate a t using all the measurable oscillations, consider Equation 4.10 as a general linear equation $y = sx + b$, then by linearly fitting this equation to the oscillations, we use the slope of the line s to determine the thickness

$$t = \frac{\lambda}{2\sqrt{s}} \tag{4.11}$$

An example use of this equation with a reflectivity measurement is shown in Figure 4.5. The 2θ angles labeled 1-7 are recorded, divided by 2 to yield the angle of incidence, then converted into radians. These values of α_{im}^2 are then plotted vs m^2 and fit with a linear using linear regression. The resulting slope and the wavelength λ=1.5406 Å is used in Equation 4.11 to yield a film thickness of 253 Å.

4.5 Reciprocal Space Maps

X-ray diffraction maps in reciprocal space can be made by a number of 2θ-ω scans, sometimes at nonzero values of ϕ, and can be used to determine periodic domain structure, relaxation effects, or small scale splittings of superlattice peaks. A complete derivation of reciprocal space formulation can be found in many standard solid state physics textbooks [4, 44], but only the specific cases of tetragonal and cubic crystals are summarized here. For tetragonal crystals,

if the real space lattice vectors are given by

$$\boldsymbol{R} = n_x a\hat{x} + n_y a\hat{y} + n_z c\hat{z}$$

where n_x, n_y, and n_z are integers, then the reciprocal lattice vectors of the tetragonal crystal are given by

$$\boldsymbol{G} = h\frac{2\pi}{a}\hat{x} + k\frac{2\pi}{a}\hat{y} + l\frac{2\pi}{c}\hat{z}$$

where a and c are the lattice parameters, and h, k, and l are Miller indices (hkl), integers corresponding to different atomic planes in the crystal. When performing x-ray diffraction, the incoming and scattered x-rays define a plane. So it is useful to define reciprocal lattice units in two dimensions, Q_z and Q_x, which are computed for tetragonal crystals by

$$Q_x = \frac{2\pi(h^2 + k^2)^{1/2}}{a} \tag{4.12}$$

$$Q_z = \frac{2\pi l}{c} \tag{4.13}$$

and Q_x and Q_z typically have units of 1/nm or 1/Å. A reciprocal lattice vector $\boldsymbol{G}$ is related to the angle of incidence of diffracted x-rays, and spacings d between adjacent planes by the equations

$$|\boldsymbol{G}| = \frac{4\pi \sin\theta}{\lambda} = \frac{2\pi n}{d}$$

These equations given can be used for cubic crystals and are readily computed for $SrTiO_3$ substrates with known lattice parameters of $a = b = c$ =3.905 Å at room temperature.

The Bruker D8 Discover diffractometer utilizes software containing these equations and others in order to perform scans over reciprocal space. To perform scans in reciprocal space, it is necessary to know the lattice parameters of a given crystal and its crystal type. Since the lattice parameters of $SrTiO_3$ substrates at room temperature are known to be 3.905 Å and $SrTiO_3$ is cubic, the program can use this information to compute the real space angles of 2θ, ω, and ϕ corresponding to different (hkl) reflections. Maps in this work are typically performed around the (113) or (103) reflections of the substrate. A 2-D map of reciprocal space can be defined in terms of h and l or in terms of Q_x and Q_z. The user defines an area in reciprocal space and number of divisions in each dimension, and the program will then calculate the angles of ω and 2θ for each coordinate and measure the intensity at each coordinate

in the area for a specified length of time. The alignment procedure is a little different than for 2θ-ω, especially when non-zero values of ϕ are used. The alignment procedure described in Appendix A.1 uses the ξ and ζ angles in order to flatten the sample with respect to the incoming x-rays, even under rotations of ϕ.

Figure 4.6 shows a (113) map of reciprocal space of an 8/3 PTO/CTO superlattice in the vicinity of the (113) $SrTiO_3$ substrate diffraction peak. The $h = k$ and l coordinates of the map are defined by basis vectors of the substrate, so by definition, the substrate peak is located at the (113) position. The superlattice peaks appearing on this map are then readily compared to the substrate, as differences in lattice parameters result in different values of h, k, and l of the superlattice. The differences along the l direction, or the y-axis here, of the superlattice peaks is related to the c lattice parameter of the superlattice. Additionally many superlattice satellite peaks appear here along the l axis much like in one dimensional 2θ-ω scans along the (001) or (002) directions. The substrate peak and superlattice peaks lie along the same value of $h = k$, meaning they have the same a and b lattice parameters, and so the growth is coherent. If the superlattice peaks were at a different value of $h = k$ from the substrate $h = k$ value, this would imply the in-plane lattice parameters of the superlattice do not match those of the substrate, indicating a relaxation process has taken place. Reciprocal space maps around a film peak may also show additional diffraction peaks with a different h, k compared to the substrate, as shown in Figure 4.7. These are identified as periodic domain structures, with the domain periodicity determined by the distance away from h=1 here. These two peaks correspond to regions of polarization where the crystal is contracted slightly along the in-plane direction at larger h values or contracted along the in-plane direction at larger h values.

Using equations 4.12 and 4.13 we can compute the lattice parameters of the superlattice and the periodicity of the domains from these reciprocal space maps. First, using the known lattice parameters of the $SrTiO_3$ substrate, the coordinates of any position in $h = k$ and l can be converted into reciprocal lattice units from Equations 4.12 and 4.13. The coordinates of the main superlattice peak can then be identified, corresponding to the average lattice parameters over the superlattice, and is converted into reciprocal lattice units. Since this main peak is near the (113) peak of the substrate, the main superlattice peak is the (113) peak in the basis vectors of the superlattice. Therefore Equations 4.12 and 4.13 are used again with the previously calculated Q_x and Q_y, h=k=1 and l=3, and then the lattice parameters can now determined by these equations. This process can actually be simplified to directly obtain the superlattice lattice parameters based on the substrate lattice parameters.

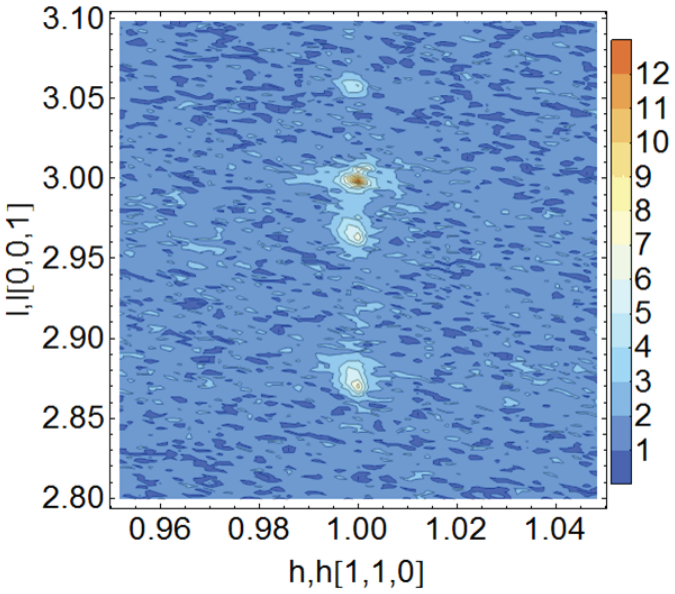

Figure 4.6: A (113) reciprocal space map of an 8/3 PTO/CTO superlattice on $SrTiO_3$

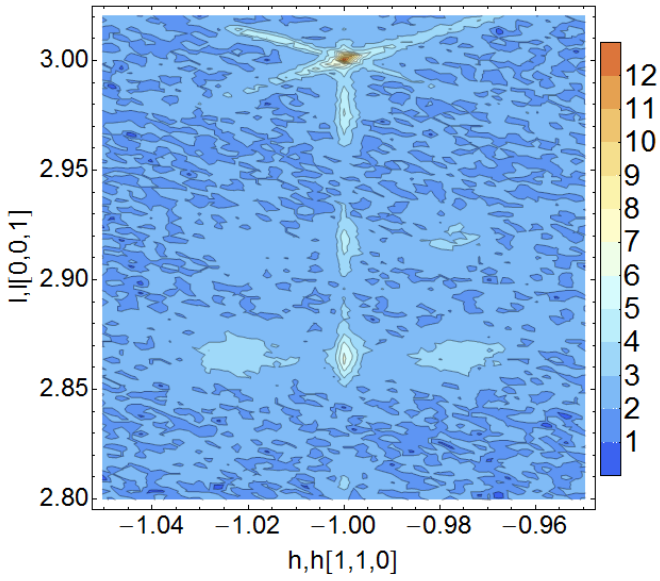

Figure 4.7: A (113) reciprocal space map of a 15/3 PTO/CTO superlattice on $SrTiO_3$ with a $SrRuO_3$ bottom electrode that showing periodic domain structure.

Using the procedure just described

$$\frac{2\pi l_{SL}}{c_{substrate}} = Q_x = \frac{2\pi l'}{c_{SL}}$$

where l_{SL} is the l value of the superlattice in the reciprocal space map, defined by the substrate basis, and l' is the l value of the superlattice in the basis of the superlattice, which is 3 for the case of a (113) reflection. This simplifies to

$$c_{SL} = \frac{l' c_{substrate}}{l_{SL}} \tag{4.14}$$

Using the values from Figure 4.6, which shows the main superlattice peak at l=2.97, and the known substrate lattice parameters,

$$c_{SL} = \frac{3 \times 3.905\,\text{Å}}{2.97} = 3.944\,\text{Å}$$

is the calculated average c lattice parameter of the superlattice. The domain periodicity can be calculated in a similar manner, based on the spacings of the domains imaged in Figure 4.7. This is accomplished by using the distance between the h=k value of the domain and the h=k=1 value of the substrate. The domain periodicity is given by [11]

$$\frac{2\pi}{\Delta Q_x} = \frac{a}{\Delta h\sqrt{2}} = \frac{3.905\,\text{Å}}{0.025\sqrt{2}} = 110\,\text{Å} \tag{4.15}$$

for a domain spacing Δh in a (11l) map. This equation also illustrates numerically that increased differences in h between domains and the substrate correspond to smaller domain periods in the in-plane direction.

4.6 Atomic Force Microscopy

Atomic force microscopy (AFM) is used to measure the topographical features of films and substrates. Atomic force microscopes use a cantilever with an attached tip that is moved across the surface typically being in direct contact with the surface or "tapping" the surface. In the tapping mode, the cantilever and tip is driven near its resonant frequency. The changing surface features underneath the tip create a force on the tip, deflecting it in different ways. Light from a laser or a superluminescent diode is reflected off the top surface of cantilever towards a photosensor, which measures the changing positions of the reflected light. When this measurement is combined with various feedback

loops driving the tip, the surface topography can be accurately reconstructed. Since deflections are very small, measurements require vibrational noise to be low and further screened using various active and passive components.

Measurements in this work are performed an Asylum MFP-3D-SA microscope controlled with software provided by the manufacturer. Topography scans are performed using the AC tapping mode and typically with cantilevers having roughly a 325 kHz resonant frequency and a tip size of 10-20 nm in diameter. Topography scans are performed in repulsive mode, meaning the driving frequency of the tip and cantilever is just below its resonant frequency, resulting in better image quality for our samples. The scan areas typically range from 1 micron squares to 40 micron squares. Samples must have clean surfaces or else dust or other particles are imaged or can interfere with the tip and produce artifacts. So samples are cleaned in an ultrasonic cleaner with acetone and ethanol to remove debris from the surface. If that process fails, a Kimwipe with ethanol or a Q-tip with ethanol is gently brushed over the surface, removing the remaining particles, but this comes at the risk of scratching the sample.

Ideally, films grown will match the same step and terrace structure of the substrate and continue to have well defined step edges. An AFM topography image of a $SrTiO_3$ substrate was shown in Figure 3.4 which clearly shows the step edges due to the miscut angle. The height of these steps can be measured with the AFM to be approximately 4 Å, in agreement with the unit cell height of $SrTiO_3$ of 3.905 Å. Films grown should ideally match this unit cell step structure, which can be verified by AFM scans. Additionally, the RMS surface roughness can be measured to quantitatively assess the smoothness of the grown film surface.

4.7 Transmission Electron Microscopy

The arrangement of the ions in a cross section of thin films and superlattices can be imaged using high resolution scanning transmission microscopy (HR-STEM). The sample preparation and measurements in this work were performed by Dong Su at Brookhaven National Laboratory. Samples are prepared using Ar ion milling to carve out a section of a superlattice and substrate that measures about 10 microns in width, a few microns in height including the superlattice and much of the substrate, and then only a few hundreds of nanometers in length. Transmission electron microscopy is performed by directing an electron beam towards the thin film or superlattice cross section and measuring the response due to diffraction and other effects. HR-STEM uses a highly focused aberration corrected electron beam that is scanned over

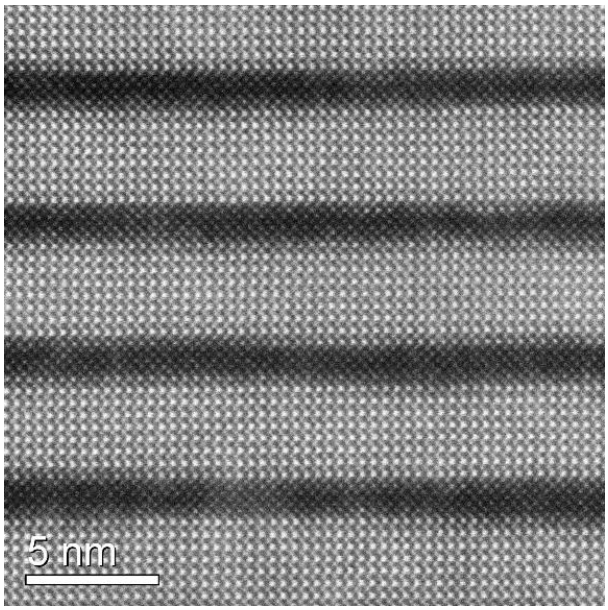

Figure 4.8: A high resolution scanning transmission electron microscopy (HR-STEM) image of an 8/3 PTO/CTO superlattice. A close inspection of the $PbTiO_3$ unit cells show a lateral displacement of the Ti ions with respect to the Pb ions, indicating polarization with a component in the in-plane direction.

the sample and allows for very accurate measurements of the atomic positions. By use of a high angle detector, it is also possible to distinguish between atoms of different atomic number (Z-contrast imaging). An HR-STEM image for an 8/3 PTO/CTO superlattice is shown in Figure 4.8. The contrast in brightness is related to the atomic number of the atoms, with the brighter layers corresponding to Pb ions, and the darker layers corresponding to Ca ions. We observe well defined superlattice layers in this cross-sectional image. HR-TEM is also capable of imaging relaxation or defects, but these are not seen in Figure 4.8.

Chapter 5

Electrical Characterization

Various electrical properties of ferroelectrics are measured with the application of electric fields across a sample including the dielectric constant, polarization, coercive fields, and piezoelectric coefficient.

In order to apply electric fields, it is necessary to have electrodes in contact with both sides of the sample, or have a conducting substrate to be used as an electrode, such as Nb-doped $SrTiO_3$. $SrRuO_3$ is useful for a bottom electrode due to its perovskite structure with small lattice mismatch when grown on $SrTiO_3$, and its lower resistivity than Nb-doped $SrTiO_3$. If $SrRuO_3$ is grown as a top electrode, it must later be etched into smaller electrode sizes. Gold is an alternative top electrode that may be easily sputtered into small electrodes with the use of a shadow mask after film growth. A shadow mask is a physical mask placed over the sample with a number of holes. Sputtered gold is then only deposited through the holes and onto the sample, resulting in the pattern shown in Figure 5.1. Top electrodes should have a relatively small area for reliable measurements since grown films may contain a localized conductive defects leading to electrical shorts. If a few defects are randomly distributed across the film, then larger area electrodes have an increased probability of containing one of these defects, resulting in an electrical short that would prevent electrical measurements on the electrode. Top electrodes used in this work are all gold electrodes applied ex-situ, while bottom electrodes are 20 nm thick $SrRuO_3$ films grown in-situ on top of the substrate and before a film or superlattice is grown. Some samples in this work have $SrRuO_3$ and Nb-doped $SrTiO_3$ as a bottom electrode, but since the circuit resistance of Nb-doped $SrTiO_3$ is about ten times larger than $SrRuO_3$, the Nb-doped $SrTiO_3$ only has a negligible effect on the circuit.

The type of electrode material used with a ferroelectric film will have an effect on the measured properties of the system. Measurements of polarization and dielectric constant measure the properties of the entire circuit including

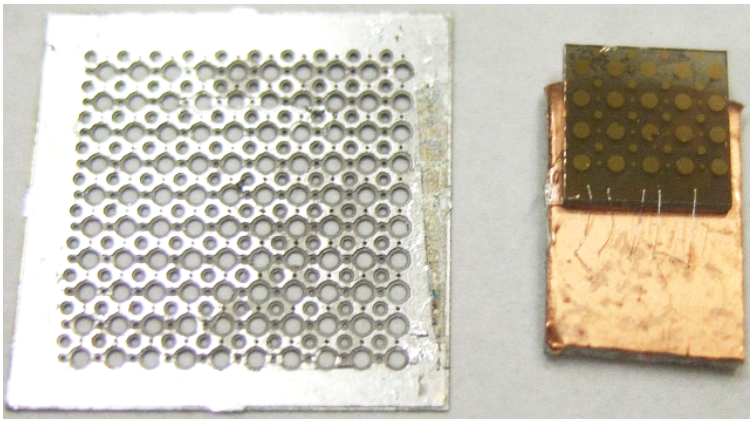

Figure 5.1: (Left) A shadow mask used to produce gold top electrodes. (Right) A sample with gold electrodes mounted onto copper with wirebonds connecting the $SrRuO_3$ bottom electrode to the copper.

the wires and electrodes, which can include a small amount of extra resistance in series or interfacial capacitances at the interface of the electrode and ferroelectric [17]. Many of the electrical measurements in this work have an asymmetry between positive and negative voltages due to the different electrode material on the top and bottom of the film [73].

In order to connect measurement devices to the electrodes, it is necessary to make connections with the bottom $SrRuO_3$ electrode and the gold top electrodes. Samples are mounted onto a small piece of copper coated PVC using double sided tape. A West Bond 7400 series wirebonder bonds aluminum wire from the copper base to the $SrRuO_3$ electrode. The machine creates a bond on each end of the wire using ultrasound, and this bond penetrates through the ferroelectric thin film to the underlying electrode and substrate. Connections are then made to the copper base and to a particular gold top electrode using a Signatone S-1160 probe station that uses tungsten probe needles connected to wires through BNC connectors.

Measurements of the polarization and dielectric constant depend on the electrode area, determined by the area of the top gold electrodes. The shadowmask used to produce gold electrodes provides four different sized electrodes of diameters of approximately 500, 250, 125, and 55 microns. However due to the variable way the shadowmask is placed over samples, the sputtered gold electrodes may differ in size by up to 7% from one another. Since this would negatively impact polarization and dielectric constant calculations, each electrode used for electrical measurements had its area measured to within 1% error using a calibrated digital microscope with computer measurement soft-

ware.

5.1 Ferroelectric Polarization

Ferroelectric polarization can be measured in an electrode and film system by applying negative and positive voltage pulses to switch the polarization direction while simultaneously measuring the current response. Ferroelectric polarization is screened at the sample surface by charge in the electrode and wire circuit. When the polarization direction is switched, the screening charge shifts, creating a current spike proportional to twice the polarization and this can then be measured using an amplifier and oscilloscope. It is later shown the measured current response contains current from other effects in addition to polarization switching, but as an approximation for now, assume that the measured current, $I(t)$, only contains polarization switching current. Then the integral of the current in time, yields charge as a function of time,

$$Q(t) = \int I(t)dt \tag{5.1}$$

and when divided by the electrode surface area, A, yields twice the polarization as a function of time,

$$2P(t) = Q(t)/A \tag{5.2}$$

Polarization is then plotted against the applied voltage in time, $V(t)$, obtaining a hysteresis loop. An example of a hysteresis loop obtained from a sample of PZT is shown in Figure 5.2. The y-intercepts of the loop define the remnant polarization. The graph is centered about the y-axis because switching the polarization from one state to another yields charge proportional to the difference $P_{up} - (-P_{down}) = 2P$. The coercive field, or the field at which the polarization switches, is defined as the intercept of the loop with the x-axis.

Many samples tend to be not as ideal as Figure 5.2 and additional current in the system may arise from leakage, dielectric charging, or unstable polarization, which cannot be easily distinguished from ferroelectric switching current. Leakage is the movement of charge through the sample due to low sample resistance or other conduction processes. Samples also tend to have diode-like characteristics where leakage increases rapidly at large voltages or high fields. Insulating ferroelectric samples with electrodes also have a linear dielectric response that will yield a charging current in response to a ramping voltage. When voltage is changed across a capacitor a dielectric charging

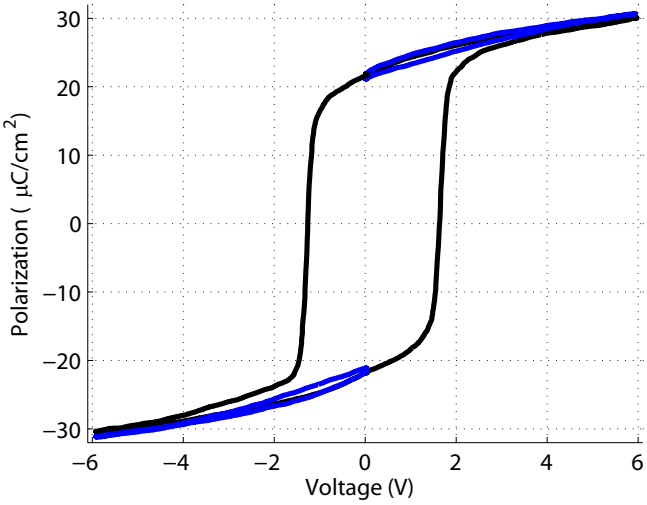

Figure 5.2:]
A hysteresis loop on a sample of PZT. The black lines are the response to applying pulses that switch the polarization while blue lines are the response to applying voltages in the same polarization direction.

current, is produced according to

$$I_{charging}(t) = C(V)\frac{d}{dt}(V(t)) \tag{5.3}$$

where V(t) is the voltage applied in time, and $C(V)$ is the magnitude of the capacitance as a function of the applied voltage. In contrast to linear dielectrics, the capacitance of a ferroelectric is typically strongly dependent on the magnitude of the applied field and additionally the polarization state.

In order to separate the ferroelectric switching current from other sources of current in the measurement, a pulse sequence known as PUND (Positive Up Negative Down) can be used. PUND measures a polarization value similar to remnant polarization, but subtracts out potential artifacts from leakage and dielectric charging. In this technique, a negative voltage pulse is first applied to switch the sample into the down polarization state, then four pulses are applied with the associated current responses are measured, as shown in Figure 5.3. The first measurement pulse, labeled as "P" in the diagram, switches the polarization into the up state, and the measured current response of the circuit will originate from both ferroelectric switching and other current sources. A second up pulse in the same direction, labeled as "U", should ideally only produce current due to dielectric charging, leakage, or other non-

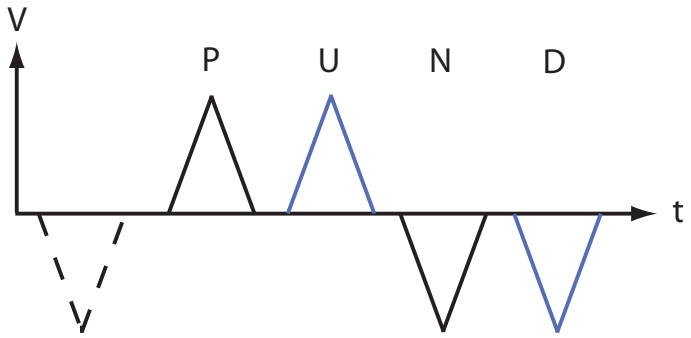

Figure 5.3: The PUND pulse sequence is used to separate ferroelectric switching current from other sources of current.

ferroelectric currents, since the ferroelectric is still in the same up polarization state. The non-ferroelectric switching current from the "U" pulse can then be subtracted from all current measured from the first "P" pulse, in order to isolate the ferroelectric switching current. The third and fourth pulses, "N" and "D", are applied similarly, and are used to isolate the ferroelectric switching current associated with switching from the up polarization state into the down polarization state.

Measurements are performed at different frequencies or voltage ramp rates to reduce artifacts. Ideally, the PUND technique should measure the same polarization value over a large range of voltage ramp rates, since currents due to other sources are subtracted. However, numerous problems can arise that PUND cannot account for well: when leakage becomes very large, subtraction may not work properly, a large in-series resistance with the ferroelectric can skew the measurement, or unstable polarization may result in backswitching of the ferroelectric. At lower frequencies or smaller voltage ramp rates, the amount of leakage current relative to ferroelectric switching current is greater. This is because the integrated ferroelectric switching current peak adds up to a fixed amount of charge, while the amount of current through a leaky ferroelectric depends on the length of time and magnitude of the applied voltage. If the sample acts like a resistor, then $V = IR$, and so the measured charge due to leakage is proportional to

$$Q_{leakage}(t) = \int \frac{V(t)}{R} dt \tag{5.4}$$

for a linear resistive circuit element, implying longer voltage pulses will yield additional leakage charge. Note that the resistance of a ferroelectric is typically dependent on the applied field and is nonlinear, but that does not change the

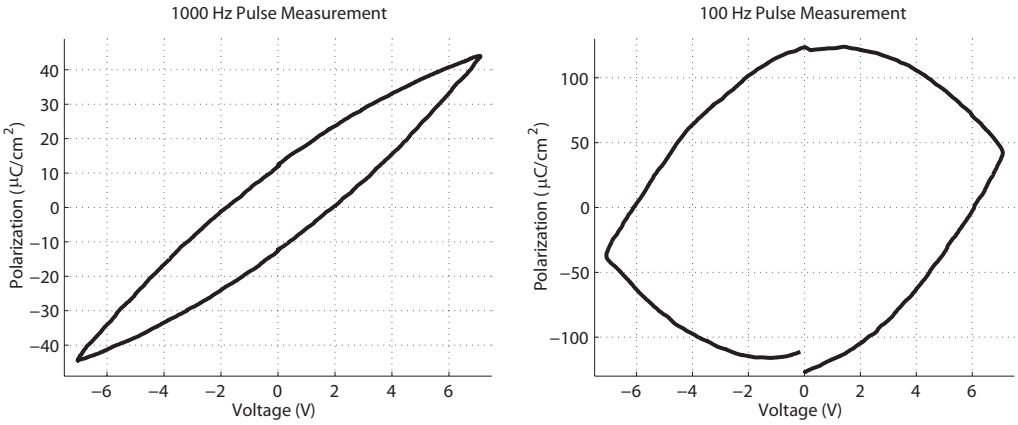

Figure 5.4: The response of a resistor and capacitor in parallel can resemble at hysteresis loop at some applied voltage frequencies. The graph on the left, measured at 1000 Hz frequency, resembles a polarization hysteresis loop. However, this same system measured at a slower, 100 Hz frequency, shown on the right, is clearly not a hysteresis loop, demonstrating the importance of measuring at different frequencies or using PUND.

fact that measurements on longer time scales will generate more leakage charge. Even with this complication, if leakage and dielectric charging can be measured directly and subtracted out of the measurement, the same polarization will be measured at various frequencies.

If PUND or similar techniques are not performed to separate the various currents, measured values of "polarization" can greatly change with voltage ramp rates [67]. A traditional measurement of ferroelectric polarization involves simply ramping from high positive field, to high negative field, and back to zero volts. This is extremely susceptible to artifacts, which would be readily seen by repeating the measurement at different frequencies or voltage. Using measurements performed in this way, it is actually possible to obtain a measurement loop that resembles a ferroelectric hysteresis loop by measuring a capacitor and resistor in parallel at some particular frequencies, as shown in the left graph in Figure 5.4. When the voltage ramp rate or frequency is reduced by a factor of ten, the leakage charge through the resistor is much larger, yielding a very different "polarization" loop, shown in the right graph of Figure 5.4. When PUND is used on this resistor and capacitor combination, P and U parts of the signal are identical to each other and the N and D parts are also identical to each other, so after subtraction, no ferroelectric polarization is measured.

PUND does not separate switching currents of the stable and unstable

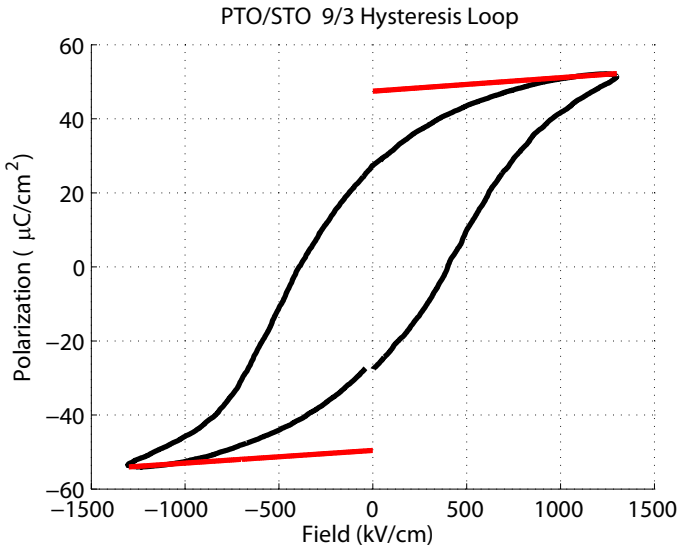

Figure 5.5: A traditional hysteresis loop measurement for a 9/3 PTO/STO superlattice. The intersection of the red fitted lines with the y-axis defines the spontaneous polarization.

ferroelectric polarizations, but instead measures a stable polarization at zero applied field, similar to remnant polarization, but without artifacts. Unstable polarization is defined here as regions of polarization that change orientation as the field is ramped from high field down towards 0 volts. Traditional measurements quantify both stable and unstable polarization by defining a term known as the spontaneous polarization. The spontaneous polarization is calculated by fitting the dielectric charging part of the hysteresis loop at high field to a line, extrapolating back to zero volts, and then defining the spontaneous polarization as value of the y-intercept of the extrapolated line, as shown in Figure 5.5. This approach is only useful when there are negligible amounts of leakage current in the measurement. If the sample is leaky, the traditional calculations of remnant polarization and spontaneous polarization will greatly vary with pulse frequency and will not be meaningful. Additionally the calculated values of spontaneous polarization will vary based on the points on the graph chosen for the fit.

To try to better quantify the unstable polarization without including artifacts, first it is necessary to understand its impact on measurements. In a switching measurement, unstable polarization causes a change in the screening charge when the polarization changes orientation, resulting in a small current spike as the voltage approaches 0 volts, as can be seen in graph of measured current against applied voltage in Figure 5.6. In this figure, the black lines

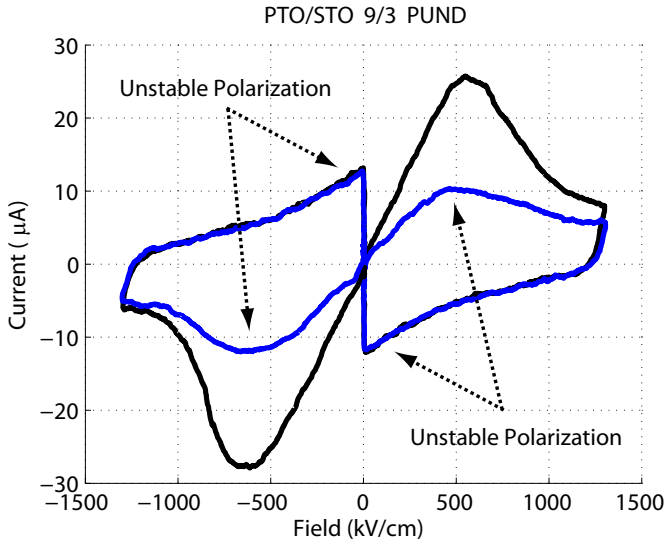

Figure 5.6: In a PUND measurement, unstable polarization is observed in two locations in a plot of measured current vs applied field, for each of positive and negative applied fields. Black lines indicate "P" and "N" pulses, while blue lines indicate "U" and "D" pulses.

are produced from the "P" and "N" pulses of PUND while the blue lines are produced from the "U" and "D" pulses in PUND. Since some amount of polarization is changing orientation while ramping down towards 0 volts, this polarization is then realigned with the field as the field is ramped up in the same direction as the overall polarization state. This affects the screening charge, producing a small peak seen in the blue lines at the coercive field with a magnitude that is greater than current produced from the dielectric charging current. Furthermore, one would not expect a peak in capacitance here, and thus dielectric charging current, for a ferroelectric sample with no unstable polarization. As shown in the next section on dielectric constant measurements, an ideal ferroelectric has a capacitance that decreases almost linearly as field is increased in the same direction as the present polarization state. So these peaks labeled as unstable polarization are the result of changing polarization orientations, rather than other effects. Unstable polarization causes the hysteresis loops measurement to show switching over a large voltage range as can be seen in a traditional polarization measurement shown in Figure 5.5.

For samples with significant unstable polarization, a new approach can be used to attempt to compute the total polarization switched upon reversal of an applied field that additionally separates current due to leakage and dielectric charging, by modifying the PUND pulse sequence. As in a traditional switch-

ing measurement, the voltage is continuously ramped from high positive field to high negative field, and vice versa, while measuring the current response from all sources. However, if in between these applied fields, the voltage is ramped down not to 0 volts, but instead just before the unstable polarization begins switching, then back up to high field, we obtain a direct measurement of dielectric charging and leakage in the high field regimes, similar to the "U" and "D" parts of PUND, but without affecting the unstable polarization. Then the applied field in time would look similar to Figure 5.7. In this figure, the green line measures the switching currents from high negative field to high positive field, the blue line measures switching currents from high positive field to high negative field, and the red ramping lines measures the non-switching currents in the high field regimes. Due to the unstable polarization, it becomes impossible to directly measure the non-switching current in the low field regime with this type of measurement, since some amount of polarization is always switching orientation, contributing to a switching current. However, given the diode-like behavior of ferroelectrics, leakage should be negligible in this low field regime. This assumption is verified by applying a slowly changing DC bias to the sample and measuring the current response, and showing this leakage current is negligible compared to the measured switching currents. Thus, in the low field regime, the non-switching current is due almost entirely to dielectric charging currents. Measurements of dielectric constant, explained in the next section, actually measure capacitance as a function of bias voltage in the low field regime and mostly ignore the effects of switching current since the measurement applies a small, 10 mV AC voltage. Therefore, we can approximately calculate the dielectric charging current expected in a polarization switching measurement by using the measured capacitance as a function of voltage and using the known voltage ramp rate of the polarization measurement with Equation 5.3. Additionally, the correct part of the capacitance versus field loop should be chosen to match the direction of the changing field in the polarization measurement. This is only an approximation of the dielectric charging current, since the capacitance versus field measurement is performed on much slower time scales than the polarization switching measurement. When this method is applied however, we typically see a matching of the calculated dielectric charging current with the measured dielectric charging current plus leakage in the high field, stable polarization regime. It is especially important to take these non-switching currents into consideration when comparing samples of similar polarizations.

All the polarization measurements described here are performed using a Tektronix AFG 3011 arbitrary function generator, a Tektronix DPO 3034 Digital Phosphor Oscilloscope, and a home-built current-to-voltage amplifier cir-

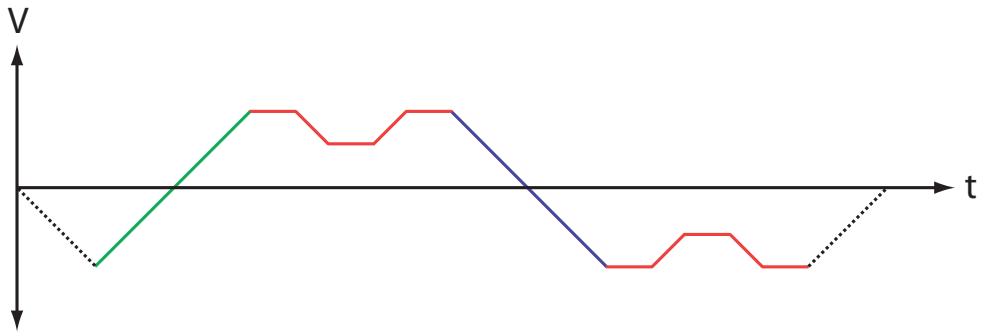

Figure 5.7: A modified PUND pulse sequence. The green line measures the switching current as the applied field is ramping from high negative field to high positive field, the blue line measures switching current from high positive to high negative field, and the red ramping lines measure non-switching sources of current such as dielectric charging and leakage in the high field regimes.

cuit, all shown in Figure 5.8. A Labview program was developed to configure and control both the function generator and the oscilloscope, read data from the oscilloscope, and finally perform calculations on the measurement data. The PUND or modified PUND voltage pulses are created using the arbitrary function generator and the output signal is split, with one part measured on the oscilloscope and the other part connecting to a top electrode on the sample. The current response of the ferroelectric is measured from the bottom electrode, and is amplified by a current-to-voltage converter op amp circuit, where the current is converted into voltage by the equation

$$V_{out} = I_{in}R \tag{5.5}$$

where R is a selectable feedback resistor in the circuit, with selectable values of 15, 98, 1001, 9890 ohms. The output voltage from the amplifier is then measured by another channel of the oscilloscope simultaneously with the applied voltage signal. The Labview software program converts the voltage response values back into current, based on the feedback resistor used in the circuit, and calculates the measured charge and polarization from different parts of the PUND pulse train. The shape and duration of all parts of the PUND pulse are customizable through the Labview program as shown in the bottom of Figure 5.8.

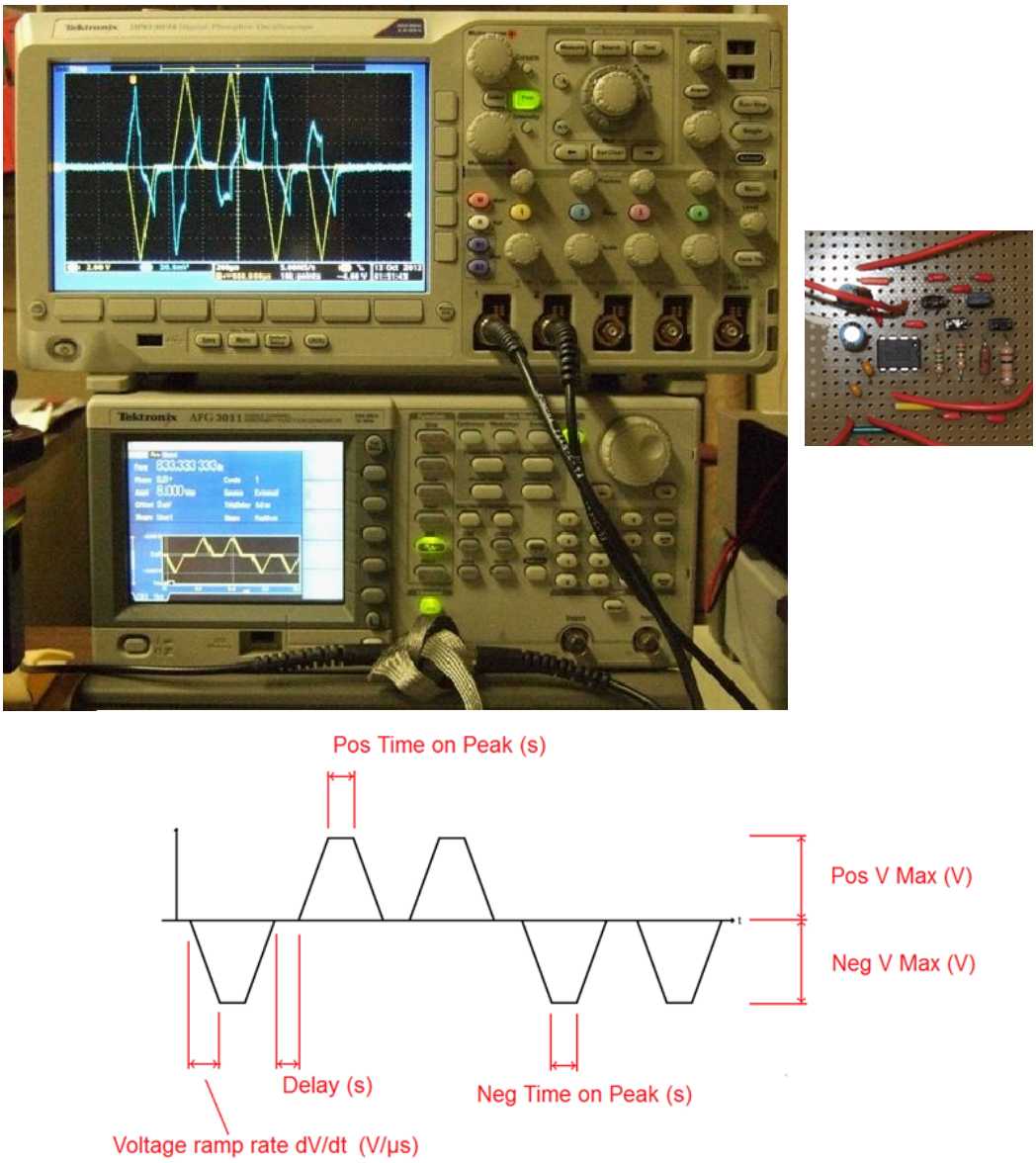

Figure 5.8: Electronic hardware used to measure ferroelectric polarization including the oscilloscope and the arbitrary function generator (top left) and the home built current-to-voltage op amp circuit (right), and the fully customizable PUND pulses that are applied by the Labview program (bottom).

5.2 Dielectric Constant

The dielectric constant of ferroelectrics exhibits a hysteretic behavior as a function of applied field. The dielectric constant, ϵ_r of grown films and superlattices can be calculated by approximating the electrodes and sample as a parallel plate capacitor and then using an LCR meter to measure the capacitance and dissipation factor. Then for a parallel plate capacitor

$$\epsilon_r = \frac{Cd}{A\epsilon_o} \tag{5.6}$$

where C is capacitance, A is the electrode area, and d is the distance between electrodes, equal to the thickness of the superlattice or film, and $\epsilon_o = 8.854 \times 10^{-12}$ F/m is the permittivity of free space.

An LCR meter can measure the capacitance and dissipation factor of a region of ferroelectric between electrodes by applying a small AC voltage to one electrode of the sample and simultaneously measuring the current response from the other electrode. In general, the current response will be of a different phase than the applied voltage, and will lag or lead the applied voltage signal depending on whether a measured circuit element is capacitive or inductive, respectively. The current response of a pure capacitor will lag the applied voltage in phase by 90° while a pure inductor will lead the applied voltage in phase by 90°. The current response will also scale in magnitude, depending on the equivalent impedance of the circuit. These variables are quantified in impedance analysis, with the complex impedance given by $Z = |Z|e^{i\theta} = R + iX$, where $\theta = \tan^{-1}(X/R)$ is the phase difference between the applied voltage and measured response, and $|Z|$ is calculated from the difference in magnitudes of voltage and current signals from Ohm's law for impedance, $V = I|Z|$. When measuring two components in parallel, it is easier to perform analysis in terms of admittance, $Y = 1/Z = |Y|e^{-i\theta} = G + iB$, where G is the conductance and B is the susceptance.

In order to compute the capacitance, it is necessary to choose a model for the circuit, which will then affect the equations used to compute the capacitance and dissipation factor. The ferroelectric here should act as a resistor and capacitor in parallel, with a small amount of additional resistance in series with the ferroelectric, due to the wires, the probe needles, and electrodes. Since the in-series resistance is very small when good, conducting electrodes are used, the circuit can be approximated as just a resistor and capacitor in parallel. The LCR meter then measures in Cp-D mode, where the model circuit is assumed to be a parallel RC circuit, and uses the associated admittance equations to calculate the capacitance and the dissipation factor, also known

as $\tan\delta$ [74]. For a ferroelectric then modeled as an RC parallel circuit, the dissipation factor D is given by the equation

$$D = \tan\delta = \frac{1}{2\pi f C_p R_p} \tag{5.7}$$

where f is the frequency of the applied voltage signal, C_p is the capacitance for the ferroelectric, and R_p is the resistance of the ferroelectric.

In order to measure the dielectric constant of a ferroelectric and dependency on field, the capacitance and dissipation factor is measured as a function of bias voltage using an Agilent E4980A LCR meter. The AC voltage measurement signal is given a DC bias, which is ramped to high positive and negative voltages in time, as shown in Figure 5.9, (Top). During the process of changing the

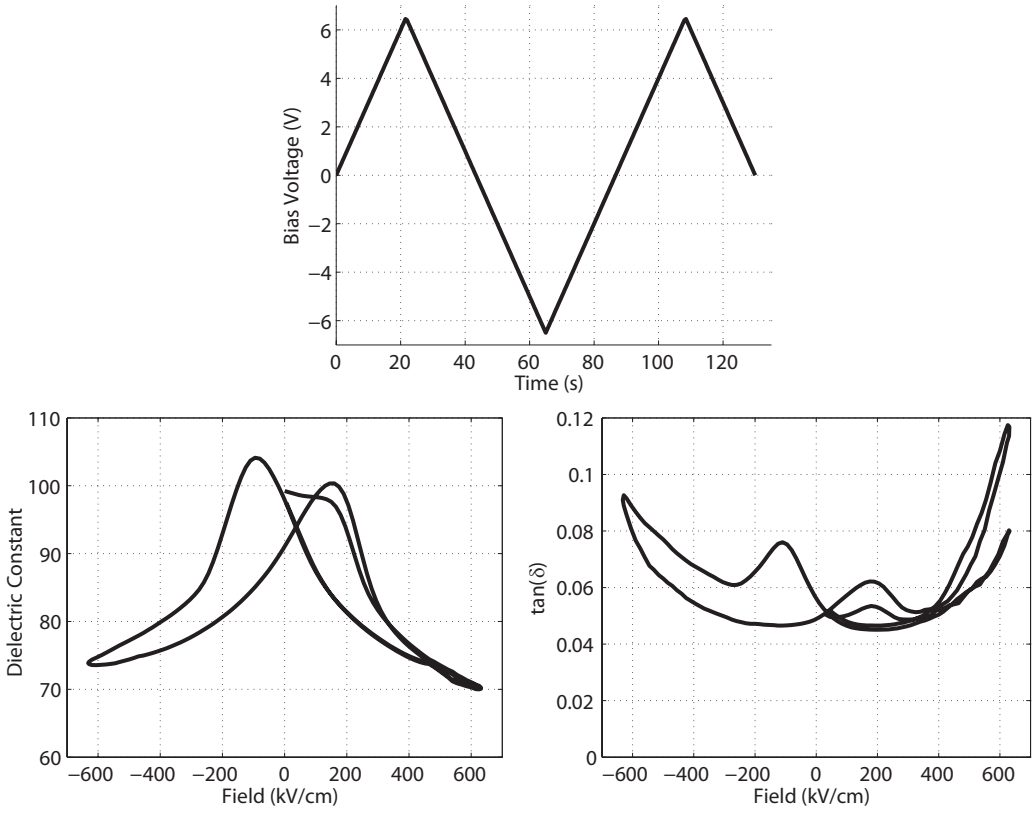

Figure 5.9: (Top) The bias voltage applied by the LCR meter in time. (Bottom Left) The dielectric constant calculated from the measured capacitance at 10 kHz frequency as a function of bias voltage. (Bottom Right) The dissipation factor measured as a function of bias voltage.

bias voltage, controlled by a Labview program, the capacitance and dissipation factor is measured, and the capacitance is used to calculate the dielectric constant, using Equation 5.6. The result for a 6/6 PTO/BTO superlattice yields the two graphs at the bottom of Figure 5.9 and was performed using a measurement peak to peak voltage of 10 mV and a frequency of 10 kHz. As the bias voltage is ramped towards the coercive field, the dielectric constant becomes larger. This is due to the changing energy landscapes surrounding the current polarization state. If the two polarization states have their energy states modeled as a double well potential, then as the bias voltage approaches the coercive field, the energy well becomes shallower, contributing to a larger dielectric constant. At the same time, the other possible polarization energy state becomes steeper. When the coercive field is reached, the system switches to the lower energy potential, and dielectric constant drops to a lower value. As the bias field is ramped toward larger fields in the same polarization direction, this energy well becomes steeper and the dielectric constant drops further. In addition to the behavior of the dielectric constant during this measurement, the resistance of the ferroelectric tends to drop rapidly at high fields. This causes the dissipation factor to rapidly increase at high fields. If the resistance becomes too small, as seen when the dissipation factor becomes large, then the measurement of capacitance may begin to show artifacts.

5.3 Impedance Spectroscopy

Calculations of capacitance and hence dielectric constant are performed assuming the entire circuit consisting of the wires, probe needles, needle contact resistance, electrodes, and the ferroelectric behavior similar to a resistor and capacitor in parallel, with an additional small in-series resistance. This model can be tested by performing impedance spectroscopy, where the resistance and the reactance of the circuit are measured over many orders of magnitude of measurement frequency. Resistors, capacitors, and inductors each have a frequency response, and additionally, the overall frequency response of the circuit depends on the configuration of these circuit elements. However, impedance spectroscopy cannot uniquely determine the circuit elements and their configurations in a given circuit. Impedance spectroscopy can be used to test whether a given circuit model fits the behavior of the actual circuit. Since solutions are not unique, only realistic circuit models should be used in this type of analysis. The reader is referred to [5] for more complete details describing impedance spectroscopy.

Applying impedance spectroscopy to the ferroelectric measurement circuit generally shows a consistency with the model circuit of a resistor in series with

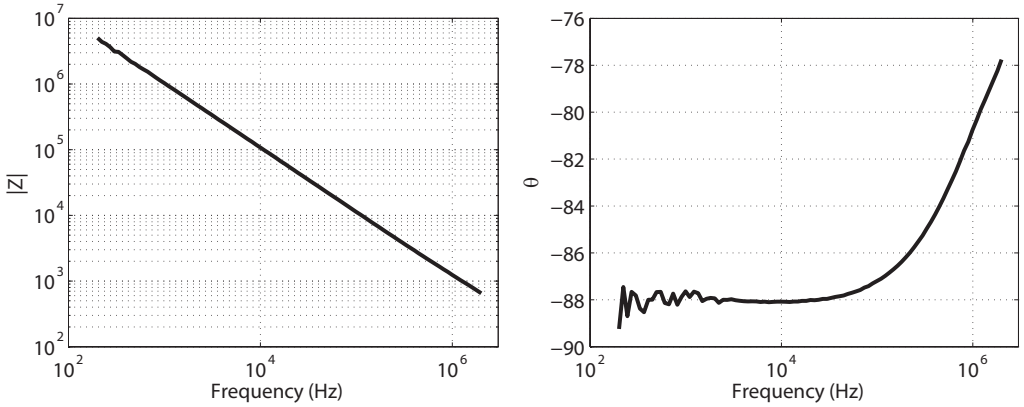

Figure 5.10: The measured frequency response of a 12/3 PTO/CTO superlattice.

a parallel RC circuit and it is possible to estimate the in-series resistance by fitting the frequency response. An impedance spectroscopy measurement of a 12/3 PTO/CTO superlattice is shown in Figure 5.10. There are many ways to transform the data and plot different values against one another. The software package Z-View is used to perform analysis on these types of measurements. If this measurement is fitted to the previously described model, the in-series resistance is found to be about 180 Ohms, the frequency independent value of capacitance is 145 pF, and the resistance of the ferroelectric is greater than 3E7 Ohms. In general, the magnitude of different circuit elements change the shapes of these graphs: the capacitance is related to the slope of the line of $|Z|$, a larger in-series resistance would cause the value of θ to begin changing shape at a lower frequency, and if the resistance of the ferroelectric was much less, the graph of $|Z|$ would be very flat at low frequencies. For leaky electrodes where the measured capacitance of the entire circuit is much more frequency dependent, a plot of Z'' is made against Z', which resembles a semicircle, where the radius is related to the resistance of the ferroelectric. The plot of Z'' against Z' is not shown for this sample, since the resistance of the ferroelectric is very large, the plot resembles a straight line, or possibly an arc of a very large semicircle, and so is not useful for analysis.

5.4 Piezoforce Microscopy

As explained in Chapter 2, materials that are ferroelectric are also piezoelectric, meaning that the application of a force on the crystal will cause a voltage difference across the crystal, or in the converse piezoelectric effect,

the application of a voltage across the crystal changes the size of the crystal. Additionally, the piezoresponse is related to the polarization direction in the ferroelectric. A diagram illustrating the piezoelectric behavior of an ideal ferroelectric with out-of-plane polarization is shown in Figure 5.11, in response to an applied out-of-plane field. A voltage applied in the same direction as the polarization direction will increase the height of the surface, described here as δz relative to the zero field surface height. As the field is changed towards the opposite direction as the polarization, the sample now contracts in height. When a large enough field is applied opposite to the polarization direction, at the coercive field, the polarization direction switches, and the field is now again in the same direction as the polarization. If the change in surface height is plotted as a function of applied field, a loop is obtained as shown in the lower left graph, with arrows indicating the path of the loop in response to the ramping voltage. If the change in surface height is divided by the applied field, then one obtains the out-of-plane piezoelectric coefficient d_{33}, and a hysteresis loop as shown in the bottom right graph.

The piezoelectric effect can be measured with an atomic force microscope that has a conducting cantilever tip connected to a voltage source and lock-in amplifier. However, due to various experimental challenges with a DC measurement, such as low signal to noise, it may not be possible to directly obtain the ideal loops shown in Figure 5.11. Instead another technique can be used to produce hysteresis loops known as switching spectroscopy piezoforce microscopy (SS-PFM) [35, 39], which is also sensitive to the local polarization state below the tip. In this technique, the conducting tip is placed in direct contact with the sample surface, and the piezoresponse is measured with an AC field on top of a changing DC bias. The applied voltage consists of a small AC voltage that measures the piezoresponse while the DC bias voltage is rapidly turned on and off following the top graph of Figure 5.12. This voltage signal is typically applied several times consecutively to check for consistent results.

The SS-PFM measurement may still result in a poor signal to noise if the response is small or the noise is relatively large. In this case, the cantilever and tip may be driven at the contact resonance, greatly increasing the measured response. However, the contact resonance tends not to stay at a single frequency during this type of measurement, but instead may show a small drift. This causes the measured response at a given frequency to fluctuate and show artifacts. A technique was developed by [61] to track the resonance during PFM scans across the sample, and is used to track the resonance during the SS-PFM measurement. On our Asylum AFM, this measurement mode is known as dual AC resonance tracking (DART). Using this mode, the bottom graphs of Figure 5.12 were obtained for a 15/3 PTO/CTO superlattice in response to

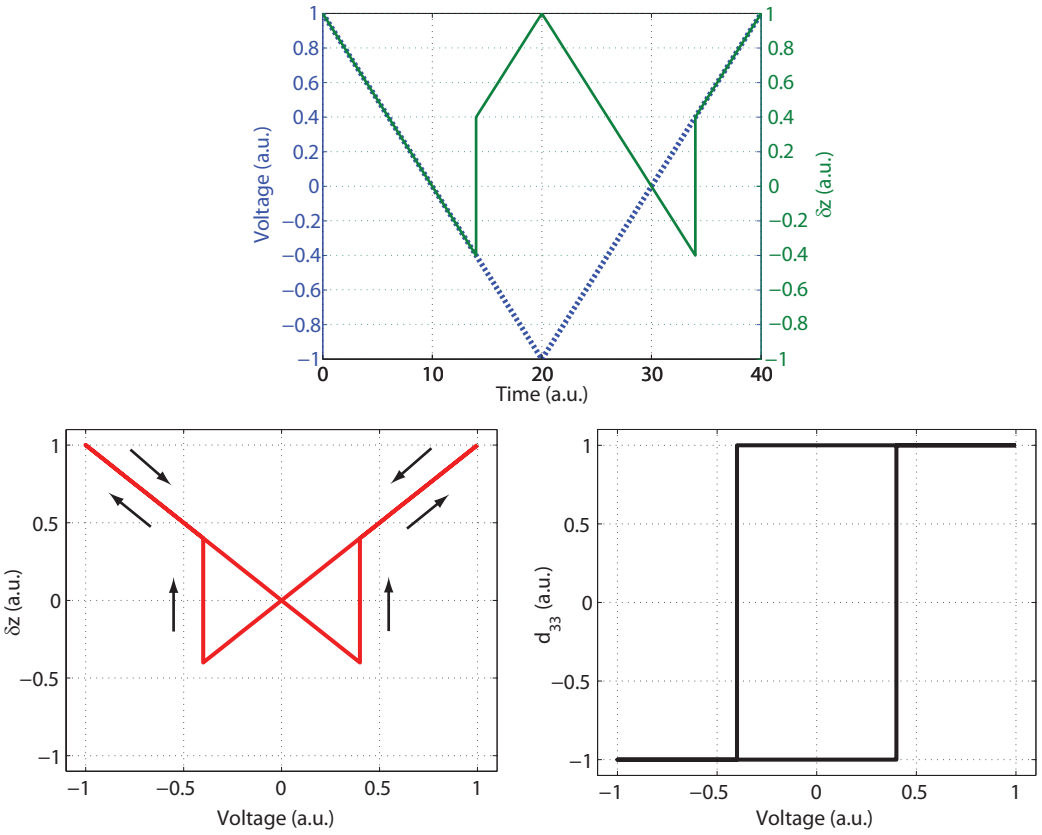

Figure 5.11: The converse piezoelectric response of an ideal ferroelectric with out-of-plane polarization to an applied out-of-plane field. The top graph shows the change in surface height δz in response to an applied voltage. The lower left graph shows a plot of δz versus the applied field. The lower right graph shows the response per applied voltage, or the d_{33} piezoelectric coefficient.

the applied top graph signal of the Figure. The bottom graphs in this figure show measurements of the piezoresponse due to the small AC voltage during the zero voltage plateaus, just after the varying DC bias is applied, for four iterations of the applied voltage shown in the top graph. The hysteresis loops obtained in the bottom left graph show the dependence of the piezoresponse on the local polarization state below the tip. The graph shown in the bottom right graph is a measurement of the phase of the tip, which is related to the polarization direction of the sample. If the polarization is pointed down and a positive voltage is applied, the sample locally contracts, and if the polarization is pointed up and a positive voltage is applied, the sample locally expands. By mapping this behavior to a phase, the two polarization directions result in a 180° phase difference in response to the applied AC voltage. The measured amplitude in the bottom right graph of Figure 5.12 is proportional to the d_{33} piezoelectric coefficient, but scaled up depending on the resonance of the tip

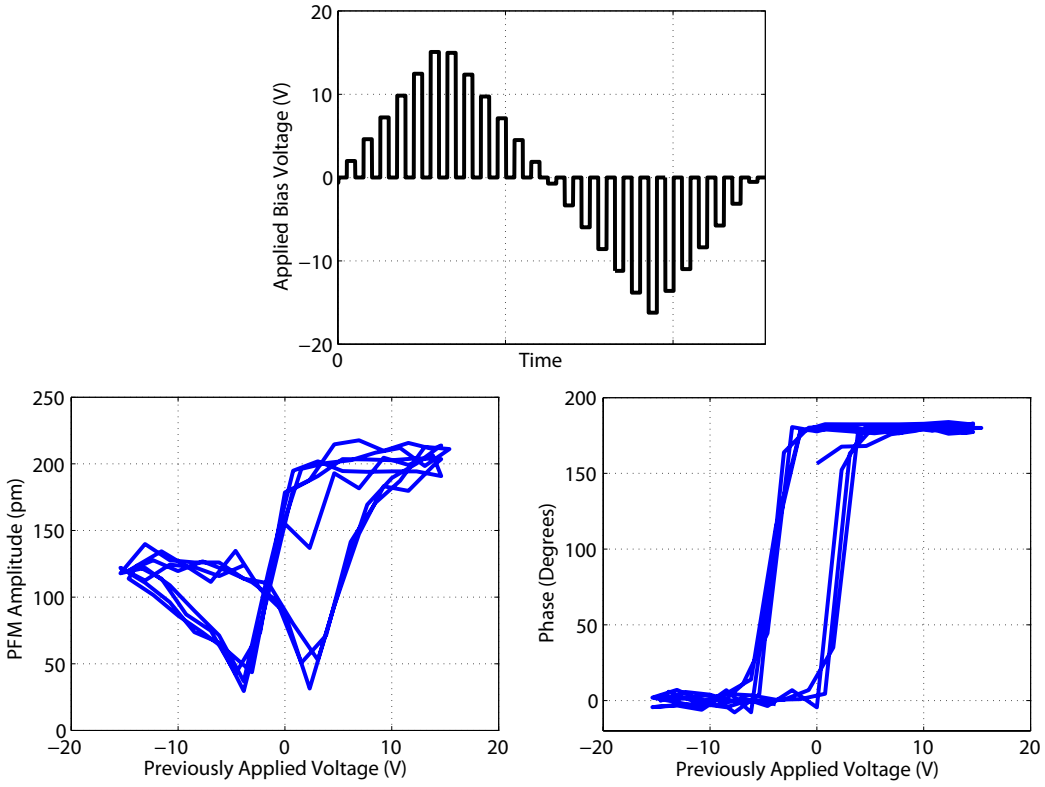

Figure 5.12: A switching spectroscopy PFM measurement on a 15/3 PTO/CTO superlattice. The top graph shows the applied bias signal which is combined with a small AC voltage. The bottom graphs show the amplitude and phase response to AC field on each 0 bias voltage plateau.

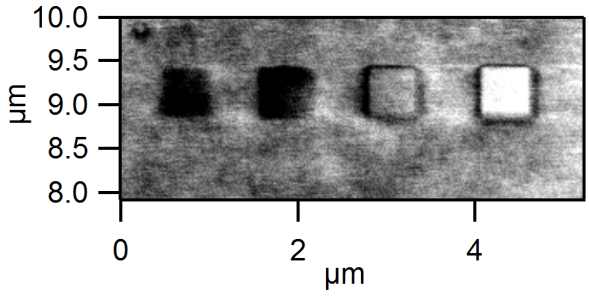

Figure 5.13: A lithography scan showing the piezoresponse of the sample, performed with increasing applied bias voltages squares towards the right side of the image.

and various other parameters, and so it is not possible to directly calculate a value of d_{33} from these plots. However, if the same tip and measurement parameters are used on several samples, the piezoresponse from sample to sample can be quantitatively compared using this measurement technique.

If DC bias voltages are applied to the tip while the AFM is scanning in contact mode, lithography can be performed to qualitatively measure the piezoresponse of the sample. An example of a scan using the lithography feature of the AFM is shown in Figure 5.13 where differing bias voltages are applied to the sample in a pattern of squares. The two left squares are the responses from two different negative bias voltages while the two right squares are responses from two different positive bias voltages. The sample contracts from a negative applied voltage, which is opposite to the current polarization state, resulting in a dark square. When a positive bias voltage is applied, which is the same direction as the polarization, the sample expands, as indicated by the brighter squares. These images are produced using the resonant frequency of the tip and cannot be used to quantitatively determine the piezoelectric coefficient d_{33}, but are useful for measuring the qualitative piezoresponse over an area of the sample.

Chapter 6

$PbTiO_3/CaTiO_3$ Superlattices

In ferroelectric perovskite oxides [17] enhanced piezoelectric responses can occur when the direction of the polarization rotates due to some small change in a parameter, such as an applied electric field or stress. For example, the solid solution lead zirconate titanate, $PbZr_{1-x}Ti_xO_3$ (PZT) has greatly enhanced piezoresponse in a narrow range of composition of about $x = 0.48$ [37]. In epitaxial thin films of ferroelectric materials, strain from the substrate on which they are grown allows for strain engineering, which in some cases leads to stunning results [22, 23, 25].

Here the strain engineering approach is built upon and taken a step further by engineering polarization rotation in artificially layered epitaxial superlattices [71]. In addition to the strain control applied by the substrate, the properties of the structures can be engineered by making use of electrostatic interactions that couple the constituent layers [27, 28] or interactions between different modes at the interfaces between those layers [21]. Based on the expectation that in short period superlattices the polarization should be approximately continuous [27, 52], and that piezoelectric strains should be equally shared [24] from one component layer to the next, it is interesting to consider whether a rotation of the polarization through one or more intermediate phases is achievable by varying the relative thicknesses of the constituent layers of different polarization orientations in the superlattice.

A key factor in the enhanced piezoresponse of PZT is the existence of a monoclinic phase which, as a function of composition, lies between the tetragonal phase and rhombohedral phase of this solid solution [20, 36]. Monoclinic phases have also been found to be crucial to enhanced piezoresponse in other solid solutions, such as $Pb(Zn_{1/3}Nb_{2/3})O_3$-$PbTiO_3$ (PZN-PT) [53] and $Pb(Mg_{1/3}Nb_{2/3})O_3$-$PbTiO_3$ (PMN-PT) [54]. First principles calculations [31], extensions to the phenomenological theory of ferroelectrics [79] and model Hamiltonian approaches [6], have revealed that the monoclinic phases allow

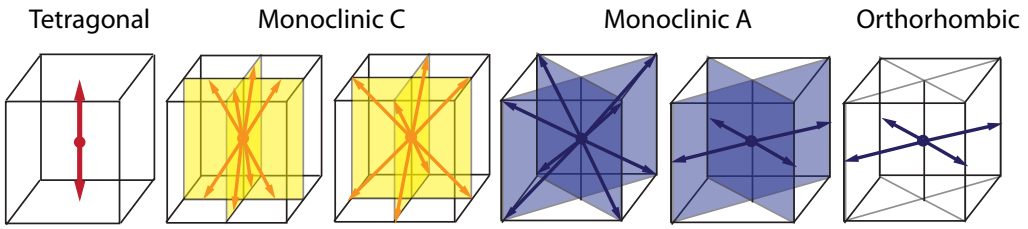

Figure 6.1: Different structural phases constrain the possible directions of polarization, indicated by the arrows, in the pseudocubic crystal. Polarization is constrained to the planes shown for monoclinic A and monoclinic C phases and so the polarization direction may lie at different orientations in these planes.

pathways for the polarization to rotate and that this is the origin of the enhanced piezoresponse in these materials. Three different kinds of monoclinic phases are possible, M_C in which the polarization is directed along $[u0v]$, and M_A and M_B in which polarization is along $[uuv]$ with $u < v$ for M_A and $u > v$ for M_B. These possible polarization directions are illustrated in Figure 6.1 for some of these structural phases. The phase observed in PZT is the M_A phase, while that in PZN-PT and PMN-PT is the M_C phase [53, 54]. A more recent study has shown that as increasingly large pressure is applied to pure $PbTiO_3$, the crystal undergoes consecutive transitions from $T - M_C - M_A - R$ [26] (where R is rhombohedral phase with polarization along [111]).

Due to the compressive strain of -1.64% that $SrTiO_3$ exerts on $PbTiO_3$, $PbTiO_3$ epitaxially constrained in-plane to the lattice parameter of a $SrTiO_3$ substrate is tetragonal and has polarization directed along the [001] direction. By contrast $CaTiO_3$ on $SrTiO_3$ is under 2% tensile strain. Based on first-principles calculations it is expected that the ground state of $CaTiO_3$ under sufficient tensile strain ($> 1.5\%$) is orthorhombic (O) and ferroelectric with polarization directed along [110] directions with respect to the cubic perovskite substrate [18]. $PbTiO_3$ itself can develop in-plane polarization when grown on $DyScO_3$ [11], which exerts a tensile strain of around 1.4%. Additionally, recent first principles predictions for the related superlattice system $PbTiO_3/SrTiO_3$ suggest it could have a continuous rotation of polarization from [001] to [110] as the strain is varied from compressive to tensile [2].

In this study, rather than modify strain, which is experimentally limited to certain discrete values by the choice of available substrates, superlattice samples were prepared in which the constituent layers have different relative thicknesses. The aim of this study was to determine whether, for particular ratios of the constituent layer thicknesses, the competing tendencies of $PbTiO_3$

and $CaTiO_3$ would result in the overall direction of polarization being directed along one of the intermediate monoclinic directions associated with polarization rotation. In this study the $CaTiO_3$ layer thickness was fixed at 3 unit cells and all of the superlattices were epitaxially constrained in-plane to the $SrTiO_3$ substrate, both conditions which should encourage uniform polarization from layer to layer. The degree to which adjoining layers are coupled is open to question [1, 40, 77, 86], but not considered in detail here.

6.1 Growth and Structural Characterization

PTO/CTO superlattices were deposited using off-axis RF magnetron sputtering as described in Chapter 3. In almost all of the superlattices discussed here, the $CaTiO_3$ layer thickness was 3 unit cells and the $PbTiO_3$ thickness was varied from sample to sample. Here changes in properties are considered as a function of the $CaTiO_3$ volume fraction

$$x = \frac{n_{CaTiO_3}}{n_{CaTiO_3} + n_{PbTiO_3}} \tag{6.1}$$

where n_{CaTiO_3} and n_{PbTiO_3} are the number of unit cells of each material in the superlattice bilayer. Most of the samples discussed here also had bottom $SrRuO_3$ electrodes of 20 nm thickness deposited in-situ. Gold top electrodes were added to the samples post-deposition. For $x \leq 0.5$ the total thickness of each superlattice was approximately 100 nm. For superlattices with $x > 0.5$ the epitaxial constraint from the substrate could only be maintained by reducing the total thickness of the superlattice, but as this led to high leakage currents we do not show electrical measurements for these samples. High Resolution-Scanning Transmission Electron Microscopy (HR-STEM) and x-ray diffraction both reveal that the samples are grown epitaxially constrained to the in-plane lattice parameter of the substrate, that the layers in the structure are well defined with no evidence of grain boundaries or misfit dislocations. An example of a TEM image is shown in Figure 4.8, with brighter layers corresponding to $PbTiO_3$ and darker layers corresponding to $CaTiO_3$.

The average tetragonality of each superlattice sample was measured using x-ray diffraction as described in Chapter 4. An example diffraction scan of an 8/3 PTO/CTO superlattice is shown in Figure 6.2 that is typical of the superlattices grown. The tetragonality was obtained from the (001) and (002) peaks of the superlattice using simulations which took in to account the underlying $SrRuO_3$ electrode. Values were confirmed by measurements of the position of the (113) peak, a peak for which $SrRuO_3$ has little or no intensity. Samples of the same composition, both with and without bottom electrodes,

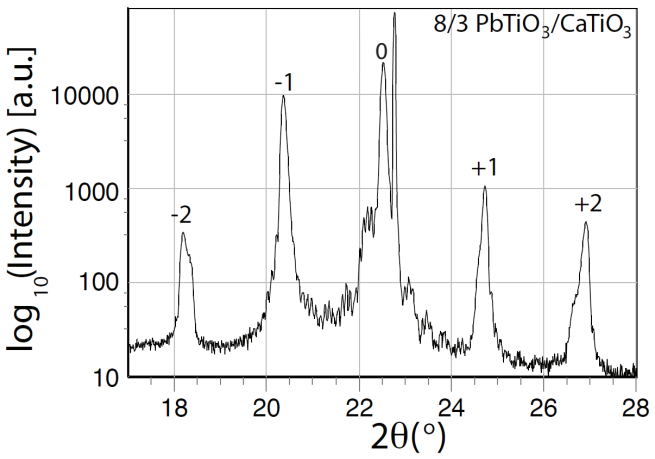

Figure 6.2: An example x-ray diffraction scan of an 8/3 PTO/CTO superlattice around the (001) diffraction peak of the $SrTiO_3$ substrate. The substrate is the most intense peak, while the main superlattice peak is labeled as 0. Superlattice satellite peaks are labeled ± 1 and ± 2.

were found to have the same tetragonality. The tetragonality of the samples is plotted as function of the $CaTiO_3$ volume fraction, x, in Fig. 6.3. The error bars are plotted in this graph, but are smaller than the size of the marker for almost every point. The background colors shown on the graph correspond to the structural phases in Figure 6.1, with phases changing from left to right as tetragonal, M_C, M_A, and orthorhombic. These phases and boundaries of different phases are determined by other x-ray diffraction measurements, as will be shown later. The shape of the curve itself has a noticeable similarity with that obtained for pure $PbTiO_3$ as a function of pressure, shown in Fig. 3 of Ahart et al. [26]. The changes in slope of the tetragonality match with the changes in structural phases.

Confirmation that the changes in slope of the tetragonality vs $CaTiO_3$ volume fraction are associated with changes of symmetry is provided by high resolution x-ray diffraction reciprocal space maps around the (113) and (103) superlattice peaks, which show different kinds of splitting for M_C, M_A, R and O phases [12, 81]. For monoclinic distortions, the film diffraction peak has a small scale splitting into two or three peaks, depending on the particular reciprocal space map geometry. For monoclinic C distortions, one expects splitting into two diffraction peaks in an (hhl) map and splitting into three peaks in an (h0l) map. In the (hhl) map, the two peaks should have slightly larger and smaller values of l, while in an (h0l) map, the splitting is similar,

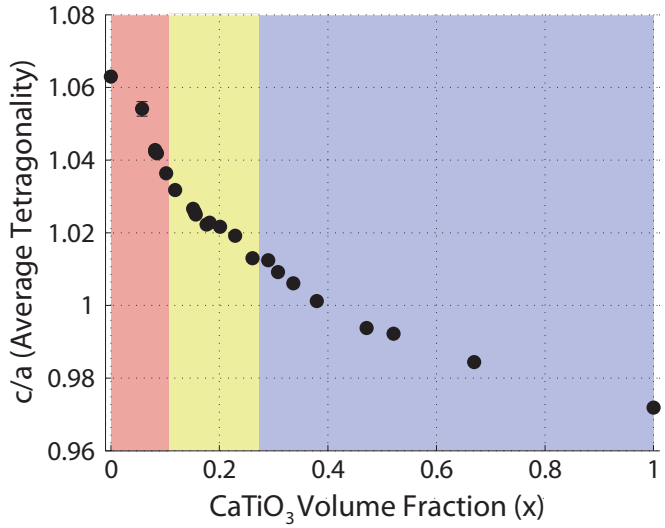

Figure 6.3: Measurement of the average tetragonality of PTO/CTO superlattices as a function of $CaTiO_3$ volume fraction.

but the 3rd peak has a different value of h than the other two peaks. The monoclinic A distortion is similar to the monoclinic C, but with a 45 degree rotation, and so here the splitting into three peaks should be seen in an (hhl) map, while splitting into two peaks should be seen in an (h0l) map.

The results on our samples shown in Figure 6.4 show splitting compatible with a monoclinic distortion along $[u0v]$ (M_C) for samples with $0.13 < x < 0.26$. For samples with higher $CaTiO_3$ volume fraction there appears to be a smooth transition through a M_A phase with polarization along $[uuv]$ towards an orthorhombic structure distorted along [110]. The 24/3 superlattice shows no splitting in the (113) or (103) planes. Moving to higher volume fractions, the 18/3 now shows a very clear splitting into two peaks in the (113) map, and three peaks for the (103) map, with the third peak at a larger value of h, consistent with the monoclinic C phase. The 9/3 shows a similar behavior to the 18/3, but now the splitting in the (113) map is less, and the third peak in the (103) map is distorted towards a smaller h instead of a larger h. The 5/3 superlattice shows very different behavior with diffuse scattering seen in the (113) map and weak splitting in both maps. These features are consistent with monoclinic A rotating towards orthorhombic. Finally the 3/3 shows even stronger diffuse scattering in the (113) map, with no diffuse scattering now towards larger l value, indicating the polarization direction has rotated further into the plane. It is difficult to determine if this phase is orthorhombic or has a slight distortion consistent with monoclinic A.

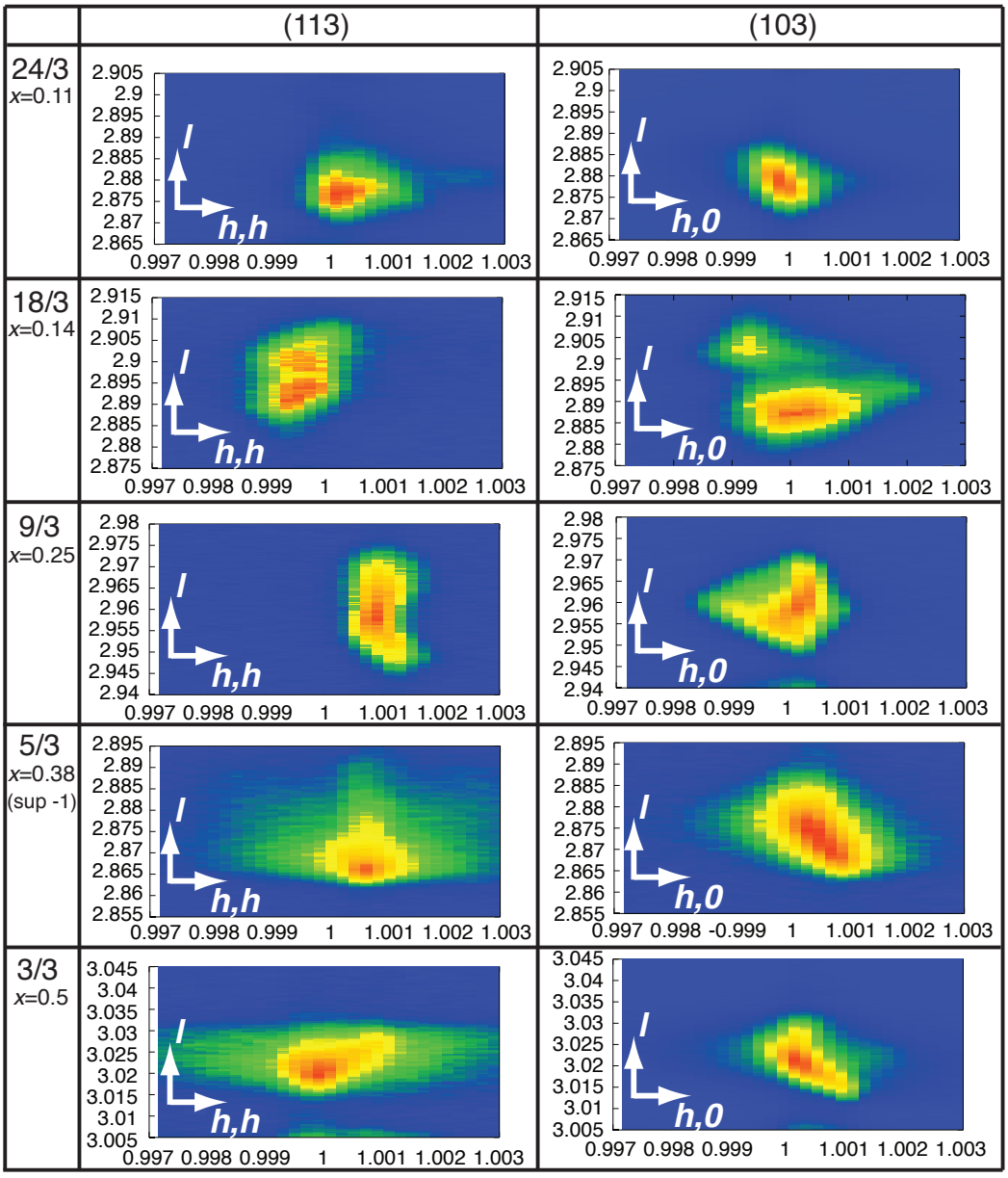

Figure 6.4: X-ray diffraction reciprocal space maps around the (113) and (103) peaks of 5 $PbTiO_3/CaTiO_3$ superlattice samples. The x and y axes are labeled with respect to the $SrTiO_3$ lattice. Intensity is plotted on a linear color scale with intensity represented from low to high by: blue-green-yellow-red.). Note that as the main superlattice peaks of the 5/3 sample lie directly on top of the much more intense $SrTiO_3$ substrate peak the scan shown is on the -1 superlattice satellite peak. It was verified on other samples that superlattice satellite peaks show the same kind of splitting as the main superlattice peaks. The measurements shown here were performed on a Bruker D8 Discover diffractometer.

In addition to the scans shown in Figure 6.4, lower resolution scans were made over a broader range of reciprocal space for all samples, with some maps shown in Figure 6.5. The x and y axes are labeled with respect to the $SrTiO_3$ lattice and the color scale corresponds to ln(Intensity). Both Figures 6.4 and 6.5 confirm that all samples had in-plane lattice parameters constrained to the $SrTiO_3$ substrate lattice parameter. Samples with $CaTiO_3$ volume fractions $x < 0.25$ show evidence of domain structure in Figure 6.5 that decreases in periodicity with increasing volume fraction, consistent with polarization rotating into the plane. All the samples with volume fractions $x < 0.26$ show satellite peaks around (113) indicative of domains, which appear to gradually decrease in size as the $CaTiO_3$ volume fraction is increased. Satellite peaks around (113) can occur for domains which are either entirely in-plane, entirely out-of-plane, or somewhere in between.

To further confirm that an in-plane polarization developed in the films, grazing incidence x-ray diffraction in-plane was performed around ($hk0$) substrate peaks [11, 30]. If scattering from domains is seen around these peaks it shows that there is an in-plane component of the polarization, since these maps have no out of plane component. Grazing incidence in-plane x-ray diffraction was performed at beamlines X22C and X21 at the National Synchrotron Light Source at Brookhaven National Laboratory. The x-ray radiation used in the synchrotron measurements had energy 10 keV. In addition to the scans around (100) and (110) shown, scans were also made around (010) and (210), and the full set of scans was made on a total of 8 samples. The results shown here were obtained at X21 using a Pilatus area detector to rapidly map out large areas of reciprocal space with high resolution. Comparable results were obtained using a point detector at X22C, but, as those maps have a lower point density due to additional time required to perform the scans, the only maps presented here were obtained at X21. In Figure 6.6 we show reciprocal space maps made around the (100) (top row) and (110) (bottom row) substrate peaks for four samples. No in-plane features are seen for samples with $x < 0.15$. For samples with $0.15 < x < 0.26$ spots appear along (110) directions, and these are replaced by weaker spots along (010) directions for $x > 0.26$. These features are compatible with scattering from domain structures associated with polarizations that have some component of their polarization directed along the direction in which the features are seen. Similar features were observed under applied electric field in PZN-PT by Noheda et al [53]. Here they are observed in the absence of an applied field because the c axis direction is fixed by the epitaxial strain coming from the $SrTiO_3$ substrate. As the $CaTiO_3$ volume fraction is increased, the domain features are seen increasingly far from the central diffraction spot (in agreement with the domain features observed

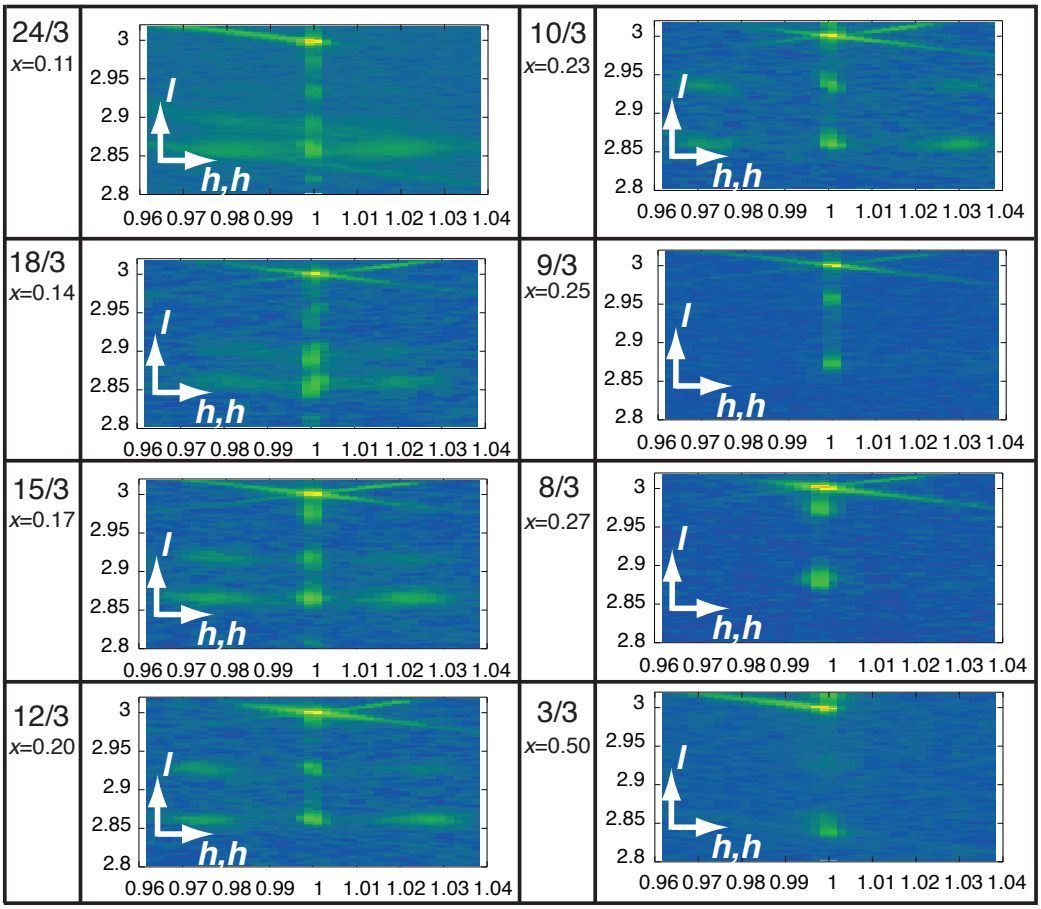

Figure 6.5: X-ray diffraction reciprocal space maps in the vicinity of the (113) $SrTiO_3$ reflection, demonstrating coherent growth and the presence of ferroelectric domain structure for samples with $x < 0.25$. The x-ray measurement shown were performed on a Bruker D8 Discover diffractometer with Cu K-α radiation.

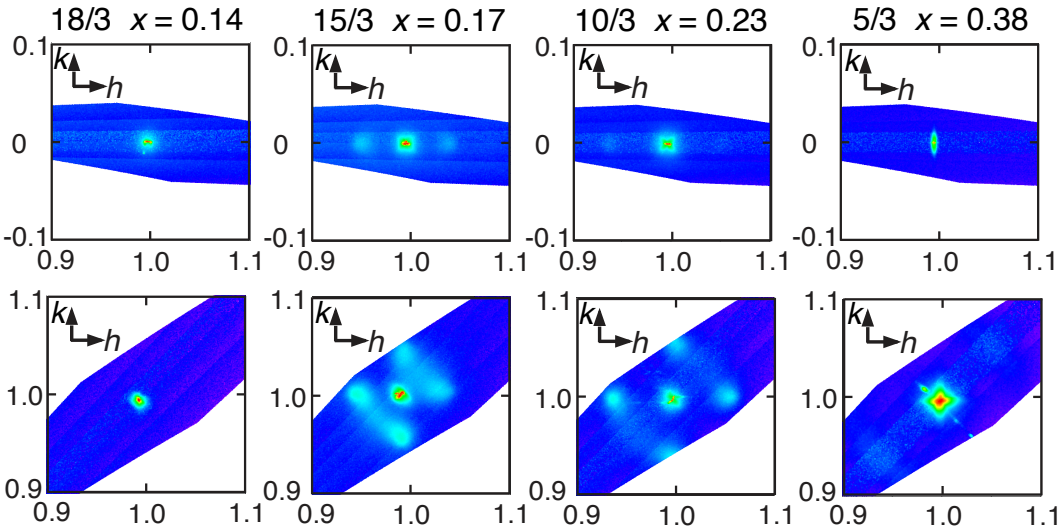

Figure 6.6: Grazing incidence x-ray diffraction reciprocal space maps along in-plane directions around the substrate (100) (top) and (110) (bottom) peaks for from left to right, 18/3, 15/3, 10/3 and 5/3 $PbTiO_3/CaTiO_3$ superlattices. Intensity is plotted on a logarithmic color scale with intensity represented from low to high by: blue-green-yellow-red.)

around (113) peaks); this implies that the in-plane domain spacing becomes smaller as the polarization starts to rotate into the plane. A close inspection of the scans around (100) for the 15/3 and 10/3 samples show that, in addition to the well defined spots far from the central substrate spot, there is "butterfly-like" diffuse scattering in the immediate vicinity of the substrate peaks, which is similar to that observed in PMN-PT [82] and PZN-PT [83]. For the 5/3 sample, in which polarization has rotated to be in the (uuv) plane, these features have also rotated, ie. the "butterfly" is now seen around the (110) peak (and is rotated by 45^o) and the (100) scan now shows ellipsoid diffuse scattering, similar to that normally seen around the (110) peak in rhombohedral PMN-PT [82] and PZN-PT [83], though this scattering is also rotated by 45^o when compared to those materials.

A representation of the general changes in polarization directions as one progressively increases the $CaTiO_3$ volume fraction is shown in Figure 6.1. The observation of a phase with polarization along $[u0v]$ in the samples is particularly interesting. While the transition through two monoclinic phases is seen in pure $PbTiO_3$ under pressure at low temperatures, the solid solutions generally only show one monoclinic phase, and the first principles predictions for polarization rotation in $PbTiO_3/SrTiO_3$ superlattices under increasing tensile

strain [2] pointed towards rotation from [001] to [110], with no intermediate $(u0v)$ phase. There have been a number of studies regarding the phase diagram of the $Pb_{1-x}Ca_xTiO_3$ solid solution, but there is not universal agreement on the phases that exist between the tetragonal structure seen from $0 \leq x < 0.4$ and orthorhombic $CaTiO_3$, with some studies finding a cubic intermediate phase[45], and others pointing towards various lower symmetry phases, none of which has been identified as monoclinic, between the two clearly defined endpoints[32, 65, 76]. In any case, the samples here differ substantially from the solid-solution, both because of their highly ordered structure and the progressive change from highly compressive to highly tensile strain as the $CaTiO_3$ volume fraction is increased. We also note that in the composition range where we identify polarization rotation through a monoclinic phase the solid solution has been clearly identified as tetragonal.

6.2 Functional Properties

Having demonstrated that the structural changes which allow polarization rotation occur in our materials, characterization of their functional properties was performed.

Initially, polarization measurements of the superlattices were measured using the PUND technique, as described in Chapter 5, determining stable polarization values, shown in the hollow squares of Figure 6.7. Polarization measurements were performed on all samples grown with a bottom $SrRuO_3$ electrodes, which were later given top gold electrodes. Measurements were performed using a voltage ramp rate of 1.0, 0.1, and 0.01 V/μs, and polarization values show little dependence on the measurement frequency. For a given electrode, the measured polarization is seen to slightly decrease with slower voltage ramp rates, while simultaneously the non-switching current peaks were observed to increase slightly, showing the time dependence of the unstable polarization present in the samples. However, these differences in polarization values for a given electrode were only about the same magnitude as measured polarization differences between different electrodes, measured at the same measurement frequency. The size of the error bars on the graph represents the measurement differences both between different electrodes and differences in polarization measured at different frequencies.

The switching dynamics show a very complicated behavior, as shown in plots of current response versus applied voltage for six superlattices in Figure 6.8. Arrows on the top left graph indicate the changing applied voltage directions as the PUND sequence is applied. We see changes in the number and magnitude of switching peaks, indicating multiple coercive fields, and the

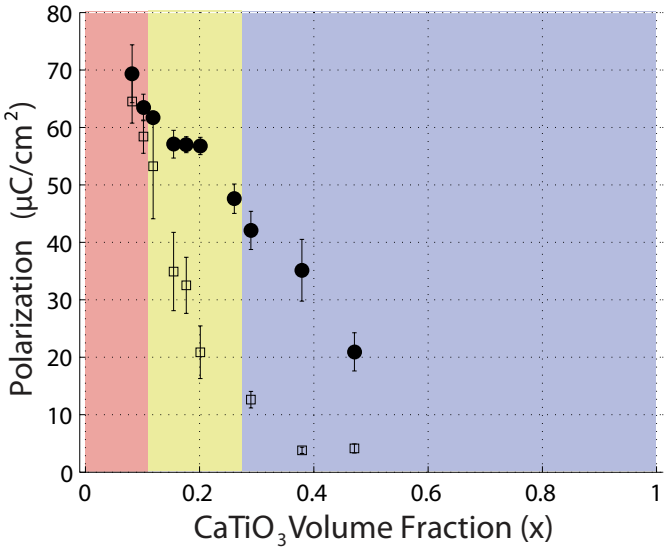

Figure 6.7: Measurement of the Polarization of PTO/CTO superlattices as a function of $CaTiO_3$ volume fraction. The black circles are measurements of the total switched polarization, while the hollow squares are measurements of the stable polarization in a standard PUND measurement.

magnitude and behavior of the unstable polarization changes from sample to sample. The 24/3 and 18/3 superlattices show multiple switching peaks on the positive voltage side and two switching peaks on the negative voltage side. The number of these switching peaks was not observed to change with measurement frequency. The magnitude of the unstable polarization and other non-switching currents, shown as the blue lines, is generally small here, with more unstable polarization on the negative voltage side, as can be seen from the current ramp up as the voltage approaches 0 volts from the negative voltage side. The 15/3 and the 12/3 show much larger magnitudes in unstable polarization. The second switching peak has moved into the positive voltage side, as can be seen by the large peaks of negative current in the bottom halves of these graphs. Additionally, the blue lines show very large current peaks as the applied voltage is ramped up from zero volts, indicating a larger amount of polarization is switching here, even though the voltage is ramped in the same direction as before. The 8/3 shows similar behavior to the 12/3 and 15/3, but now with much less magnitude and less well defined switching peaks. Finally the 3/3 only shows a very broad switching current peak with little magnitude.

The multiple coercive fields observed may be due to the various polarization orientations possible in these samples. The x-ray diffraction measure-

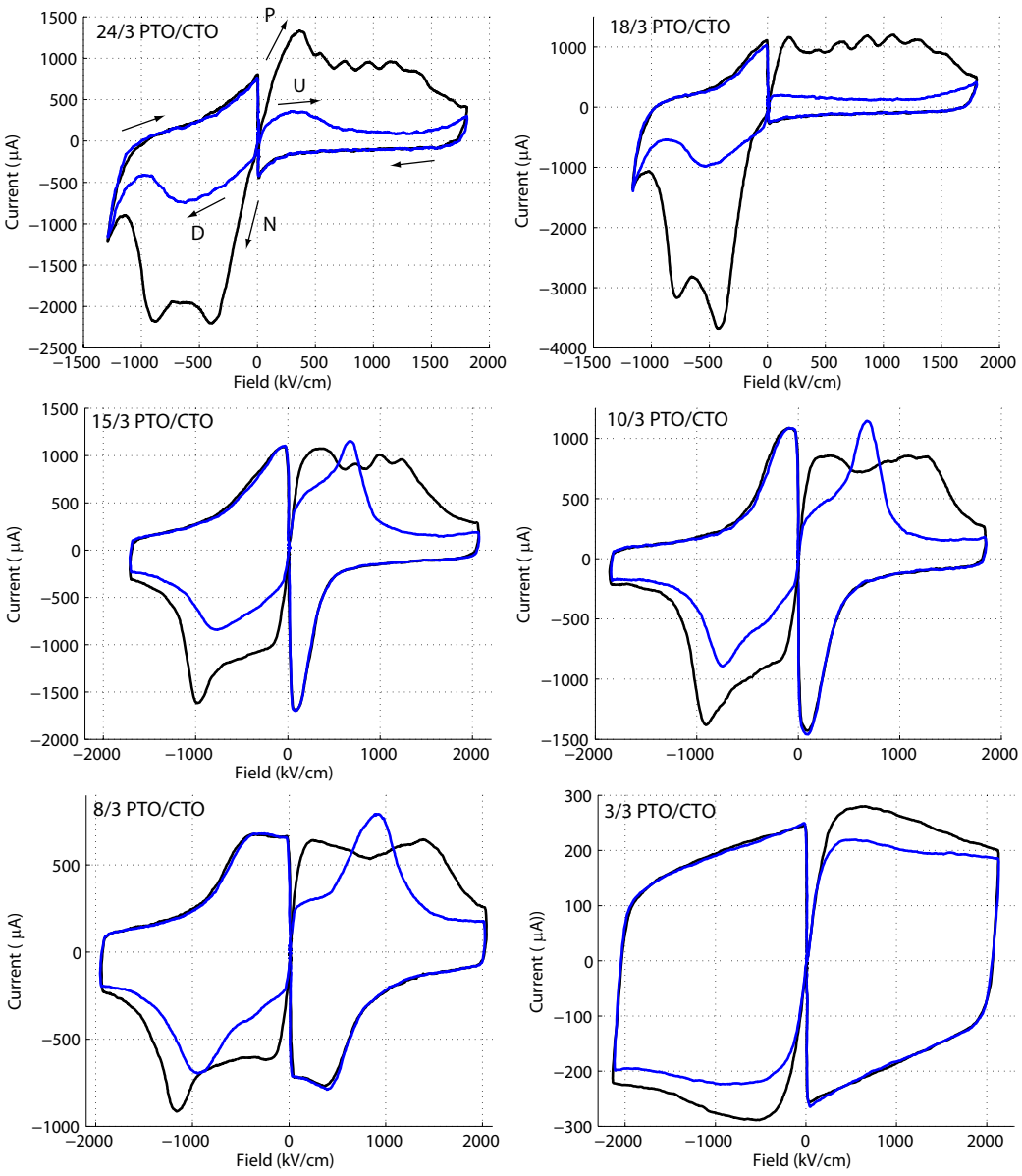

Figure 6.8: Current versus applied voltage plots generated from PUND shows a variety of changing switching behaviors. Black lines are generated from the P and N parts of PUND, while blue lines are generated from U and D parts of PUND. Arrows shows the direction of changing applied voltages and the parts of the PUND pulse.

ments show the polarization direction has some in-plane component for 18/3 superlattices and higher $CaTiO_3$ volume fractions. Since a field is applied in only the out-of-plane direction during polarization measurements, the different polarization orientations may react at different magnitudes of applied fields, or possibly changing polarization orientation in discrete steps. As the $CaTiO_3$ volume fraction increases, x-ray diffraction shows the polarization rotates more towards the in-plane direction. In this case, the polarization measurements show larger coercive fields and more spread out switching current peaks, consistent with more in-plane polarization directions being less affected by out-of-plane fields.

Due to the unstable polarization greatly changing in magnitude from sample to sample and the fact that PUND only measures a stable polarization, a new approach described as the modified PUND measurement in Chapter 5, was used to measure the total switchable polarization for each superlattice. These results are shown as the solid circles in the plot of polarization versus $CaTiO_3$ volume fraction in Figure 6.7. Interestingly, we see the total switched polarization in the monoclinic C phase is not changing in magnitude, even though the polarization domains were observed to increasing in size in the in-plane direction, as seen from the grazing incident x-ray diffraction measurements. Outside of this plateau, the switched polarization magnitude is observed to decrease relatively linearly as $CaTiO_3$ volume increases.

As described in Chapter 5, these measurements were performed by first measuring the total current response when the field is changed continuously from high positive field to high negative field, and vice versa. Then the non-switching current is measured directly in the high field regime by ramping the field down from high field, to just before the unstable polarization switches, and then back to high field again. In the low field regime, the non-switching current is primarily due to dielectric charging, and so is calculated using the measured values of capacitance as a function of field measured using an LCR meter. A few examples of the measurement data produced using this method is shown in Figure 6.9. The green lines are measured responses to voltage being ramped from high negative field to high positive field, the blue lines are measured responses to voltage being ramped from high negative field to high positive field, and the red lines indicate the measured non-switching sources of current where voltage is ramped down only to just before the unstable polarization switches. The orange lines on the current versus voltage graphs are the calculated dielectric charging currents, from $I = C(V)dV/dt$, where the capacitance as a function of bias voltage is measured using an LCR meter and dV/dt is the voltage ramp rate, 1.0 V/μs for these examples. We see a good matching between the orange lines and the red lines, confirming the good

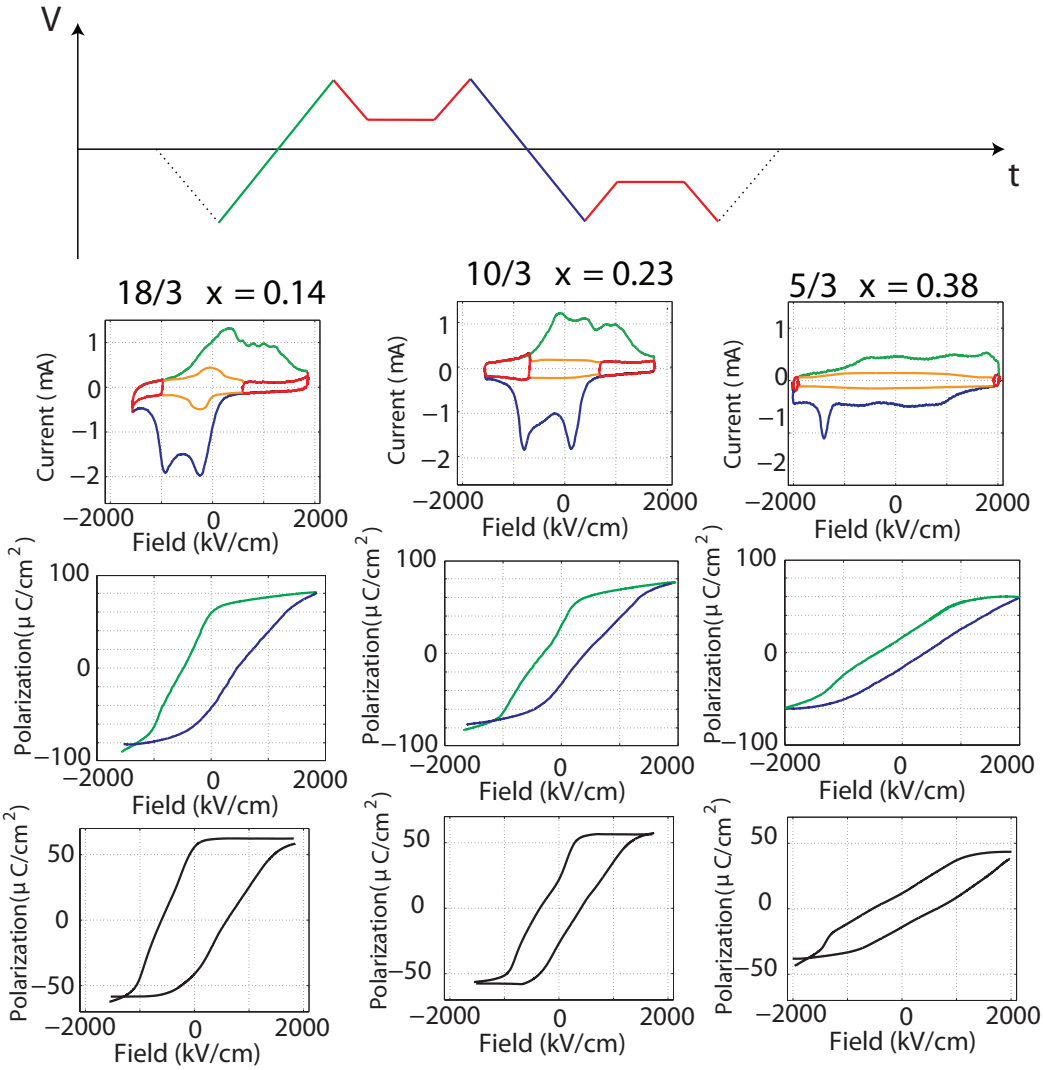

Figure 6.9: The modified PUND technique used to calculate the total switchable polarization.

accuracy of this dielectric charging current approximation. The middle graphs show the hysteresis loops if no subtraction is performed, which over-estimates the true polarization. The bottom graphs show the subtracted polarization, used to calculate the polarization values in Figure 6.7, corresponding to the area between the total switching current and non-switching current curves of the graphs of current versus voltage.

The dielectric constant of each superlattice was measured as a function of DC bias with an LCR meter using the techniques outlined in Chapter 5.2, to produce Figure 6.10. The dielectric constant is calculated using the measured value of capacitance at the crossing point of the loops near zero volts. In a few cases where the loop is not ideal, and there is not a clear crossing point near zero volts, then the average value of the capacitance at zero volts was used as the capacitance value for that electrode. Measurements of the capacitance versus bias voltage were performed at a frequency of 10 kHz and a peak to peak voltage of 10 mV. Values of capacitance were observed to have little dependence on the measurement frequency in the range of 20 Hz to 500 kHz. The capacitance of an electrode and its measured area are used with Equation 5.6 to calculate the dielectric constant. Measurements were performed on at least five electrodes per sample to obtain the error bars shown in the figure.

In Figure 6.10, the dielectric constant is seen to peak at the transition to $[uuv]$ oriented polarization and has a small plateau, before rapidly falling off in the M_C phase, and becoming fairly constant for $x > 0.26$. The relatively

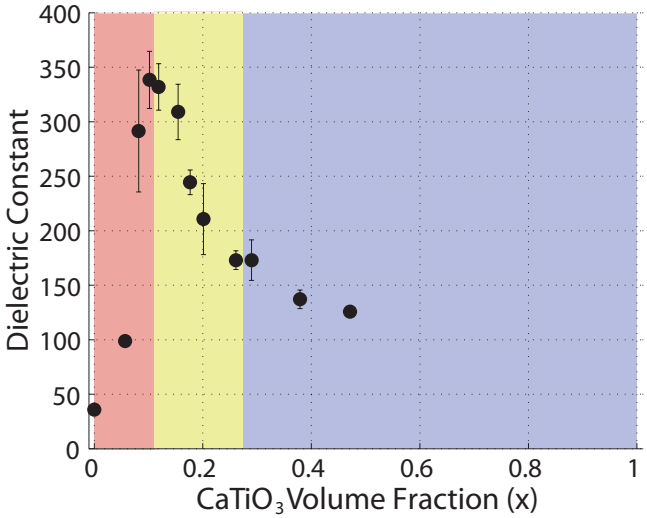

Figure 6.10: Measurement of the dielectric constant of PTO/CTO superlattices as a function of $CaTiO_3$ volume fraction.

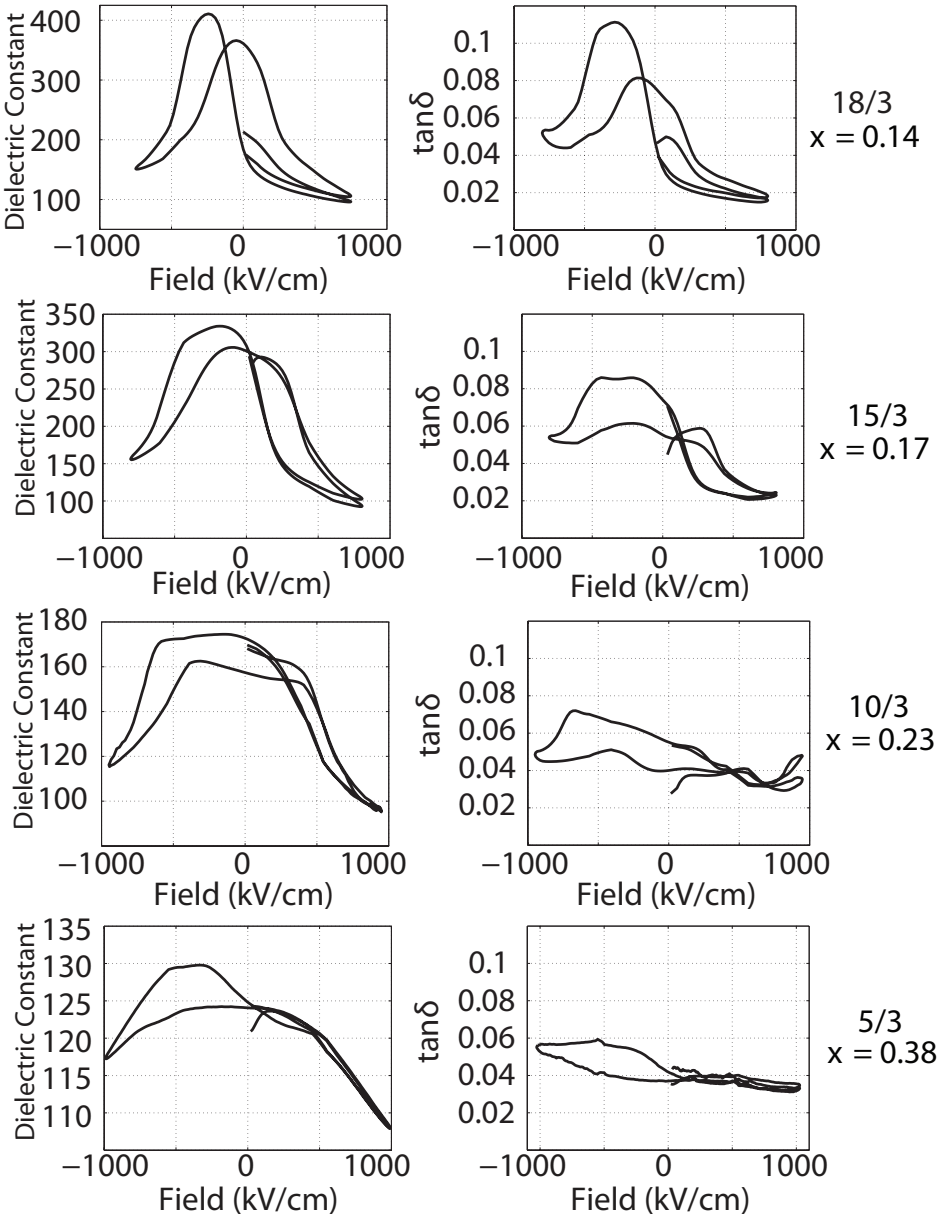

Figure 6.11: Calculated dielectric constant and associated loss tangent measurements for several PTO/CTO superlattices.

constant polarization in the M_C phase combined with the enhanced dielectric constant in the vicinity of the $T - M_C$ transition is a good indication that piezoresponse should be high in these samples. Example measurement loops of the dielectric constant and the associated dissipation factor, or loss tangent, are shown in Figure 6.11. The measured loops near the peak enhancement show large tunabilities, or percentage change in dielectric constant as a function of applied field. At higher $CaTiO_3$ volume fractions, the loops become much flatter, and have less well defined crossings of the loops and coercive fields. This behavior is consistent with the polarization measurements that also showed a broadened and poorly defined coercive field at higher $CaTiO_3$ volume fractions. The asymmetry of the loops here is also likely due to the different electrode materials used for the top and bottom electrodes.

Finally, the out-of-plane strain generated in response to an out-of-plane field (d_{33}) was measured directly using Dual Frequency Resonance Technique-Piezo Force Microscopy (DART-PFM) and Switching Spectrocopy-PiezoForce Microscopy (SS-PFM) [39, 61] on an Asylum MFP-3D atomic force microscope with the results summarized in Figure 6.12. Measurements were performed using a Au coated AFM tip (MikroMasch NSC18/Cr-Au/50) as the top electrode, which was applied directly to the superlattice top layer, not the gold top electrode used for electrical characterization. Due to numerous experimental factors, the absolute magnitude of this piezoresponse is challeng-

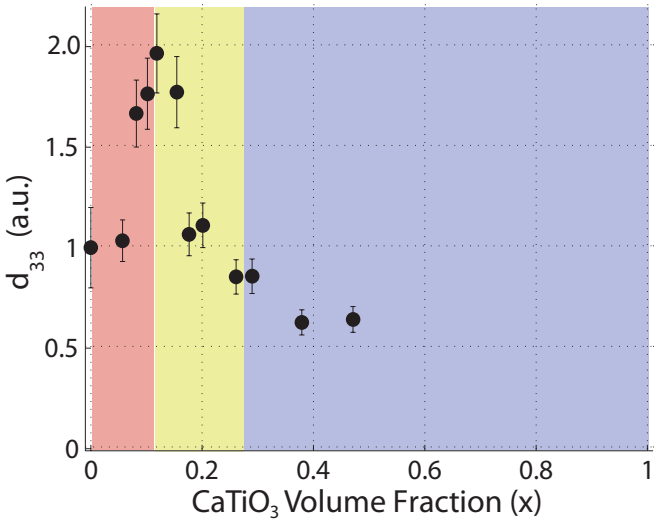

Figure 6.12: Measurement of the d_{33} piezoelectric coefficient of PTO/CTO superlattices as a function of $CaTiO_3$ volume fraction, normalized to the measured d_{33} on a thin film of $PbTiO_3$.

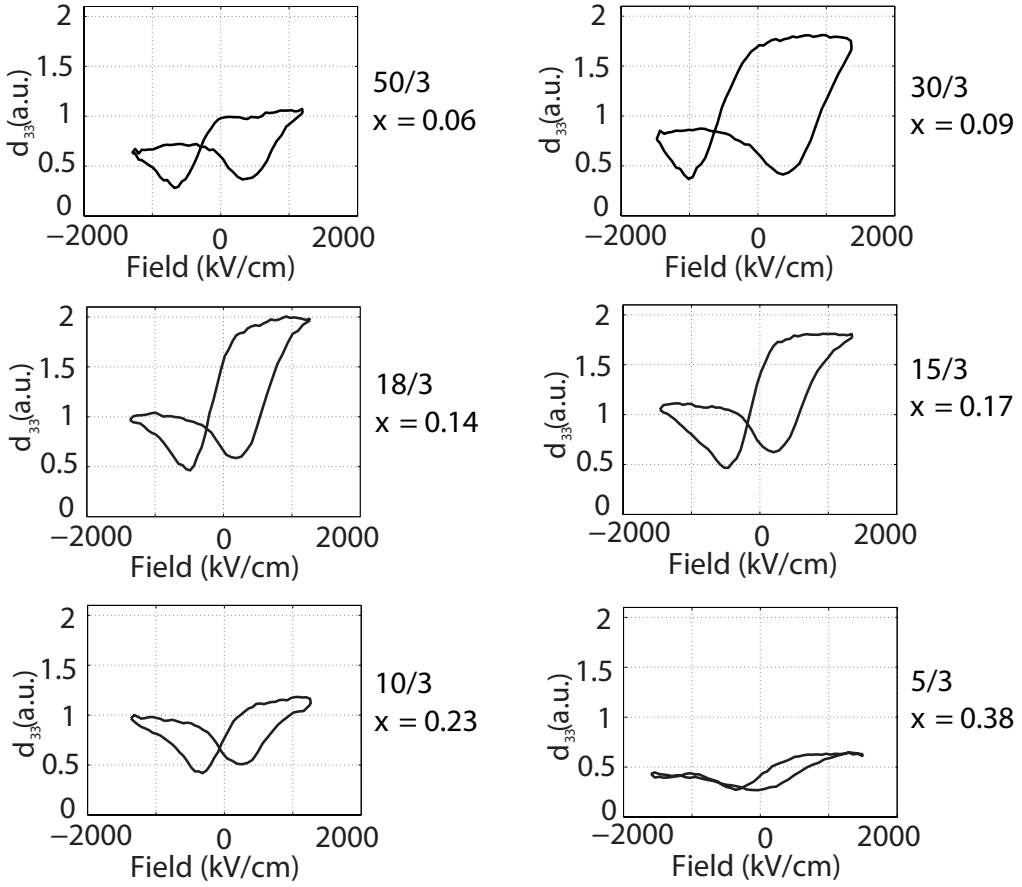

Figure 6.13: Measurements of d_{33} piezoresponse. Values in Figure 6.12 are determined by the largest measured piezoresponse, but enhancement is also seen on the negative field side.

ing to determine, and so the piezoresponse is measured using DART-PFM and SS-PFM, which uses the resonance of the cantilever tip, obtaining the loops shown in Figure 6.13. Measurements used to produce these loops used a drive voltage of 1.7 V with maximum DC biases of ± 15 V. The loops shown here have arbitrary units that are normalized to the highest measured piezoresponse for a pure $PbTiO_3$ film grown in our lab. However, an issue with this resonance technique is that the tip degrades from repeated measurements, causing measured piezoresponse to slowly decrease over time for measurements on the same sample. In order to prevent a bias in the measurements, samples were measured in various orders and the cantilever tip was frequently replaced, and this process was repeated until there was a clear and consistent relationship of piezoresponse magnitude from sample to sample. The values plotted in

Figure 6.12 are the maximum values of the piezoresponse for each sample, on the high positive field side, again normalized by the highest measured piezoresponse for a pure $PbTiO_3$ film, which by other means has been measured to be $\approx$ 60 pm/V [73]. The measured loops in Figure 6.13 consistently show higher values on the right side of the loop than compared to the left, even for the pure $PbTiO_3$ film. The asymmetry is most likely due to the difference between the top and bottom electrodes, with the gold coated AFM tip on top and the $SrRuO_3$ film on the bottom. Even so, the same enhancement of the piezoresponse as a function of $CaTiO_3$ volume fraction is seen whether the values are taken from the right or the left side of the loop. Although domain wall motion can contribute to a high piezoresponse, it is believed that the enhanced piezoresponse in the these samples comes from polarization rotation rather than domain wall motion, as here the spacing of the domains changes smoothly in the vicinity of the sharp peak in the piezoelectric and dielectric responses.

These results suggest a path forward toward the development of new piezoelectric materials. The enhancement of piezoresponse here is driven by the competition between preferred directions for polarization between two materials in a layered structure. As these samples are thin films, high electric fields can be readily applied, and the ordered layered structure that these samples have is a far simpler system to study by density functional theory methods than solid solutions which require very large supercells. It is expected that this material system will act as an excellent model system to help understand polarization rotation behavior in both pure single crystals and solid solutions.

Chapter 7

$PbTiO_3/BaTiO_3$ Superlattices

In the previous chapter, an enhancement of the piezoelectric response due to polarization rotation was demonstrated. Another well known mechanism which can drive large piezoelectric responses is the movement of domain walls. In this chapter we look at a material system in which polarization rotation is very unlikely to occur and in which our experimental measurements show are free of domain structure. It is found that even in a system which lacks these effects, such as PTO/BTO superlattices, there is still a modest increase in the piezoelectric coefficient, for superlattices as compared to single component films, which was initially predicted by first principles density functional calculations [16]. This suggests that interfaces in superlattices can also be a driving force for enhanced piezoresponse. In order to distinguish between bulk and interfacial properties of the superlattices, a parameterized energy expression can be constructed where the layers are each treated as strained bulk material with electric boundary conditions [16, 28, 87]. In particular the absence of overall free charge (short-circuit boundary conditions) implies continuity of the electrical displacement field across the interfaces, thereby relating the polarizations and the fields in each layer. In this chapter, plots of theoretical work performed by our collaborators at Rutgers and ORNL, Karin Rabe, Premi Chandra and Valentino Cooper, compare DFT values with predictions from this model. The role of our work was to verify the DFT predictions experimentally.

In Figures 7.1 and 7.2 we display $P(x)$ and $\frac{c}{a}(x)$ for both the model and DFT calculations on long-period superlattices. We note that in both cases the curves are not simply linear. There is excellent agreement between the first-principles and the model calculations for $P(x)$. Qualitatively this agreement is also good for the tetragonality, though we do note that here there is some difference for DFT points associated with the same PTO concentration (x) but with different periods (e.g. 1/1 and 2/2). The observed trends in the

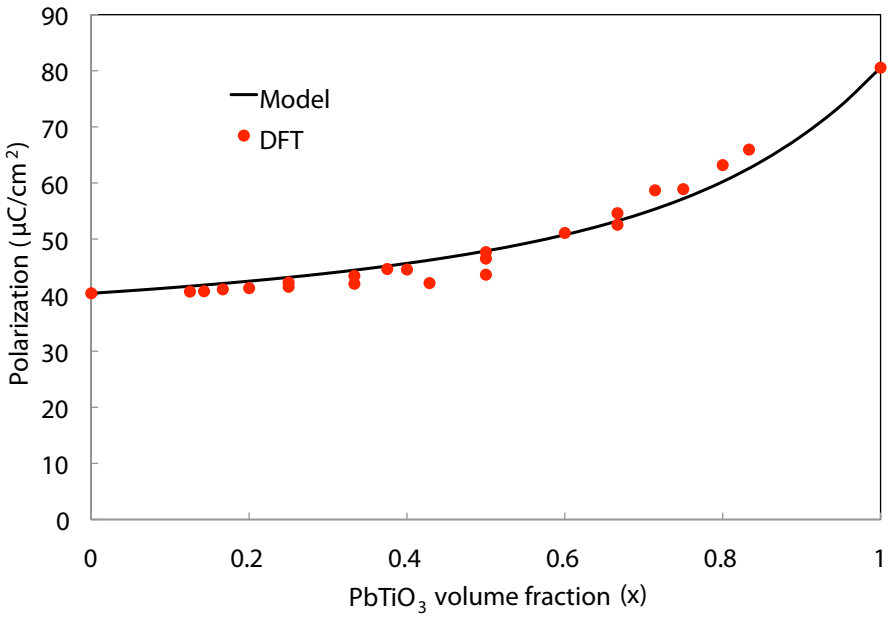

Figure 7.1: A comparison of the polarization predictions of PTO/BTO superlattices from DFT and the model of [16].

polarization and the tetragonality as a function of PTO concentration suggest that they can both be attributed to elastic and electrical boundary conditions imposed on layered bulk materials.

However this is certainly not the case for the piezoelectricity: in Figure 7.3 we display $d_{33}(x)$ again for model and DFT calculations. We observe that the model calculation of d_{33} has a different curvature (convex versus concave) than does the DFT data and indeed is consistently *less* than the linear extrapolation between the piezoelectric coefficients of the two bulk materials; more succinctly, there is no enhancement in the model d_{33} at all. Furthermore there is significant difference between DFT points associated with a given x with different periods, and this feature is certainly not captured by the bulk effective model. By separating the data according to the $BaTiO_3$ layer thickness it appears that both the magnitude and the position of the d_{33} maximum depend on the number of interfaces in the superlattice, as for any given composition, the superlattice with the thinnest $BaTiO_3$ layers will have the highest density of $PbTiO_3/BaTiO_3$ interfaces. The experimental results we present here do not explicitly examine superlattices with varying interfacial density, but rather seek to examine whether the shapes of the theoretical curves as predicted from DFT match those found in experiment.

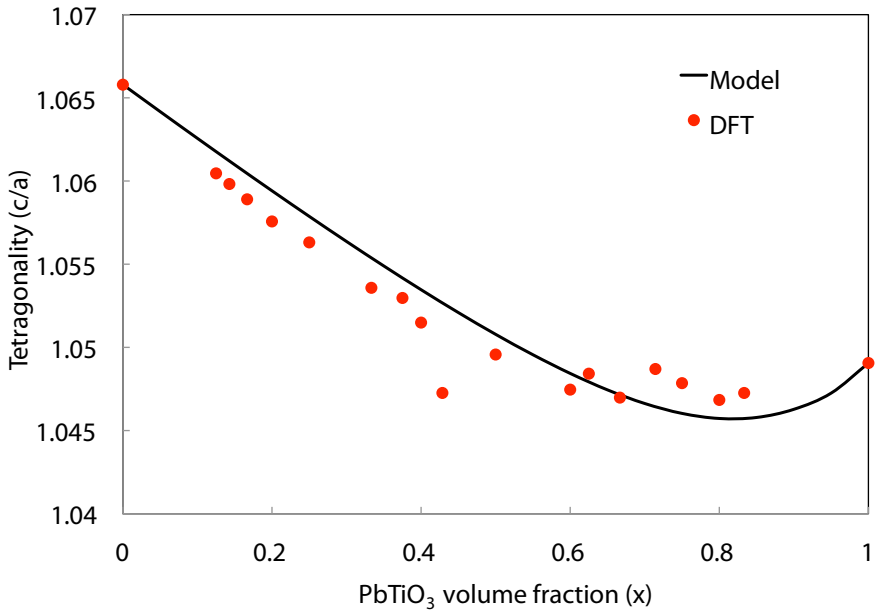

Figure 7.2: A comparison of the tetragonality predictions of PTO/BTO superlattices from DFT and the model of [16].

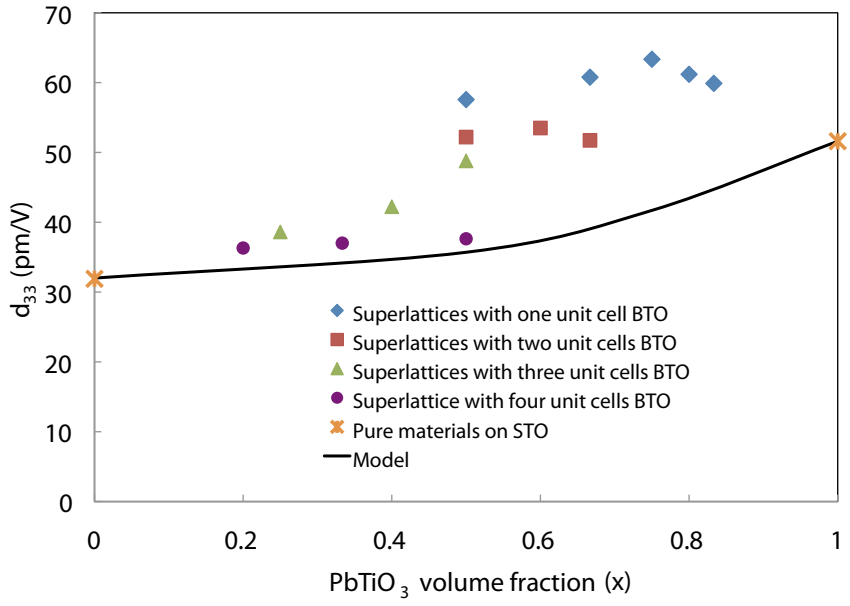

Figure 7.3: A comparison of the piezoresponse d_{33} predictions of PTO/BTO superlattices from DFT and the model of [16]. Different period superlattices, which have a different concentration of interfaces, show significant differences in their predicted piezoresponses.

7.1 Growth and Structural Properties

Superlattices of $PbTiO_3$ and $BaTiO_3$ with short superlattice wavelengths were grown in our lab by Benedikt Ziegler using off-axis RF magnetron sputter deposition, as described in Chapter 3, on (001) oriented $SrTiO_3$ substrates [84]. An earlier study of $PbTiO_3/BaTiO_3$ superlattices was performed with growth on MgO substrates [46] with long superlattice wavelengths. In this case, $PbTiO_3$ and $BaTiO_3$, having pseudocubic lattice parameters of a_{pc}=3.97 Å and a_{pc}=4.01 Å, respectively, were both under tensile strain, since MgO has an in-plane lattice parameters of a=4.213 Å, significantly larger than $SrTiO_3$ with in-plane lattice parameters of a=3.905 Å. Additionally, when under tensile strain, the $PbTiO_3$ layers here exhibited polarization along the in-plane direction, with respect to the substrate surface [46]. In the experiment presented here, both $PbTiO_3$ and $BaTiO_3$ are grown on $SrTiO_3$, and both materials are then under compressive strain. In this case, the polarizations of the $PbTiO_3$ and $BaTiO_3$ layers are expected to be in the out-of-plane direction [58]. Due to the large mismatch between $BaTiO_3$ and $SrTiO_3$, coherent growth of $PbTiO_3/BaTiO_3$ superlattices is challenging, especially with greater $BaTiO_3$ layer thicknesses in the superlattices. Despite this fact, a number of coherent superlattices of $PbTiO_3/BaTiO_3$ were successfully grown and their various structural, electrical, and piezoelectric properties were measured.

Before the superlattice growth, a number of thin films of $BaTiO_3$ were grown in order to study relaxation processes and find the optimum conditions for coherent growth. The various growth conditions such as the argon to oxygen ratio, growth temperature, and oxygen partial pressure were adjusted for the growth of a number of films. The structural characteristics were then measured with our Bruker D8 Discover diffractometer as described in Chapter 4. Films were found to be tetragonal when grown on $SrTiO_3$ with the polarization directed along the out-of-plane direction. The optimum growth conditions for $BaTiO_3$ were found to be at a pressure of 100 mTorr, an Ar:O ratio of 2:1, and a substrate temperature of 650 °C. A few films were grown on a 20 nm thick $SrRuO_3$ bottom electrode, which was grown in-situ, and interestingly, it was found that the presence of this bottom electrode was the most important parameter for achieving coherent $BaTiO_3$ growth. A direct comparison of two $BaTiO_3$ films, but with and without the additional 20 nm thick $SrRuO_3$ bottom electrode, is shown with x-ray diffraction in Figure 7.4. Both of the $BaTiO_3$ films shown in this figure are grown at the same conditions to a thickness of 22.5 nm. The tetragonality of the film grown on $SrRuO_3$ was c/a=1.078, with a=3.914 Å and c=4.205 Å, while without the $SrRuO_3$ electrode, the $BaTiO_3$ film had a much smaller tetragonality of c/a=1.031, with a=3.972 Å and c=4.095 Å. Reciprocal space maps of these films near the (113)

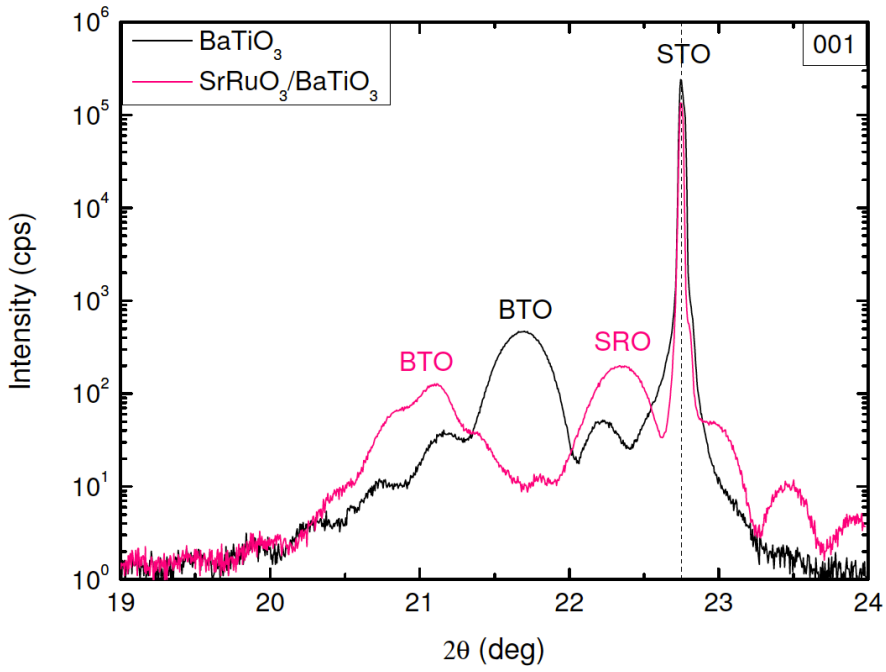

Figure 7.4: A 2θ-ω scan of $BaTiO_3$ films of 22.5 nm thickness grown with the same conditions (100 mTorr, Ar:O ratio of 2:1, and a substrate temperature of 650°C), either with or without a $SrRuO_3$ bottom electrode. With the bottom electrode, the tetragonality of $BaTiO_3$ is 1.078, and without it the tetragonality is 1.031. Reciprocal space maps of lower tetragonality $BaTiO_3$ films revealed considerable in-plane relaxation.

reflection show significant in-plane relaxation for the film grown without the $SrRuO_3$ electrode, but a high coherence of the film with respect to the substrate for the growth on $SrRuO_3$. Thinner films of $BaTiO_3$ on $SrRuO_3$ show even better coherence with the substrate. A 11.5 nm thin film of $BaTiO_3$ grown under the previous conditions on $SrRuO_3$ had lattice parameters of a=3.909 Å and c=4.254 Å, yielding a tetragonality of c/a=1.088.

In contrast to the growth of $BaTiO_3$ on $SrTiO_3$, coherent $PbTiO_3$ growth on $SrTiO_3$ is significantly easier due to the smaller lattice mismatch between $PbTiO_3$ and $SrTiO_3$. The optimal growth parameters of $PbTiO_3$ were found prior to superlattice growth, having an overall chamber pressure of 180 mTorr, an Ar:O ratio of 2:1, and a substrate temperature of 550 °C. Films grown at these parameters show coherent growth with the substrate and a high tetragonality of c/a=1.053, with polarization pointing along the out of plane direction. The tetragonality of $PbTiO_3$ was measured to be the same (within measurement uncertainty) for growth on a bottom $SrRuO_3$ electrode or growth directly

on the $SrTiO_3$ substrates.

The initial attempts to grow superlattices composed of $BaTiO_3$ and $PbTiO_3$ using the optimal growth conditions of each material was not successful, as Pb is very volatile and the $PbTiO_3$ quickly degrades when the sample is heated to the higher $BaTiO_3$ growth temperature. However, it was found that a 10 nm thick $BaTiO_3$ film could be grown at the lower, optimal $PbTiO_3$ growth temperature of 550 °C with only a small amount of relaxation, having lattice parameters of a=3.916 Å and c=4.180 Å. If the $BaTiO_3$ layers are grown sufficiently thin in a superlattice, they should not undergo relaxation and this should enable the overall superlattice to be highly strained. This lower temperature growth method was already proven successful for $PbTiO_3/SrTiO_3$ superlattices [27], where $SrTiO_3$ was grown at a lower than its optimal temperature in a superlattice with $PbTiO_3$. Superlattices of $PbTiO_3/BaTiO_3$ were then grown at the temperature of 550 °C with thin $BaTiO_3$ layers, which successfully produced highly coherent superlattices. An example of a successfully grown superlattice using this method is shown by x-ray diffraction scans for a 6/5 $PbTiO_3/BaTiO_3$ superlattice in Figure 7.5. The figure shows a 2θ-ω scan around the (001) diffraction peak in the top graph, with an intense main superlattice peak with a high average c lattice parameter, and many well defined superlattice satellite peaks. The bottom graph of the figure shows a reciprocal space map around the (113) diffraction peak, with the superlattice and the substrate aligned along the h=k=1 axis, indicating very little or no relaxation of the in-plane lattice parameter of the superlattice with respect to the $SrTiO_3$ substrate in-plane lattice parameter.

A number of superlattices were grown with an overall thickness of about 50 nm, which is an appropriate thickness for electrical measurements and piezoforce microscopy. At this thickness, samples with a concentration of $PbTiO_3$ greater than 50% were found to be coherent, while below this concentration of $PbTiO_3$, some relaxation was observed. By growing to lower overall thicknesses however, relaxation was avoided, as a superlattice of 33% $PbTiO_3$ grown to 20 nm total thickness and a pure $BaTiO_3$ film grown to 10 nm thickness both showed high coherence with the substrate. The tetragonality of strained $PbTiO_3/BaTiO_3$ superlattices is shown in Figure 7.6 as the black squares, and is additionally compared to the predictions from DFT and first principles. The shape of the measured tetragonality matches qualitatively to the theoretical predictions, with a minimum tetragonality around 70% $PbTiO_3$ in the superlattice.

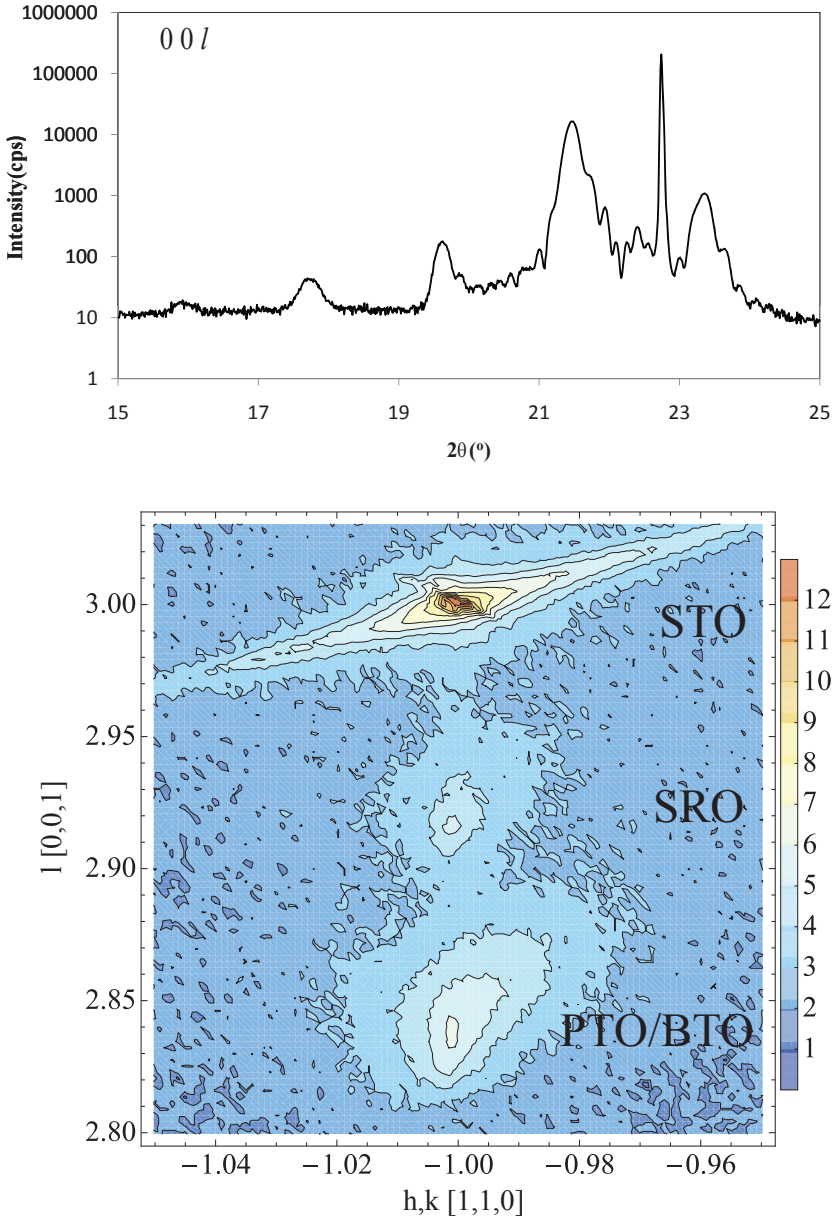

Figure 7.5: (Top) A 2θ-ω x-ray diffraction scan of a 6/5 $PbTiO_3/BaTiO_3$ superlattice on a $SrRuO_3$ bottom electrode showing the superlattice periodicity. (Bottom) A reciprocal space map around the (113) peak of this superlattice demonstrating that the entire structure had been grown constrained in plane to the $SrTiO_3$ lattice parameter.

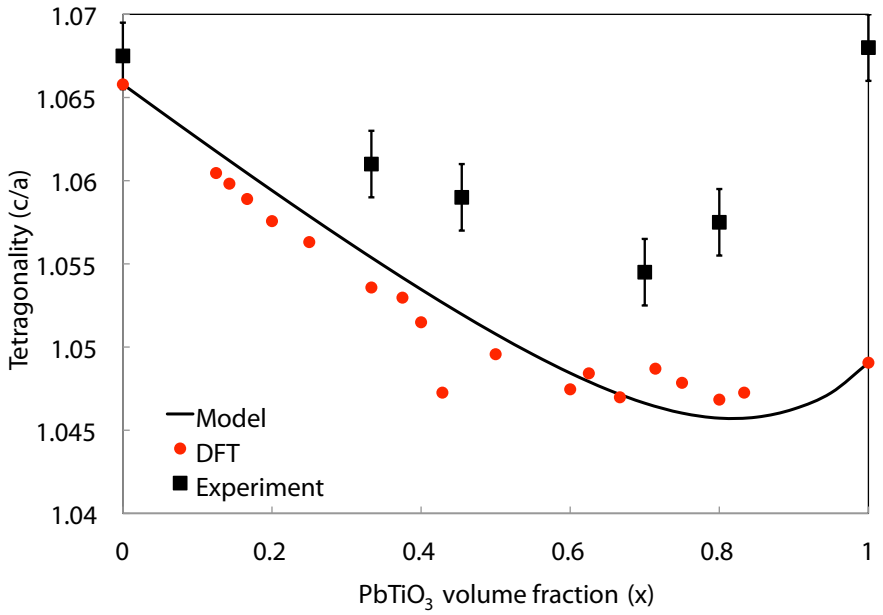

Figure 7.6: A comparison of the measured tetragonality of $PbTiO_3/BaTiO_3$ with DFT and first principles predictions.

7.2 Electrical and Piezoelectric Properties

The various electrical and piezoelectric properties of the superlattices were measured using the methods described in Chapter 5. First, gold electrodes were deposited on top of the samples ex-situ, and each sample was wirebonded to a copper base in order to make electrical connections with the bottom electrode. Polarization was measured using the PUND pulse technique with our home-built electrical measurement apparatus. Samples exhibited an asymmetry in the electrical characteristics, due to the different materials used for the top and bottom electrodes. This asymmetry was most pronounced by the measured leakage current at large negative fields, as can be seen in a typical hysteresis loop shown in Figure 7.7 (a). Due to this large leakage current on the negative field side, polarization values were determined from the right side of the hysteresis loop, which showed negligible leakage currents.

The measured polarization of each superlattice is shown in Figure 7.8 and is compared to predictions from theory, showing a very good agreement. Much like the measurement of tetragonality versus percentage $PbTiO_3$, the relationship between polarization versus percentage $PbTiO_3$ is nonlinear. Pure $BaTiO_3$ has a lower polarization than $PbTiO_3$, and superlattices show very little difference in polarization values until about 50% $PbTiO_3$. Then the

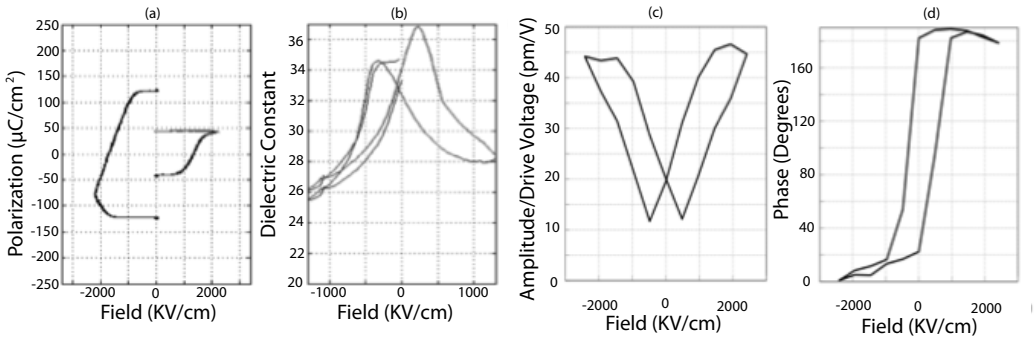

Figure 7.7: (a) Polarization-field and (b) dielectric constant-field loops measured on a 6/5 $PbTiO_3/BaTiO_3$ superlattice with gold, top, and $SrRuO_3$, bottom, electrodes. The piezoelectric response of a ferroelectric sample can also be measured by applying a small AC voltage (and larger DC bias) across the conductive tip and sample and measuring (c) amplitude and (d) phase of the oscillation.

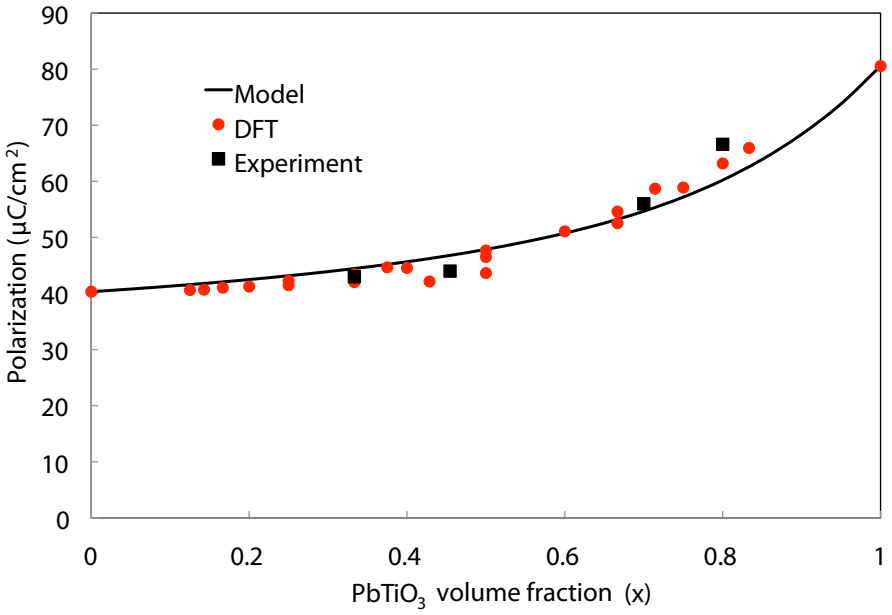

Figure 7.8: A comparison of measured polarization values of $PbTiO_3/BaTiO_3$ superlattice and first principles calculations versus the $PbTiO_3$ volume fraction of the superlattice.

slope of the graph changes, and polarization increases much more rapidly with increasing percentage $PbTiO_3$, in both experimental data and predictions from theory.

The dielectric constant was measured as a function of bias voltage using an LCR meter, obtaining loops similar to that of Figure 7.7 (b), which are typical of strongly ferroelectric materials. A value of dielectric constant for each superlattice was obtained by choosing the value of the dielectric constant at the intersection of the butterfly loop obtained from the dielectric constant versus bias field measurement. Then the dielectric constant for each superlattice was plotted versus the percentage of $PbTiO_3$ in the superlattice, as shown in top graph of Figure 7.9. The dielectric constant values for the $PbTiO_3/BaTiO_3$ superlattices are fairly modest when compared to $PbTiO_3/SrTiO_3$ [85]. Work on this system [85] based on Landau theory predictions suggest the larger than expected dielectric in this case is due to the presence of stripe-domain structures. This might imply the more modest dielectric constant of $PbTiO_3/BaTiO_3$ superlattice is due to a lack of stripe-domain structure, and since x-ray diffraction of $PbTiO_3/BaTiO_3$ superlattices here did not show diffuse scattering from periodic domain structures. This low dielectric constant behavior in $PbTiO_3/BaTiO_3$ superlattices may also be due to the large strain exerted by the $BaTiO_3$ layers in the superlattice.

Using an Asylum MFP-3D atomic force microscope in Piezo-Force Microscopy (PFM) mode, the out-of-plane strain was measured in response to an applied field. In this measurement, a small AC voltage is applied to a conducting cantilever and tip, creating a field between the tip and the bottom electrode. The piezoresponse causes the tip to oscillate as the surface height of the sample changes. A DC bias voltage is added to the AC signal, so that the piezoresponse is additionally measured as a function of the DC bias voltage. Depending on the polarization direction of the sample, the response is either in phase with the applied voltage or 180° out of phase with the applied voltage. An example of a measurement is shown in Figure 7.7 (c) and (d), showing the piezoresponse magnitude as a function of DC bias voltage and the associated phase. The piezoresponse of each superlattice was measured by Sara Callori, and normalized to the response of a pure $PbTiO_3$ film, obtaining the bottom graph of Figure 7.9. The magnitudes here are normalized with respect to the response of $PbTiO_3$ and given with arbitrary units, since numerous experimental issues affect the absolute magnitude of the piezoresponse. An enhancement of the d_{33} is observed at $PbTiO_3$ concentrations greater than 50%, with the peak appearing around $\sim 50\%$. At this peak, the magnitude of the enhancement is about 30% compared to pure $PbTiO_3$. The shape of the graph is in general agreement with DFT calculations shown in Figure 7.3.

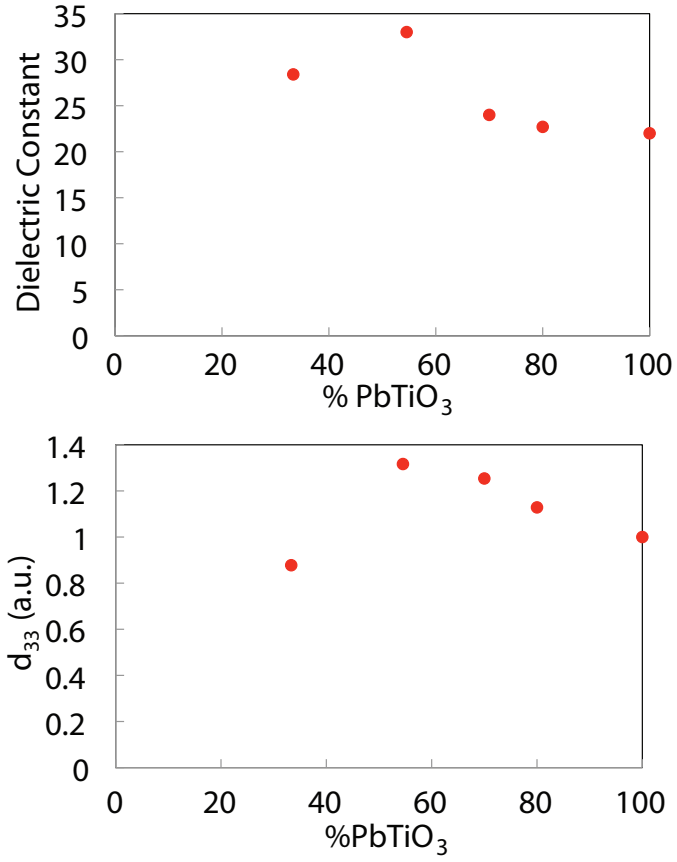

Figure 7.9: (Top) Measured values of dielectric constant versus percentage of $PbTiO_3$ in the superlattice. (Bottom) Measured values of the piezoelectric coefficient d_{33} from piezoforce microscopy measurements versus percentage of $PbTiO_3$ in the superlattice.

Overall, these results serve to confirm the key findings of the first principles calculations, showing an enhancement of the piezoresponse that cannot be explained by electrostatics and strain. Experimentally we do not see evidence of domains and the dielectric constants are small. As this effect is also seen in DFT simulations which do not have domains, we can rule out domain wall motion as the cause of the d_{33} enhancement in this system. Therefore, based both on a process of elimination, and the dependence on layer thickness seen in the first principles results in Figure 7.3 we suggest the enhancement of piezoresponse in this system is driven by the interfaces. Further investigation of this effect, both theoretically and experimentally, is underway.

Chapter 8

$BaTiO_3$ Growth

The growth of $BaTiO_3$ described in Chapter 7 showed a large, unexpected difference in the relaxation behaviors of $BaTiO_3$ films, depending on whether growth was directly on a $SrTiO_3$ substrate or whether growth was on a 20 nm $SrRuO_3$ electrode deposited on $SrTiO_3$ in-situ. In order to further investigate this effect, numerous experiments were carried out at the National Synchrotron Light Source (NSLS) X21 beamline, which has the capability for in-situ growth and x-ray diffraction. With this type of experiment, the in-plane and out-of-plane lattice parameters could be measured at various steps of the film growth, determining the lattice parameters as a function of film thickness. Using this setup, growth of $BaTiO_3$ was performed via sputter deposition on $SrTiO_3$ substrates both with and without a 20 nm thick $SrRuO_3$ electrode, deposited ex-situ in our home lab. Additionally, using the pulsed laser deposition (PLD) system available at the beamline, another comparison was made between growth using off-axis RF magnetron sputter deposition and growth using PLD. PLD is performed under different growth conditions compared to sputtering, such as lower pressures and the absence of argon gas. It is interesting to consider whether these different growth methods and the presence or absence of a $SrRuO_3$ bottom electrode will have an effect on the relaxation behaviors of grown $BaTiO_3$ films.

To perform this experiment, x-rays must enter the chamber, diffract from the sample, and then be measured over a range of angles with a detector. To accomplish this, the chamber is mounted onto a motorized, translatable table, which mimics the x, y, and z axes of a sample holder in a traditional diffractometer. The sample itself is mounted onto a motorized stage, which provides the ω or θ angle, as in the geometry of our home diffractometer, described in Chapter 4, or shown in Figure 4.1. The diffracted x-rays are measured with a detector attached to the outside of the chamber. The motorized table is also able to rotate, which when combined with the attached detector, mimics the 2θ

angle of a traditional diffractometer. In-plane lattice parameters are measured through a grazing incidence in-plane x-ray diffraction geometry. The required, movable angles for this geometry are provided by two other motors. One motor mimics the ϕ angle of Figure 4.1, while another motor moves the detector, which sweeps an arc in a vertical plane containing the x-ray beam. These various motors and detector measurements are controlled remotely through a control computer running SPEC software. The chamber also features two beryllium windows that are nearly transparent to x-rays, allowing for x-rays to enter and exit the chamber. Prior to mounting a sample, the sample holder and chamber is aligned such that the fixed incoming x-ray beam hits the center of the sample holder where the substrate will be placed.

Growth is achieved in this chamber by controlling the same growth parameters as described in Chapter 3, including the argon and oxygen flow rates, the overall chamber pressure, the sputter gun power, and the temperature of the substrate, where the substrate is heated by a resistive heater. The overall chamber pressure is controlled through a butterfly valve, and mass flow controllers connected to compressed air bottles, providing accurate flow rates of the gases into the chamber. The substrate is pasted onto a piece of silicon using silver paste, and this silicon piece is then mounted onto a sample holder that connects onto the motorized sample stage. The substrate temperature is measured indirectly by measuring the temperature of the silicon base using a pyrometer, which is calibrated with the known emissivity of the silicon, and additionally, a thermocouple is used to measure the temperature of the heater. A sputter gun is mounted through a flange into the chamber to provide a nearly off-axis geometry as in our home deposition chamber. Before sputtering is activated, the diffraction angles and offsets of the substrate at the growth temperature are found using an alignment procedure equivalent to the alignment performed in our home diffractometer, as described in Appendix A.1.

The growth and measurements were performed by alternating sputtering for a set amount of time, then measuring the film diffraction peaks in the vicinity of the substrate, both for in-plane and out-of-plane geometries. These diffraction scans were then used to calculate the a and c lattice parameters, and the overall $BaTiO_3$ thickness. For substrates with a $SrRuO_3$ electrode, diffraction scans were before $BaTiO_3$ growth in order to accurately measure the a and c lattice parameters and thickness of the $SrRuO_3$ electrode at the growth temperature.

In later experiments, the sputter gun was turned on and off through a remote switch in the control room, allowing for the possibility of measurements while sputtering. In this case, the diffraction angles were set to the half-bragg

position and x-ray intensity was monitored during growth. As material is deposited, small islands of one unit cell height form, and the surface roughens, causing a drop in measured intensity. As more material is deposited, the small islands on the surface will fill in, forming a new smooth surface 1 unit cell layer higher than previously, and x-ray reflectivity intensity will increase. Thus the measured x-ray reflectivity during growth shows oscillations in intensity, with each oscillation corresponding to the growth of one unit cell layer. However these growth oscillations tend to only be visible for the first few atomic cell layers grown, and then become less clear or distorted. This could be due to an overall roughening of the surface, which reaches a steady state as the film becomes thicker.

8.1 Results

A number of $BaTiO_3$ films were grown on $SrTiO_3$ substrates with and without a bottom $SrRuO_3$ electrodes. Additionally, $BaTiO_3$ films were grown either using sputtering or using PLD. Each x-ray diffraction scan along the (001) direction near the (001) $SrTiO_3$ substrate peak was fitted using the x-ray simulation program described in Chapter 4, obtaining a c lattice parameter of the $BaTiO_3$ film and its thickness. A series of measured x-ray diffraction scans of a $BaTiO_3$ film grown on $SrTiO_3$ for increasing thicknesses is shown in the top graph of Figure 8.1. The thickness is calculated by fitting these diffraction scans to simulations, shown in the bottom graph of Figure 8.1. In general, the c lattice parameter is related to the 2θ position of the most intense peak while the thickness is related to the spacings of the Laue oscillations. Smaller c lattice parameters of the film shifts the most intense film peak towards larger 2θ, closer to the substrate peak, and larger thicknesses decreases the spacings between the Laue oscillations. The simulations in the bottom graph show a very good matching with the measured diffraction peaks, demonstrating the accuracy of the calculations of the c lattice parameters and the overall film thickness. The simulations were especially useful for measuring the c lattice parameter and overall film thickness on $BaTiO_3$ films grown on $SrRuO_3$, since the x-ray diffraction from each of these films convolutes, distorting the diffraction peaks. The in-plane lattice parameters were measured in the grazing incidence in-plane diffraction geometry. Here, the center of the main film peak is directly used to calculate the a lattice parameter using Bragg's Law (4.1) for films greater than 10 unit cells thick. Films below this thickness resulted in in-plane diffraction with insufficient intensity to provide accurate measurements.

Using these fitting methods and calculations, the a and c lattice parameters were calculated at multiple stages of a $BaTiO_3$ film growth. This process

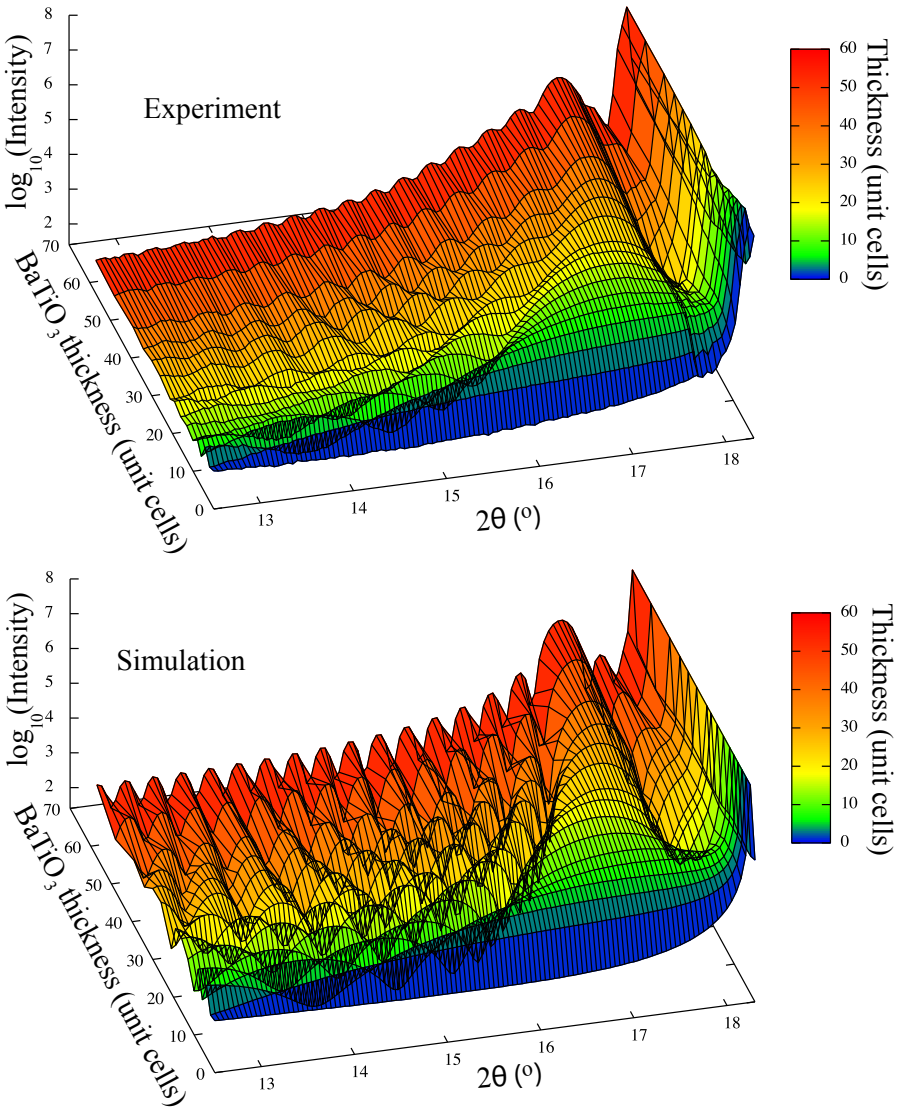

Figure 8.1: A comparison of measured x-ray diffraction scans at different $BaTiO_3$ film thicknesses (Top) with simulated x-ray diffraction scans that were used to accurately calculate the thickness (Bottom).

was repeated for the different combinations of growth method and presence of $SrRuO_3$ electrode to generate the results shown in Figure 8.2, which plot the lattice parameters against the overall film thickness in each case. We see a number of surprising results from this data. First, we examine the lattice parameters of the sputtered films, indicated by the green and purple lines on the graphs. The a lattice parameters show a small, consistent difference between growth on the $SrRuO_3$ electrode and growth on $SrTiO_3$, where relaxation is consistently less on $SrRuO_3$, confirming the result produced from $BaTiO_3$ in our home deposition system. However, the difference seen from deposition in our home system was significantly larger between films grown with and without the $SrRuO_3$ electrode. The c lattice parameters for these curves are not separated however, where the c lattice parameter is larger for growth $SrRuO_3$ only for thin films less than 15 unit cell layers thick. Interestingly, at larger $BaTiO_3$ thicknesses than about 15 unit cell layers, the growth directly $SrTiO_3$ actually shows a larger c lattice parameter. For both of these films, there is a somewhat linear trend between total thickness and the amount of relaxation.

Growth using pulsed laser deposition, on the other hand, shows a drastic difference in relaxation effects depending on the presence or not of a $SrRuO_3$ electrode. The growth on $SrRuO_3$ is found to be highly strained over a large range of thickness, exhibiting no relaxation of the in-plane lattice parameter until about 30 unit cell layers thickness. The c lattice parameter also plateaus until this thickness, showing little or no relaxation. At greater thicknesses, relaxation begins, but still remains much more coherent than both of the films grown with sputtering. Surprisingly, the PLD growth directly on $SrTiO_3$ exhibited more relaxation than any other $BaTiO_3$ film growth, where the $BaTiO_3$ c lattice parameter quickly plateaus at about 15 unit cell layer thickness. The a lattice parameter also reaches a plateau, but not until about 30 unit cell layer thickness.

These results raise further questions about the relaxation behavior of $BaTiO_3$ on $SrTiO_3$. The difference between growth on $SrRuO_3$ compared to growth directly on the $SrTiO_3$ is likely due to depolarization field effects on the $BaTiO_3$, which may be ferroelectric at its growth temperature when strained to the in-plane lattice parameters of $SrTiO_3$. It is also possible that the interface between $BaTiO_3$ and $SrRuO_3$ compared to that of $BaTiO_3$ and $SrTiO_3$ is different enough to have a significant effect on these very thin films. The difference between sputtering and PLD may stem from the overall chamber pressure difference compared to sputtering, or the difference in oxygen partial pressure, or the different energetics of the vaporized $BaTiO_3$ reaching the substrate.

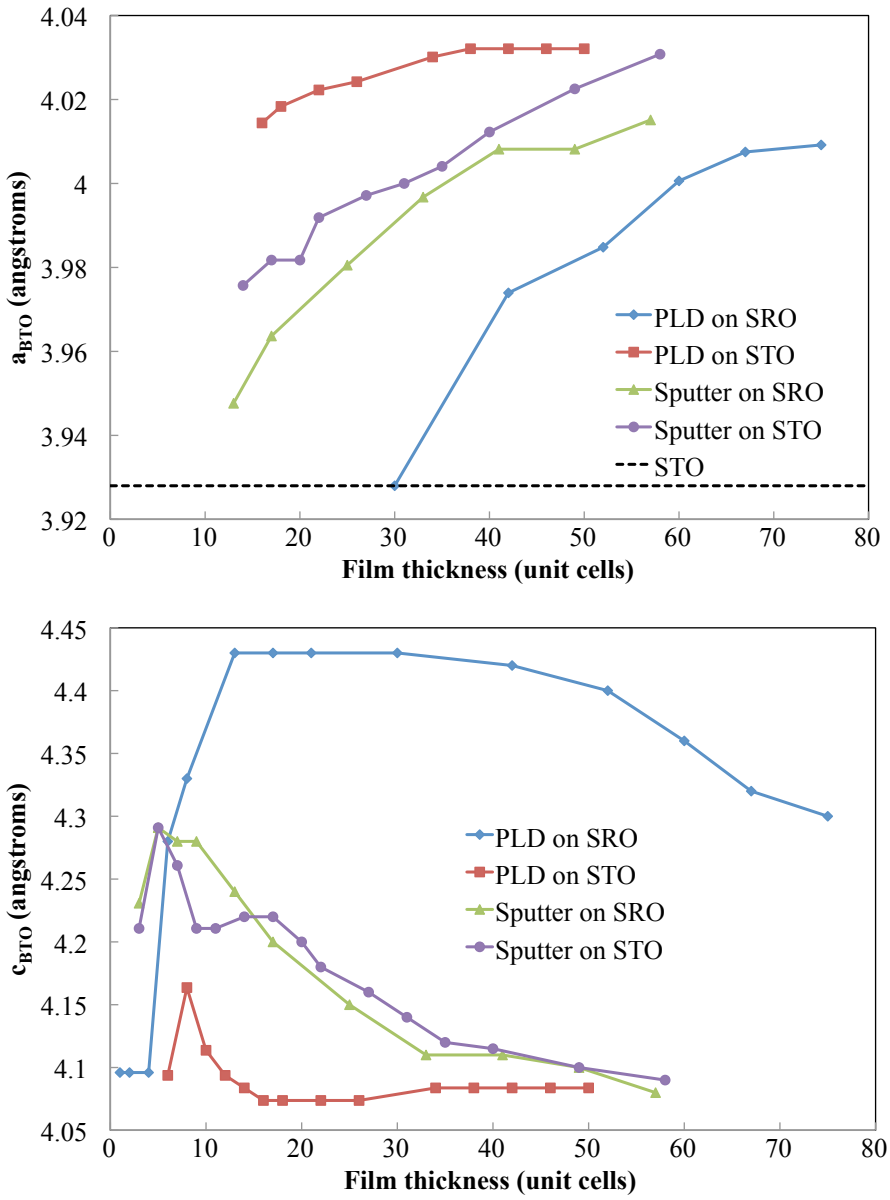

Figure 8.2: A comparison of growth and relaxation of films made using pulsed laser deposition and sputtering for $BaTiO_3$ deposited on $SrTiO_3$ with and without a 20 nm thick $SrRuO_3$ bottom electrode. (Top) The measured in-plane lattice parameter, a, as a function of film thickness. (Bottom) The out-of-plane lattice parameter, c, as a function of film thickness.

8.2 Experimental Improvements

These results will be further studied to try to better understand the mechanisms responsible for the relaxation behaviors observed. To facilitate this, a number of improvements, largely developed by myself, have been made to the experimental process over time to improve the efficiency of conducting this experiment. Initially, the sputter gun was powered on and off manually inside of the hutch where the chamber is located, so measurements could not be made during sputtering. This was improved through the use of a remote switch with adjustable RF power control, so that x-ray diffraction measurements of the reflectivity could then be made while sputtering. Most recently, a new chamber was purchased and an automation process was developed, greatly improving the efficiency of growth and allowing for growth parameter monitoring or adjustment during the experiment. The present setup now uses a Labview program similar to that used in our home deposition system, but is controllable through the control computer that runs the various diffraction angle motors. Text strings are sent through an ethernet connection from the control computer to another computer running Labview inside the hutch. The Labview program interprets the strings, and has to capability to sputter for a user-defined amount of time, change or measure the overall chamber pressure, and change or measure the heater temperature. While sputtering, these growth parameters are automatically measured and recorded in time. Additionally, since x-ray scans can be automated, an experiment that alternates growth and scanning can be automated, only requiring monitoring by a user, significantly reducing the time gaps that previously existed from manually operating each part of the experiment. In addition to improving the time efficiency of experiments, these capabilities allow for new experiments to be conducted in order to better understand the effect of different growth parameters on the film growth.

Chapter 9

Conclusions

In this thesis, two different methods have been presented to engineer enhanced piezoelectricity in ferroelectric superlattices. Superlattices composed of $PbTiO_3$ and $CaTiO_3$ were grown in various material ratios and show a rotation in the polarization orientation from sample to sample. At the compositional phase transition from monoclinic C to tetragonal, we measure a piezoresponse that is double that of pure $PbTiO_3$. The superlattice system also shows an enhanced dielectric constant and interesting polarization switching dynamics. This system is expected to act as an excellent model system to better understand polarization rotation and its associated effects in both single crystals and solid solutions.

In contrast to this system, superlattices composed of $PbTiO_3$ and $BaTiO_3$, having purely out-of-plane polarization orientations, were also shown to have an enhanced piezoresponse about 40% larger than a pure $PbTiO_3$. The results confirm the key findings of the first principles calculations, showing that the piezoelectric enhancement is not due to electrostatics and strain. Additionally, given the small dielectric constants and the lack of domains observed in the system, the piezoelectric enhancement is not due to domain wall motion. These results suggest the enhancement is instead driven by interfaces in the system. Further investigation into this superlattice system is in progress both theoretically and experimentally.

In order to produce fully strained superlattices of $PbTiO_3$ and $BaTiO_3$, it is necessary to understand the growth conditions leading to full strained $BaTiO_3$. Growth experiments both in our home deposition chamber and the chamber at the NSLS X21 beamline show a significant reduction in relaxation effects when growth is performed on a bottom $SrRuO_3$ electrode. Improvements to the experimental setup at the beamline will allow for additional experiments to be conducted, facilitating future growths of $PbTiO_3/BaTiO_3$ in further study of the piezoelectric enhancement of this system.

Bibliography

[1] Pablo Aguado-Puente and Javier Junquera. Structural and energetic properties of domains in $PbTiO_3/SrTiO_3$ superlattices from first principles. *Phys. Rev. B*, 85:184105, May 2012. doi: 10.1103/PhysRevB.85.184105. URL http://link.aps.org/doi/10.1103/PhysRevB.85.184105.

[2] Pablo Aguado-Puente, Pablo García-Fernández, and Javier Junquera. Interplay of couplings between antiferrodistortive, ferroelectric, and strain degrees of freedom in monodomain $PbTiO_3/SrTiO_3$ superlattices. *Phys. Rev. Lett.*, 107:217601, Nov 2011. doi: 10.1103/PhysRevLett.107.217601. URL http://link.aps.org/doi/10.1103/PhysRevLett.107.217601.

[3] P. B. Allen, H. Berger, O. Chauvet, L. Forro, T. Jarlborg, A. Junod, B. Revaz, and G. Santi. Transport properties, thermodynamic properties, and electronic structure of $SrRuO_3$. *Phys. Rev. B*, 53:4393–4398, Feb 1996. doi: 10.1103/PhysRevB.53.4393. URL http://link.aps.org/doi/10.1103/PhysRevB.53.4393.

[4] N.W. Ashcroft and N.D. Mermin. *Solid state physics*. Science: Physics. Saunders College, 1976. ISBN 9780030493461. URL http://books.google.com/books?id=FRZRAAAAMAAJ.

[5] E. Barsoukov and J.R. Macdonald. *Impedance Spectroscopy: Theory, Experiment, and Applications*. Wiley, 2005. ISBN 9780471716228. URL http://books.google.com/books?id=8hNkOWO_DLwC.

[6] L. Bellaiche, Alberto Garcia, and David Vanderbilt. Electric-field induced polarization paths in $Pb(Zr_{1-x}Ti_x)O_3$ alloys. *Phys. Rev. B*, 64:060103, Jul 2001. doi: 10.1103/PhysRevB.64.060103. URL http://link.aps.org/doi/10.1103/PhysRevB.64.060103.

[7] F Bernardini, V Fiorentini, and D Vanderbilt. Spontaneous polarization and piezoelectric constants of III-V nitrides. *Physical Review B*, 56(16): 10024–10027, Oct 15 1997. ISSN 0163-1829.

[8] P.R. Bevington and D.K. Robinson. *Data reduction and error analysis for the physical sciences*. McGraw-Hill Higher Education. McGraw-Hill, 2003. ISBN 9780072472271. URL `http://books.google.com/books?id=0poQAQAAIAAJ`.

[9] Alastair D. Bruce, K. A. Müller, and W. Berlinger. Order-disorder behavior at displacive structural phase transitions. *Phys. Rev. Lett.*, 42:185–188, Jan 1979. doi: 10.1103/PhysRevLett.42.185. URL `http://link.aps.org/doi/10.1103/PhysRevLett.42.185`.

[10] Claudia Bungaro and K. M. Rabe. Coexistence of antiferrodistortive and ferroelectric distortions at the $PbTiO_3$ (001) surface. *Phys. Rev. B*, 71:035420, Jan 2005. doi: 10.1103/PhysRevB.71.035420. URL `http://link.aps.org/doi/10.1103/PhysRevB.71.035420`.

[11] G. Catalan, A. Janssens, G. Rispens, S. Csiszar, O. Seeck, G. Rijnders, D. H. A. Blank, and B. Noheda. Polar domains in lead titanate films under tensile strain. *Phys. Rev. Lett.*, 96:127602, Mar 2006. doi: 10.1103/PhysRevLett.96.127602. URL `http://link.aps.org/doi/10.1103/PhysRevLett.96.127602`.

[12] H. M. Christen, J. H. Nam, H. S. Kim, A. J. Hatt, and N. A. Spaldin. Stress-induced R-M_A-M_C-T symmetry changes in $BiFeO_3$ films. *Phys. Rev. B*, 83:144107, Apr 2011. doi: 10.1103/PhysRevB.83.144107. URL `http://link.aps.org/doi/10.1103/PhysRevB.83.144107`.

[13] Ying-Hao Chu, Lane W. Martin, Mikel B. Holcomb, Martin Gajek, Shu-Jen Han, Qing He, Nina Balke, Chan-Ho Yang, Donkoun Lee, Wei Hu, Qian Zhan, Pei-Ling Yang, Arantxa Fraile-Rodriguez, Andreas Scholl, Shan X. Wang, and R. Ramesh. Electric-field control of local ferromagnetism using a magnetoelectric multiferroic. *Nature MaterialS*, 7(6):478–482, Jun 2008. ISSN 1476-1122. doi: {10.1038/nmat2184}.

[14] Eric Cockayne and Benjamin P. Burton. Phonons and static dielectric constant in $CaTiO_3$ from first principles. *Phys. Rev. B*, 62:3735–3743, Aug 2000. doi: 10.1103/PhysRevB.62.3735. URL `http://link.aps.org/doi/10.1103/PhysRevB.62.3735`.

[15] R.E. Cohen. Origin of ferroelectricity in perovskite oxides. *Nature*, 358 (6382):136–138, Jul 9 1992. ISSN 0028-0836. doi: 10.1038/358136a0.

[16] Valentino R. Cooper and Karin M. Rabe. Enhancing piezoelectricity through polarization-strain coupling in ferroelectric superlattices. *Phys.*

Rev. B, 79:180101, May 2009. doi: 10.1103/PhysRevB.79.180101. URL http://link.aps.org/doi/10.1103/PhysRevB.79.180101.

[17] M. Dawber, K. M. Rabe, and J. F. Scott. Physics of thin-film ferroelectric oxides. *Rev. Mod. Phys.*, 77:1083–1130, Oct 2005. doi: 10.1103/RevModPhys.77.1083. URL http://link.aps.org/doi/10.1103/RevModPhys.77.1083.

[18] C.-J. Eklund, C. J. Fennie, and K. M. Rabe. Strain-induced ferroelectricity in orthorhombic $CaTiO_3$ from first principles. *Phys. Rev. B*, 79:220101, Jun 2009. doi: 10.1103/PhysRevB.79.220101. URL http://link.aps.org/doi/10.1103/PhysRevB.79.220101.

[19] Cb Eom, Rj Cava, Rm Fleming, Jm Phillips, Rb Vandover, Jh Marshall, Jwp Hsu, Jj Krajewski, and Wf Peck. Single-crystal epitaxial thin-films of the isotropic metallic oxides $Sr_{(1-X)}Ca_XRuO_3$ ($0 \leq X \leq 1$). *Science*, 258 (5089):1766–1769, Dec 11 1992. ISSN 0036-8075. doi: {10.1126/science.258.5089.1766}.

[20] B. Noheda et al. A monoclinic ferroelectric phase in the $Pb(Zr_{1-x}Ti_x)O_3$ solid solution . *Appl. Phys. Lett.*, 74:2059, Feb 1999. doi: 10.1063/1.123756. URL http://dx.doi.org/10.1063/1.123756.

[21] E. Bousquet et al. Improper ferroelectricity in perovskite oxide artificial superlattices. *Nature*, 452:732, Apr 2008. doi: 10.1038/nature06817. URL http://www.nature.com/nature/journal/v452/n7188/full/nature06817.html.

[22] J.H. Haeni et al. Room-temperature ferroelectricity in strained $SrTiO_3$. *Nature*, 430:758–761, Aug 2004. doi: 10.1038/nature02773. URL http://www.nature.com/nature/journal/v430/n7001/full/nature02773.html.

[23] J.H. Lee et al. A strong ferroelectric ferromagnet created by means of spinlattice coupling. *Nature*, 466:954–958, Aug 2010. doi: doi: 10.1038/nature09331. URL http://www.nature.com/nature/journal/v466/n7309/full/nature09331.html.

[24] Ji Young Jo et al. Component-specific electromechanical response in a ferroelectric/dielectric superlattice. *Phys. Rev. B*, 82:174116, Nov 2010. doi: 10.1103/PhysRevB.82.174116. URL http://link.aps.org/doi/10.1103/PhysRevB.82.174116.

[25] K. J. Choi et al. Enhancement of Ferroelectricity in Strained $BaTiO_3$ Thin Films. *Science*, 306(5698):1005–1009, 2004. doi: 10.1126/science.1103218. URL http://www.sciencemag.org/content/306/5698/1005.abstract.

[26] M. Ahart et al. Origin of morphotropic phase boundaries in ferroelectrics. *Nature*, 451:545, 2008. doi: 10.1038/nature06459. URL http://www.nature.com/nature/journal/v451/n7178/full/nature06459.html.

[27] M. Dawber et al. Unusual Behavior of the Ferroelectric Polarization in $PbTiO_3/SrTiO_3$ Superlattices. *Phys. Rev. Lett.*, 95:177601, Oct 2005. doi: 10.1103/PhysRevLett.95.177601. URL http://link.aps.org/doi/10.1103/PhysRevLett.95.177601.

[28] M. Dawber et al. Tailoring the properties of artificially layered ferroelectric superlattices. *Advanced Materials*, 19(23):4153–4159, 2007. ISSN 1521-4095. doi: 10.1002/adma.200700965. URL http://dx.doi.org/10.1002/adma.200700965.

[29] P. A. Fleury, J. F. Scott, and J. M. Worlock. Soft Phonon Modes and the 110° K Phase Transition in $SrTiO_3$. *Phys. Rev. Lett.*, 21:16–19, Jul 1968. doi: 10.1103/PhysRevLett.21.16. URL http://link.aps.org/doi/10.1103/PhysRevLett.21.16.

[30] Dillon D. Fong, G. Brian Stephenson, Stephen K. Streiffer, Jeffrey A. Eastman, Orlando Auciello, Paul H. Fuoss, and Carol Thompson. Ferroelectricity in ultrathin perovskite films. *Science*, 304(5677):1650–1653, 2004. doi: 10.1126/science.1098252. URL http://www.sciencemag.org/content/304/5677/1650.abstract.

[31] H. Fu and R.E. Cohen. Polarization rotation mechanism for ultrahigh electromechanical response in single-crystal piezoelectrics. *Nature*, 403:281, Jan 2000. doi: 10.1038/35002022. URL http://www.nature.com/nature/journal/v403/n6767/full/403281a0.html.

[32] Ramaratnam Ganesh and Edward Goo. Dielectric and Ordering Behavior in $Pb_xCa_{1-x}TiO_3$. *Journal of the American Ceramic Society*, 80(3):653–662, 1997. ISSN 1551-2916. doi: 10.1111/j.1151-2916.1997.tb02881.x. URL http://dx.doi.org/10.1111/j.1151-2916.1997.tb02881.x.

[33] M. Ghita, M. Fornari, D. J. Singh, and S. V. Halilov. Interplay between A-site and B-site driven instabilities in perovskites. *Phys. Rev. B*, 72:054114, Aug 2005. doi: 10.1103/PhysRevB.72.054114. URL http://link.aps.org/doi/10.1103/PhysRevB.72.054114.

[34] C. Giacovazzo. *Fundamentals of Crystallography*. IUCr texts on crystallography. Oxford University Press, 2002. ISBN 9780198509585. URL http://books.google.com/books?id=77pUdgxcar0C.

[35] A Gruverman, BJ Rodriguez, C Dehoff, JD Waldrep, AI Kingon, RJ Nemanich, and JS Cross. Direct studies of domain switching dynamics in thin film ferroelectric capacitors. *Applied Physics Letters*, 87(8), Aug 22 2005. ISSN 0003-6951. doi: {10.1063/1.2010605}.

[36] R. Guo, L. E. Cross, S-E. Park, B. Noheda, D. E. Cox, and G. Shirane. Origin of the high piezoelectric response in $PbZr_{1-x}Ti_xO_3$. *Phys. Rev. Lett.*, 84:5423–5426, Jun 2000. doi: 10.1103/PhysRevLett.84.5423. URL http://link.aps.org/doi/10.1103/PhysRevLett.84.5423.

[37] B. Jaffe, R. S. Roth, and S. Marzullo. Piezoelectric properties of lead zirconate-lead titanate solid-solution ceramics. *J. Appl. Phys.*, 85:809–810, Mar 1954. doi: 10.1063/1.1721741. URL http://dx.doi.org/10.1063/1.1721741.

[38] B. Jaffe, W.R. Cook, and H.L. Jaffe. *Piezoelectric ceramics*. Non-metallic solids. Academic Press, 1971. ISBN 9780123795502. URL http://books.google.com/books?id=ZApTAAAAMAAJ.

[39] Stephen Jesse, Ho Nyung Lee, and Sergei V. Kalinin. Quantitative mapping of switching behavior in piezoresponse force microscopy. *Review Of Scientific Instruments*, 77(7), Jul 2006. ISSN 0034-6748. doi: {10.1063/1.2214699}.

[40] Karen Johnston, Xiangyang Huang, J. B. Neaton, and Karin M. Rabe. First-principles study of symmetry lowering and polarization in $BaTiO_3/SrTiO_3$ superlattices with in-plane expansion. *Phys. Rev. B*, 71:100103, Mar 2005. doi: 10.1103/PhysRevB.71.100103. URL http://link.aps.org/doi/10.1103/PhysRevB.71.100103.

[41] C. W. Jones, P. D. Battle, P. Lightfoot, and W. T. A. Harrison. The structure of $SrRuO_3$ by time-of-flight neutron powder diffraction. *Acta Crystallographica Section C*, 45(3):365–367, Mar 1989. doi: 10.1107/S0108270188012077. URL http://dx.doi.org/10.1107/S0108270188012077.

[42] J Junquera and P Ghosez. Critical thickness for ferroelectricity in perovskite ultrathin films. *Nature*, 422(6931):506–509, Apr 3 2003. ISSN 0028-0836. doi: {10.1038/nature01501}.

[43] Hf Kay and P Vousden. Symmetry Changes In Barium Titanate At Low Temperatures And Their Relation To Its Ferroelectric Properties. *Philosophical Magazine*, 40(309):1019–1040, 1949. ISSN 0031-8086.

[44] C. Kittel. *Introduction to Solid State Physics*. John Wiley & Sons, 2004. ISBN 9780471415268. URL `http://books.google.com/books?id=kym4QgAACAAJ`.

[45] Shou-Yi Kuo, Chung-Ting Li, and Wen-Feng Hsieh. Lattice dynamics of perovskite $Pb_xCa_{1-x}TiO_3$. *Phys. Rev. B*, 69:184104, May 2004. doi: 10.1103/PhysRevB.69.184104. URL `http://link.aps.org/doi/10.1103/PhysRevB.69.184104`.

[46] F. Le Marrec, R. Farhi, M. El Marssi, J. L. Dellis, M. G. Karkut, and D. Ariosa. Ferroelectric $PbTiO_3/BaTiO_3$ superlattices: Growth anomalies and confined modes. *Phys. Rev. B*, 61:R6447–R6450, Mar 2000. doi: 10.1103/PhysRevB.61.R6447. URL `http://link.aps.org/doi/10.1103/PhysRevB.61.R6447`.

[47] HN Lee, HM Christen, MF Chisholm, CM Rouleau, and DH Lowndes. Strong polarization enhancement in asymmetric three-component ferroelectric superlattices. *Nature*, 433(7024):395–399, Jan 27 2005. ISSN 0028-0836. doi: {10.1038/nature03261}.

[48] M.E. Lines and A.M. Glass. *Principles and Applications of Ferroelectrics and Related Materials*. Oxford Classic Texts in Physical Sciences. Clarendon Press, 1977. ISBN 9780198507789. URL `http://books.google.com/books?id=p6ruJH8C84kC`.

[49] JP Maria, HL McKinstry, and S Trolier-McKinstry. Origin of preferential orthorhombic twinning in $SrRuO_3$ epitaxial thin firms. *Applied Physics Letters*, 76(23):3382–3384, Jun 5 2000. ISSN 0003-6951. doi: {10.1063/1.126654}.

[50] L. J. McGilly and J. M. Gregg. Scaling of superdomain bands in ferroelectric dots. *Applied Physics Letters*, 98(13), Mar 28 2011. ISSN 0003-6951. doi: {10.1063/1.3571560}.

[51] V Nagarajan, A Roytburd, A Stanishevsky, S Prasertchoung, T Zhao, L Chen, J Melngailis, O Auciello, and R Ramesh. Dynamics of ferroelastic domains in ferroelectric thin films. *Nature Materials*, 2(1):43–47, Jan 2003. ISSN 1476-1122. doi: {10.1038/nmat800}.

[52] J.B. Neaton and K.M. Rabe. Theory of polarization enhancement in epitaxial $BaTiO_3/SrTiO_3$ superlattices. *Appl. Phys. Lett*, 82:1586, Jan 2003. doi: http://dx.doi.org/10.1063/1.1559651. URL `http://apl.aip.org/resource/1/applab/v82/i10/p1586_s1`.

[53] B. Noheda, D. E. Cox, G. Shirane, S.-E. Park, L. E. Cross, and Z. Zhong. Polarization rotation via a monoclinic phase in the piezoelectric 92% $PbZn_{1/3}Nb_{2/3}O_3$-8% $PbTiO_3$. *Phys. Rev. Lett.*, 86:3891–3894, Apr 2001. doi: 10.1103/PhysRevLett.86.3891. URL `http://link.aps.org/doi/10.1103/PhysRevLett.86.3891`.

[54] B. Noheda, D. E. Cox, G. Shirane, J. Gao, and Z.-G. Ye. Phase diagram of the ferroelectric relaxor $(1-x)PbMg_{1/3}Nb_{2/3}O_3 - xPbTiO_3$. *Phys. Rev. B*, 66:054104, Aug 2002. doi: 10.1103/PhysRevB.66.054104. URL `http://link.aps.org/doi/10.1103/PhysRevB.66.054104`.

[55] J.F. Nye. *Physical Properties of Crystals: Their Representation by Tensors and Matrices*. Oxford Science Publications. Clarendon Press, 1985. ISBN 9780198511656. URL `http://books.google.com/books?id=ugwql-uVB44C`.

[56] International Union of Crystallography. *International tables for X-ray crystallography*. Number v. 4 in International Tables for X-ray Crystallography. Kynoch Press, 1969. URL `http://books.google.com/books?id=3AvwAAAAMAAJ`.

[57] SE Park and TR Shrout. Ultrahigh strain and piezoelectric behavior in relaxor based ferroelectric single crystals. *Journal Of Applied Physics*, 82 (4):1804–1811, Aug 15 1997. ISSN 0021-8979. doi: {10.1063/1.365983}.

[58] N. A. Pertsev, A. G. Zembilgotov, and A. K. Tagantsev. Effect of mechanical boundary conditions on phase diagrams of epitaxial ferroelectric thin films. *Phys. Rev. Lett.*, 80:1988–1991, Mar 1998. doi: 10.1103/PhysRevLett.80.1988. URL `http://link.aps.org/doi/10.1103/PhysRevLett.80.1988`.

[59] U. Pietsch, V. Holy, and T. Baumbach. *High-Resolution X-Ray Scattering: From Thin Films to Lateral Nanostructures*. Advanced Texts in Physics. Springer, 2004. ISBN 9780387400921. URL `http://books.google.com/books?id=p8r9PpdpYrAC`.

[60] K.M. Rabe, C.H. Ahn, and J.M. Triscone. *Physics of Ferroelectrics: A Modern Perspective*. Topics in Applied Physics. Springer, 2010.

ISBN 9783642070969. URL http://books.google.com/books?id=u_iecQAACAAJ.

[61] Brian J Rodriguez, Clint Callahan, Sergei V Kalinin, and Roger Proksch. Dual-frequency resonance-tracking atomic force microscopy. *Nanotechnology*, 18(47):475504, 2007. URL http://stacks.iop.org/0957-4484/18/i=47/a=475504.

[62] A. Safari and E.K. Akdoğan. *Piezoelectric and Acoustic Materials for Transducer Applications*. Springer London, Limited, 2008. ISBN 9780387765402. URL http://books.google.com/books?id=OCddeKbhUa8C.

[63] Y Saito, H Takao, T Tani, T Nonoyama, K Takatori, T Homma, T Nagaya, and M Nakamura. Lead-free piezoceramics. *Nature*, 432(7013): 84–87, Nov 4 2004. ISSN 0028-0836. doi: {10.1038/nature03028}.

[64] S. Sasaki, C. T. Prewitt, J. D. Bass, and W. A. Schulze. Orthorhombic perovskite $CaTiO_3$ and $CdTiO_3$: structure and space group. *Acta Crystallographica Section C*, 43(9):1668–1674, Sep 1987. doi: 10.1107/S0108270187090620. URL http://dx.doi.org/10.1107/S0108270187090620.

[65] E. Sawaguchi and M. L. Charters. Aging and the double hysteresis loop of $Pb_\lambda Ca_{1-\lambda} TiO_3$ ceramics. *Journal of the American Ceramic Society*, 42(4):157–164, 1959. ISSN 1551-2916. doi: 10.1111/j.1151-2916.1959.tb12939.x. URL http://dx.doi.org/10.1111/j.1151-2916.1959.tb12939.x.

[66] A. Schilling, D. Byrne, G. Catalan, K. G. Webber, Y. A. Genenko, G. S. Wu, J. F. Scott, and J. M. Gregg. Domains in ferroelectric nanodots. *Nano Letters*, 9(9):3359–3364, 2009. doi: 10.1021/nl901661a. URL http://pubs.acs.org/doi/abs/10.1021/nl901661a. PMID: 19591494.

[67] J F Scott. Ferroelectrics go bananas. *Journal of Physics: Condensed Matter*, 20(2):021001, 2008. URL http://stacks.iop.org/0953-8984/20/i=2/a=021001.

[68] Sung Seok A. Seo and Ho Nyung Lee. Strain-coupled ferroelectric polarization in $BaTiO_3$-$CaTiO_3$ superlattices. *Applied Physics Letters*, 94(23), JUN 8 2009. ISSN 0003-6951. doi: {10.1063/1.3153512}.

[69] N. Setter, D. Damjanovic, L. Eng, G. Fox, S. Gevorgian, S. Hong, A. Kingon, H. Kohlstedt, N. Y. Park, G. B. Stephenson, I. Stolitchnov, A. K. Taganstev, D. V. Taylor, T. Yamada, and S. Streiffer. Ferroelectric thin films: Review of materials, properties, and applications. *Journal Of Applied Physics*, 100(5), Sep 1 2006. ISSN 0021-8979. doi: {10.1063/1.2336999}.

[70] T Shimuta, O Nakagawara, T Makino, S Arai, H Tabata, and T Kawai. Enhancement of remanent polarization in epitaxial BaTiO3/SrTiO3 superlattices with "asymmetric" structure. *Journal Of Applied Physics*, 91 (4):2290–2294, Feb 15 2002. ISSN 0021-8979. doi: {10.1063/1.1434547}.

[71] J. Sinsheimer, S. J. Callori, B. Bein, Y. Benkara, J. Daley, J. Coraor, D. Su, P. W. Stephens, and M. Dawber. Engineering polarization rotation in a ferroelectric superlattice. *Phys. Rev. Lett.*, 109:167601, Oct 2012. doi: 10.1103/PhysRevLett.109.167601. URL `http://link.aps.org/doi/10.1103/PhysRevLett.109.167601`.

[72] Massimiliano Stengel, David Vanderbilt, and Nicola A. Spaldin. Enhancement of ferroelectricity at metal-oxide interfaces. *Nature Materials*, 8(5): 392–397, May 2009. ISSN 1476-1122. doi: {10.1038/NMAT2429}.

[73] N. Stucki. *Artificial Ferroelectric Materials*. PhD thesis, University of Geneva, 2008.

[74] Agilent Technologies. *Agilent Impedance Measurement Handbook. 4th Edition.* 2009. URL `http://cp.literature.agilent.com/litweb/pdf/5950-3000.pdf`.

[75] C Thompson, CM Foster, JA Eastman, and GB Stephenson. Observation of the polarization of domains in ferroelectric thin films using x-ray interference. *Applied Physics Letters*, 71(24):3516–3518, Dec 15 1997. ISSN 0003-6951. doi: {10.1063/1.120377}.

[76] V. Torgashev, Yu. Yuzyuk, V. Shirokov, and V. Lemanov. Rotational polar structural distortions in solid solutions from raman spectroscopic data. *Physics of the Solid State*, 48:919–928, 2006. ISSN 1063-7834. URL `http://dx.doi.org/10.1134/S1063783406050179`. 10.1134/S1063783406050179.

[77] Almudena Torres-Pardo, Alexandre Gloter, Pavlo Zubko, Noémie Jecklin, Céline Lichtensteiger, Christian Colliex, Jean-Marc Triscone, and Odile Stéphan. Spectroscopic mapping of local structural distortions in

ferroelectric $PbTiO_3/SrTiO_3$ superlattices at the unit-cell scale. *Phys. Rev. B*, 84:220102, Dec 2011. doi: 10.1103/PhysRevB.84.220102. URL http://link.aps.org/doi/10.1103/PhysRevB.84.220102.

[78] J. Valasek. Piezo-electric and allied phenomena in rochelle salt. *Phys. Rev.*, 17:475–481, Apr 1921. doi: 10.1103/PhysRev.17.475. URL http://link.aps.org/doi/10.1103/PhysRev.17.475.

[79] David Vanderbilt and Morrel H. Cohen. Monoclinic and triclinic phases in higher-order devonshire theory. *Phys. Rev. B*, 63:094108, Jan 2001. doi: 10.1103/PhysRevB.63.094108. URL http://link.aps.org/doi/10.1103/PhysRevB.63.094108.

[80] BM Wul and IM Goldman. Dielectric constants of titanates of metals of the second group. *Compt. rend. Acad. sci. URSS*, 46:139–42, 1945.

[81] G. Xu, H. Hiraka, G. Shirane, J. Li, J. Wang, and D. Viehland. Low symmetry phase in (001) $BiFeO_3$ epitaxial constrained thin films . *Appl. Phys. Lett.*, 86:182905, Apr 2005. doi: 10.1063/1.1924891. URL http://dx.doi.org/10.1063/1.1924891.

[82] Guangyong Xu, G. Shirane, J. R. D. Copley, and P. M. Gehring. Neutron elastic diffuse scattering study of $Pb(Mg_{1/3}Nb_{2/3})O_3$. *Phys. Rev. B*, 69:064112, Feb 2004. doi: 10.1103/PhysRevB.69.064112. URL http://link.aps.org/doi/10.1103/PhysRevB.69.064112.

[83] Guangyong Xu, Z. Zhong, H. Hiraka, and G. Shirane. Three-dimensional mapping of diffuse scattering in $Pb(Zn_{1/3}Nb_{2/3})O_3$-$x$$PbTiO_3$. *Phys. Rev. B*, 70:174109, Nov 2004. doi: 10.1103/PhysRevB.70.174109. URL http://link.aps.org/doi/10.1103/PhysRevB.70.174109.

[84] Benedikt Ziegler. Growth and characterization of $PbTiO_3/BaTiO_3$ superlattices. Master's thesis, Stony Brook University, 2009. URL http://dspace.sunyconnect.suny.edu/handle/1951/52306.

[85] P. Zubko, N. Stucki, C. Lichtensteiger, and J.-M. Triscone. X-Ray diffraction studies of 180° ferroelectric domains in $PbTiO_3/SrTiO_3$ superlattices under an applied electric field. *Phys. Rev. Lett.*, 104:187601, May 2010. doi: 10.1103/PhysRevLett.104.187601. URL http://link.aps.org/doi/10.1103/PhysRevLett.104.187601.

[86] P. Zubko, N. Jecklin, A. Torres-Pardo, P. Aguado-Puente, A. Gloter, C. Lichtensteiger, J. Junquera, O. Stphan, and J.-M. Triscone. Electrostatic coupling and local structural distortions at interfaces in fer-

roelectric/paraelectric superlattices. *Nano Letters*, 12(6):2846–2851, 2012. doi: 10.1021/nl3003717. URL `http://pubs.acs.org/doi/abs/10.1021/nl3003717`.

[87] Pavlo Zubko, Stefano Gariglio, Marc Gabay, Philippe Ghosez, and Jean-Marc Triscone. Interface Physics in Complex Oxide Heterostructures. In Langer, JS, editor, *Annual Review Of Condensed Matter Physics, Vol 2*, volume 2 of *Annual Review of Condensed Matter Physics*, pages 141–165. Annual Reviews, 2011. ISBN 978-0-8243-5002-4. doi: {10.1146/annurev-conmatphys-062910-140445}.

Appendix A

X-ray Diffraction Supplement

A.1 Alignment Procedure

Before diffraction can be performed on a film, the sample must be aligned by adjusting many of the angles shown in Figure 4.1 that are available in our diffractometer. The alignment procedure described here is similar to other diffractometer configurations, but the angles may have different names. When a sample is placed onto the sample holder in a diffractometer, it will often not be flat at zero degrees in ω relative to the x-ray beam and will not be in the center of the x-ray beam. Since the x-ray source is fixed in position and direction, the Z motor is first adjusted so that the sample is centered in the x-ray beam, and the x-ray beam always hits the same spot on the sample even as the sample is rotated. This is accomplished by positioning the ω and 2θ angles at 0 degrees, and scanning in the Z direction. The measured x-ray intensity will drop as the sample moves into the beam, and will plateau when the sample is fully in the beam, and then fall off more rapidly as the sample holder blocks the beam. Then Z is aligned by selecting a value in the center of this first intensity drop such that the beam is centered on the top surface of the sample. Next, the ω and 2θ angles are moved to the nominal positions for diffraction from the $SrTiO_3$ substrate, obtained from the known lattice parameters of the $SrTiO_3$ substrate, and a rocking curve scan is performed by scanning over ω. Since the sample surface is not exactly flat, there will be an offset in ω, meaning the value of ω will not exactly be half of 2θ. The angle of the diffraction peak in the rocking curve is selected as the new value for ω. Another alignment scan is then performed with an 2θ-ω scan, where 2θ is changed at twice the rate as ω, maintaining the Bragg diffraction condition. Ideally, the 2θ angle should not vary from the theoretical position derived from the known lattice parameters of the substrate after compensating for the

offset in ω. However the center of the peak should still be selected in this scan since various other factors such as poor Z alignment, poor substrate quality, or internal 2θ offsets, can all contribute to a small offset in 2θ. However, once the 2θ angle is changed, the rocking curve over ω may change slightly, and so the rocking curve alignment is performed once more. For larger offsets in 2θ, this process can be iterated once more so that the substrate diffraction peak is properly aligned. Once alignment is complete, a wider 2θ-ω scan can be performed to measure diffraction peaks from films or superlattices.

For maps in reciprocal space, especially at non-zero values of ϕ, such as (113) maps, a modified alignment procedure is used to flatten the sample with respect to rotations in ϕ. The alignment involves the use of the ζ and ξ motors shown in Figure 4.1. The sample is moved to the nominal ω and 2θ positions for the (001) diffraction condition of the substrate. Then a scan is performed over ζ, similarly to a rocking curve, and the angle of the peak is selected. To align ξ, the sample is rotated 90 degrees and a ξ scan is performed, once again the equivalent of a rocking curve, and the angle of the diffraction peak selected. This alignment process is repeated once more since the ζ and ξ angles have some dependence on one another. Next, the ϕ angle is aligned, by scanning over scanning over ϕ and selecting the peak angle, which typically has some offset. Finally the other angles, ω and 2θ, are aligned as previously discussed for 2θ-ω scans.

A.2 Resolving c Lattice Parameters

The c lattice parameter of each material in a superlattice is not always measurable with accuracy due to convolution effects. To illustrate this effect, the relative intensities of the out-of-plane diffraction were calculated for a 30/20 PTO/CTO superlattice and corresponding thin films of each material, and for a 6/4 PTO/CTO superlattice and corresponding thin films of each material. For these calculations, assume the c lattice parameter of $PbTiO_3$ in the superlattice is 4.11 Å, the c lattice parameter of $CaTiO_3$ in the superlattice is 3.81 Å, and diffraction is performed with an x-ray wavelength of 1.5406 Å. Figure A.1 (Top) shows the calculated diffraction of a thin film of $PbTiO_3$ consisting of 30 unit cell layers with another thin film of $CaTiO_3$ consisting of 20 unit cell layers grown coherently on top. If this pattern is repeated five times, creating a superlattice, these peaks in the top graph do not disappear, but are instead convoluted with the superlattice peaks, as can be seen in the graph in Figure A.1 (Bottom). If one performs a measurement similar the bottom figure and then wants to determine c lattice parameters of each material from this graph, it would be difficult to do so, but possible with similar kinds of

calculations. Now consider a 6/4 PTO/CTO superlattice and corresponding thin films, which have the same ratios of materials as the 30/20 superlattice, but a much smaller superlattice wavelength, with calculated intensities shown in Figure A.2. The thin films analogues of each of these (Top) have the same central diffraction peaks at the 2θ angles as the 30/20 superlattice, but the peaks are much broader and convolute into less well defined peaks. As these thin films are repeated into a superlattice, shown in the bottom graph of Figure A.2, the convolution obscures the peaks further, and so resolving the peaks of the $PbTiO_3$ layers and $CaTiO_3$ layers would require very high resolution and intensity from synchrotron radiation, if at all possible.

At lower angles such as (001) or (002), the diffraction from each block of material convolutes into a single peak, making the determination of the c lattice parameter of each material extremely difficult, unless the superlattice wavelength is very large. Consider again the 6/4 PTO/CTO superlattice again in Figure A.2, but now around the (001) diffraction of the substrate. Using the same c lattice parameters as before for $PbTiO_3$ and $CaTiO_3$ and Bragg's Law 4.1, the nominal 2θ angles of each material block is calculated as $2\theta_{PTO} = 21.6°$ and $2\theta_{CTO} = 23.3°$. Because of the convolution, it is not possible to resolve these peaks individually, as shown in Figure A.3.

These calculations and graphs also show the behavior of the superlattice peak 2θ position corresponding to the average c of the unit cells composing the superlattice. The superlattice peak corresponding to the average c must lie between the two broad diffraction peaks of the blocks of materials composing the superlattice. At low angles and small superlattice wavelengths, there only exists one superlattice diffraction peak in this small 2θ angular separation of the two materials. Furthermore, because of the convolution, this causes the particular superlattice peak corresponding to the average c over the superlattice to have the highest intensity. At high angles or large superlattice wavelengths, the 2θ angular separation between the broad diffraction peaks is much larger, and there now exist several superlattice peaks between these diffraction peak from each material block, and so one cannot easily choose which superlattice peak corresponds to the average c of the unit cells.

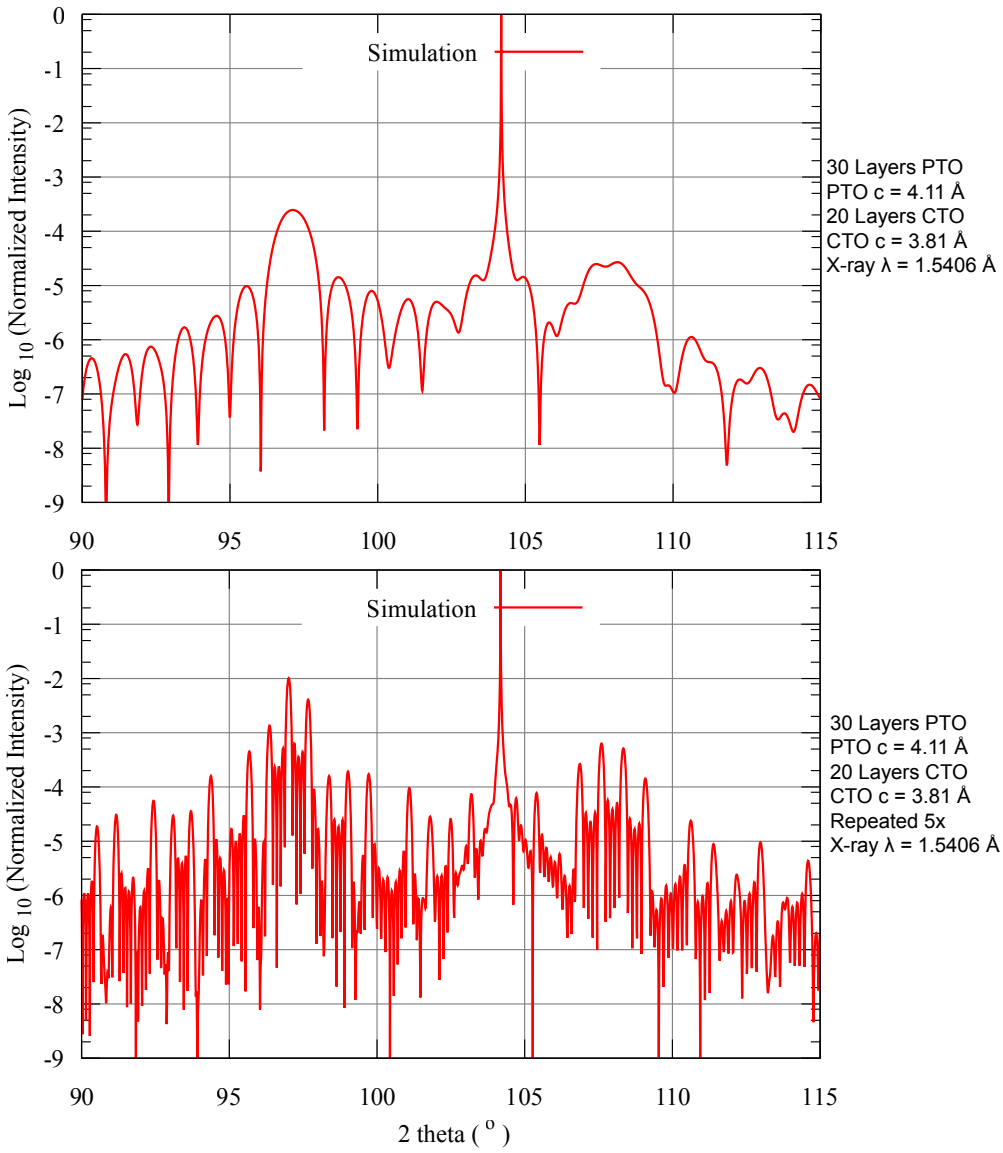

Figure A.1: Calculated diffraction from 30 unit cell layers of $PbTiO_3$ and 20 unit cell layers of $CaTiO_3$ (Top) and a 30/20 PTO/CTO Superlattice with 5 repetitions (Bottom), around the (004) diffraction peak of the substrate.

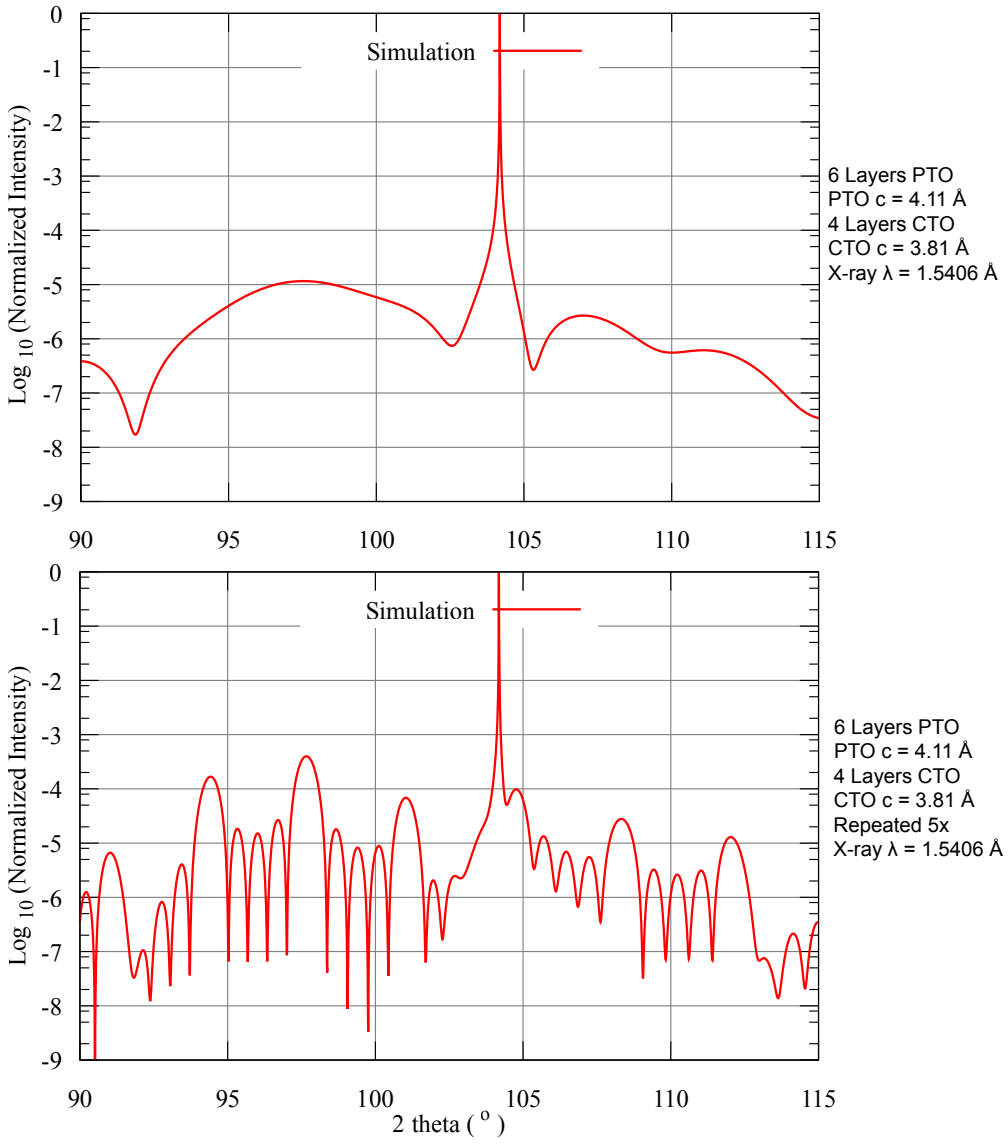

Figure A.2: Calculated diffraction from 6 unit cell layers of $PbTiO_3$ and 4 unit cell layers of $CaTiO_3$ (Top) and a 6/4 PTO/CTO Superlattice with 5 repetitions (Bottom), around the (004) diffraction peak of the substrate..

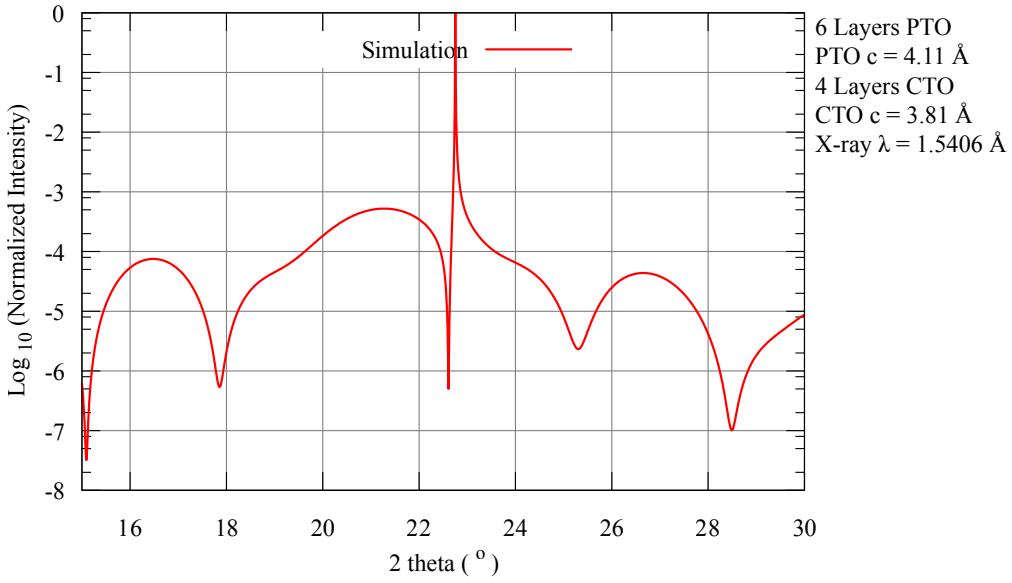

Figure A.3: Calculated diffraction from 6 unit cell layers of $PbTiO_3$ and 4 unit cell layers of $CaTiO_3$ near the (001) $SrTiO_3$ diffraction peak. It is not possible to resolve the two main diffraction peaks due to the convolution at low angles.

A.3 Interpretation of Non-integer Periods

Following [73], another method to try to address the interpretation of the diffraction is to define a new superlattice wavelength, Λ', with $\Lambda' = N'\Lambda$ and N' being smallest positive integer such that each block of material has an integer number of unit cells in Λ'. Or expressed mathematically, consider an N/M superlattice composed of materials A and B so that $\Lambda = (Nc_A + Mc_B)$, as before, but now here suppose N and M are rational numbers, or $(N, M \in \mathbb{Q})$. Then choose the smallest N' that is a positive integer, or $N' \in \mathbb{N}$, such that $(N'N) \in \mathbb{N}$ and $(N'M) \in \mathbb{N}$. Thus the repeated structure with wavelength Λ' will necessarily be an integer number of unit cells and have an integer number of unit cell layers of each material A and B and have orders n that are positive integers. The problem with this construction is that not all possible orders in this case will lead to a diffraction peak. If the superlattice wavelength is increased by a factor N', one would expect N' times more superlattice peaks compared to a similar diffraction of a superlattice with perfect integer layers, and this is clearly not observed. So if this interpretation is used, restrictions must be placed on values of n that give rise to diffraction peaks from Bragg's law, and adjacent peaks would differ in order by $N'n$. Even in this interpretation, we still have the same result that equations for $\bar{c}$ (4.6),

c/a (4.7), and Λ (4.4) are unchanged by this modification since these equation do not contain n. Additionally, in the derivation of $\overline{c}$, the order n and number of unit cell layers $(N + M)$ term still equals 1 and drops out of the equation, since the numerator and denominator are now both multiplied by N'.